Synthetic seismic illumination of CO₂ migration in fault zones

Johannes Krakowski

Thesis submitted for the degree of

masters in Structural Geology and Tectonics

60 Credits

Department of Geosciences

Faculty of Mathematics and Natural Sciences

UNIVERSITY OF OSLO

June 2021

Synthetic seismic illumination of CO₂ migration in fault zones

Photo: Ingid Anell, 2019

Master Thesis in Structural Geology and Tectonics

Part of the COTEC research project at the University of Oslo
Written by Johannes Krakowski

Supervisors: Ingrid Anell, Alvar Braathen,Thea Sveva Faleide

Abstract

Many subsurface geological storage sites for anthropogenic CO_2 are situated in normal fault zones, where there is a risk of leakage as faults can act as fluid conduits. Optimal CO_2 storage sites are generally located at depth which are most easily studied using seismic data, therefore monitoring and verification of the storage site is limited by seismic resolution. Seismic modelling of onshore analogues can be used to aid in understanding the seismic expression of geological features and the effect of CO_2 migration. Synthetic seismic modelling of CO_2 leakage in fault zones is performed in this study by studying the CO_2 emitting siliciclastic Little Grand Wash fault (Utah, USA).

The geomodel used to generate synthetic images is based on literature studies and comprises data both from the study area and comparable geological systems. The model is designed to represent leakage of a CO_2 plume through a seal-bypass system in a fault zone. Scenarios of the system prior to CO_2 exposure and prolonged mineralization of rocks is modelled, as well as reservoir conditions with added overburden to simulate a realistic storage scenario. Synthetic seismic images of each scenario were generated using a seismic modelling software based on input of the geomodel and associated elastic properties.

The study of the generated synthetic seismic images confidently interprets several aspects of a CO_2 plume migrating trough siliciclastic fault zones, implying that many features may be visible in conventional seismic data, and that fluid conduits in the fault zone may be resolvable using seismic p-cable technologies. If the goal is illuminating fluid-conduits prior to storage, there is room for an improved 3D model of the fault zone with more nuanced fault facies and variations in stratigraphic architecture. The findings of this study will ultimately aid in improving the interpretation of fluid migration in faults and expression and detectability of fault facies within a fault-zone.

Acknowledgements

Table of contents

Chapter 1: Introduction

This study addresses two fundamental questions:

    i)   Is it possible to illuminate CO_2 migration along fault zones in seismic images?

    ii)   Which elements in fault architecture cause fluid leakage? Do these elements produce noticeable seismic signatures?

1.1 Background and rationale

COTEC is a multidisciplinary research project dedicated to Carbon dioxide (CO_2) containment and monitoring techniques.

Carbon capture and storage (CCS) is a process consisting of the separating CO_2 from industrial and energy-related sources, and transporting it to a storage location and long-term isolation from the atmosphere. CCS is acknowledged as a viable technique for mitigating global emissions, and subsurface geological reservoirs are currently the best and most reliable storage candidate. (Benson, et al., 2005). A critical part of the storage process is avoidance of CO_2 leakage into the atmosphere. The COTEC project is investigating the aspects of fluid escape mechanisms from subsurface CO_2 storage reservoirs, and any geological features that are detrimental to subsurface storage of CO_2, with the aim of monitoring and de-risking storage sites. The long term safety and effects of CO_2 storage are still unclear. Investigating natural onshore reservoirs of CO_2 can therefore provide valuable knowledge that can be applied in subsurface scenarios.

The COTEC project mainly focuses on one such study area in East-central Utah a few kilometres south of Green River (chapter 1.3): The Little Grand Wash fault (LGWF). Here natural seeps of CO_2 from deep Paleozoic strata (2.6 km) is transmitted to the surface (Wilkinson, et al., 2009). It is the outlet of a leakage system transmitting up to 30 tons of CO_2 charged brine per day through springs within the fault zone (Baer & Rigby, 1978; Gouveia, et al., 2005). The system has a 400 k year leakage history, as described by Burnside, et al. (2013). The area is easily accessible for field study and thus is an excellent analogue to a subsurface fluid escape scenario that may be encountered in future storage sites. The system has a seemingly intact reservoir-seal complex that may look promising in conventional seismic data, yet is still leaking CO_2. Millennia's of leakage has left a distinct geological footprint in the strata and fault damage zone, allowing us to see its flow paths, and predict how CO_2 storage sites might behave long term.

Geological storage of anthropogenic CO_2 will in most cases involve injection at depths more than 800 meters, a domain that primarily can be studied trough seismic data (Benson, et al., 2005). Seismic images have several limitations in resolution (Bond, 2015; Rotevatn & Fossen, 2011). Many features

that are involved in fluid leakage, like secondary fault structures and thin strata (<15 meters thick) are below seismic resolution (Andersen, 2020). Exposure to CO_2 over time is expected to further weaken the signal of these structures (Aben, et al., 2017). Although the seismic response and detectability of CO_2 is well studied (Agofack, et al., 2018; Chadwick, et al., 2009; Furre, et al., 2017) Small leakages rates such as that of the LGWF is hypothesized to be challenging to detect in conventional seismic (Burnside, et al., 2013).

To better understand fluid leakage in seismic data, seismic modelling could be applied to bridge the gap in resolution between outcrop and seismic data (Lecomte, et al., 2015). Seismic modelling has the potential to provide valuable information on the sensitivity and limitations of real seismic data in the subsurface (Lecomte, et al., 2015). Several studies have utilized seismic modelling from outcrop-derived geological models to develop Seismic modelling techniques that solved various seismic interpretation problems (Andersen, 2020; Anell, et al., 2016)

1.2 Objectives

The rocks that make up The Little Grand Wash Fault stacked reservoirs and seals show a distinct fluid bypass-system, which is one of the most studied CO_2 leakage sites in the world. The stratigraphy is studied at a large variety of sites. This makes it possible to estimate how it responds to faulting and CO_2 exposure. Such a location presents an opportunity to study processes that may occur during subsurface CO_2 leakage within a future storage site.

The work presented in this thesis applies geophysical data and field outcrop data from the study area to create detailed geological models of the system. These models are based on scenarios of the system with and without CO_2, overburden and damage zone. A ray-based modelling approach is applied to create synthetic seismic images of these models. This study aims to better understand how CO_2 migration in fault zones is visualized in seismic images by addressing the following questions:

- What are the ideal survey parameters for illuminating the stratigraphy, fault zone and CO_2 plume?
- How is CO_2 leakage and fluid conduits in siliciclastic normal fault zones expressed in seismic images?
- Can seismic modelling of CO_2 leakage aid monitoring and verification of geologically stored CO_2, and evaluate fault-sealing capabilities in storage sites?

1.3 Study area

The study area is located in the state of Utah, mid-western USA. The Little Grand Wash Fault is located a few kilometres south of Green River in southeast Utah (Fig. 1). Green river is characterized by an arid landscape of flat lying, faulted sedimentary strata that are part of the Colorado Plateau, a large physiographic region hosting famous sites such as the Grand Canyon. The state of Utah offers a relatively dry climate, with scattered forest areas, the result of it being located in the rain shadow of Sierra Nevada, California and Wasatch mountains.
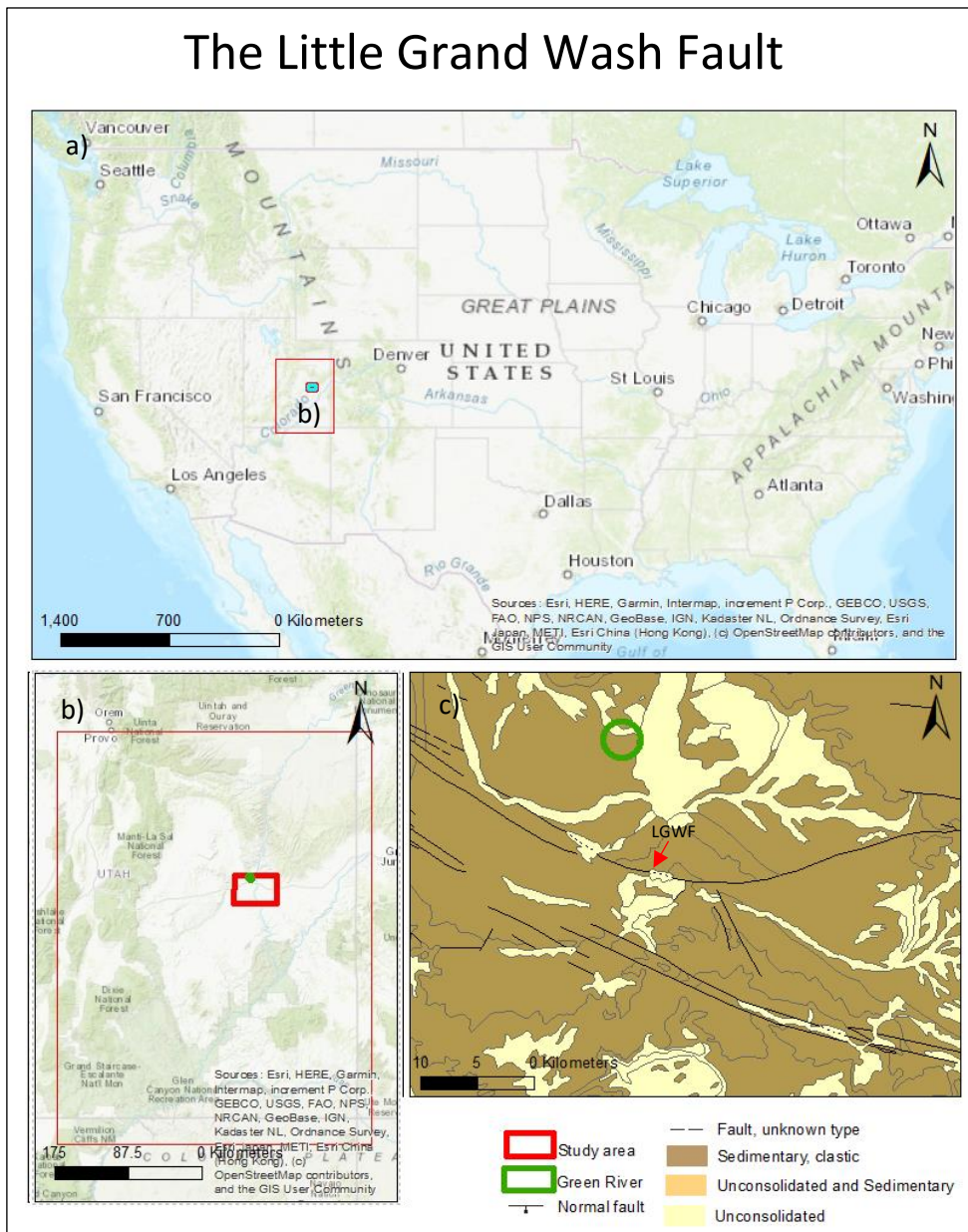
Figure 1: Location of the Study area, Green River, and the Little Grand Wash Fault. a) Overview of the U.S.A and location of b) The study area location within the state of Utah c) LGWF, Paradox Basin and Green River. From ArcMap (v.10.8.1): world topographic map and State Geological Map Compilation (SGMC)

Chapter 2: Geological setting

2.1 Tectonic setting

The Colorado Plateau is a large physiographic region in the western interior, U.S.A. The plateau has a very long and complex geological history. To better understand the context of the depositional history and fault development of the study area outlined in chapter 2.1.2 and 2.3, a brief overview of the regional geological setting since Late Triassic times, is outlined in the following chapter.

2.1.1 Regional tectonic setting:

The Colorado Plateau is positioned relatively close to the North American plate boundary (Fig. 2a) and is defined as a back-arc setting during the Mesozoic and Tertiary times (Peterson & Turner-Peterson, 1989). The numerous orogenic events in western USA produced foreland basins and eventually lifted the plateau up, while episodes of extensions produced rifted back-arc basins where many the sedimentary units we see today were deposited. The most important tectonic events were firstly the Late Jurassic-Early Cretacious Laramide and Sevier orogeny. These events led to the formation of depositional basins like the Elko foreland basin and the Utah-Idaho trough that created deposition in the study area (Bjerrum & Dorsey, 1995; Maidment & Muxworthy, 2019; DeCelles, et al., 1995; Kirkland, et al., 2016). A latter event of high importance is the development of the western interior seaway, the large inland sea that existed during the mid- to late Cretaceous, splitting the North American continent into two landmasses (Blakey, 2014; Peterson & Turner-Peterson, 1989) (Fig. 2b). The depositional environments that existed in South-Eastern Utah throughout these events are further outlined in chapter 2.3. The latest significant tectonic event that affected the entire Plateau uplifted it several thousand meters during the Pliocene. This is apparent from the present elevation of Cretaceous marine strata deposited in the western interior that are now at elevations of as much as 3,6 km above sea level (Blakey, 2014).
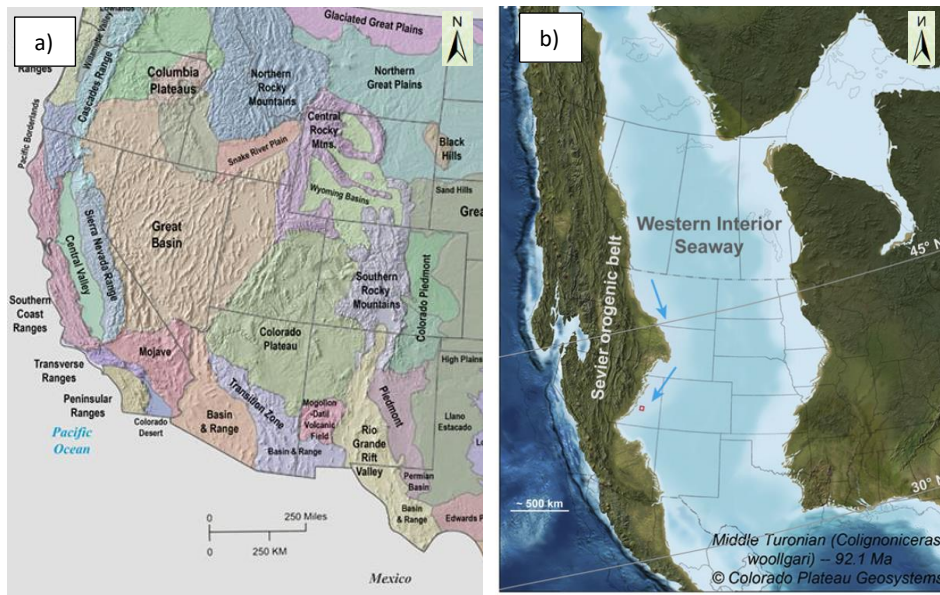
Figure 2: a) Topographic map illustrating the different physiographic regions of the western U.S.A, including the vast extent of the Colorado Plateau in the western interior. Cropped from published map by Fenneman (1917). b) paleo-geographic map showing extent of the Western Interior Seaway during mid-late Cretaceous, from Blakey (2014)

2.1.2 Local structural setting: The Little Grand Wash Fault.

The study area is located within the Colorado Plateau which is characterized by normally faulted basins that are broadly folded. The strata is generally flat lying, and well preserved outside these deformation zones. One of these basins is the Paradox Basin, a SE-NW trending foreland basin of carboniferous origin. It contains a series of normal faults trending NE-SW and E-W, implying that the rocks in the area have been subjected to numerous tectonic loads (Newell & Butcher, 2015) (Fig. 3a). The origin of this deformation is likely the paradox basins role as an evaporitic basin that caused salt movement in the subsurface during Tertiary times (Nuccio & Condon, 1996). Episodes of compression and uplift in the Cretaceous to early Tertiary, likely reactivated the fault systems on several occasions. This is possible in Foreland basin scenarios (Huffman, et al., 1996; Middleton, 1989). Today the area is under NNE extension (Williams, 2005).

On the Paradox Basin´s northern margin, near Green River in eastern Utah, we find a large E-W trending curved normal fault, The Little Grand Wash Fault (LGWF). (Fig. 3b). It is a grologically significant site as it is transmitting CO_2 from deep (2.6 km) Palaeozoic strata to the surface. A regional anticline produced by salt tectonics, is an important structural part of the study area. It is referred to as the Green River Anticline. The anticline tilts strata towards the Green River area, allowing gas to accumulate here beneath an effective regional seal, only leaking from the LGWF (Campbell & Baer, 1978). The gas likely originates from thermal decomposition of calcite or hydrocarbons (Baer & Rigby, 1978; Gouveia, et al., 2005; Wilkinson, et al., 2009). The area contains travertine deposits from the leaking CO_2. Travertine is a sedimentary rock, formed by the precipitation of carbonate minerals from

solution in ground and surface waters, due to the acidification of water from CO_2 saturation (Gratier, et al., 2012).

The fault zone is 200 m wide at its widest and contains 4–5 major subparallel fault segments that form multiple soft- and hard-linked relay ramps. The offset varies from 200 to 300 meters (Fig. 3b). Studies suggest that all evidence of leakage is located along the northernmost traces of the Little Grand Wash fault at or near the fold axis of the Caine Creek Anticline (Fig. 3b) (Dockrill & Shipton, 2010)
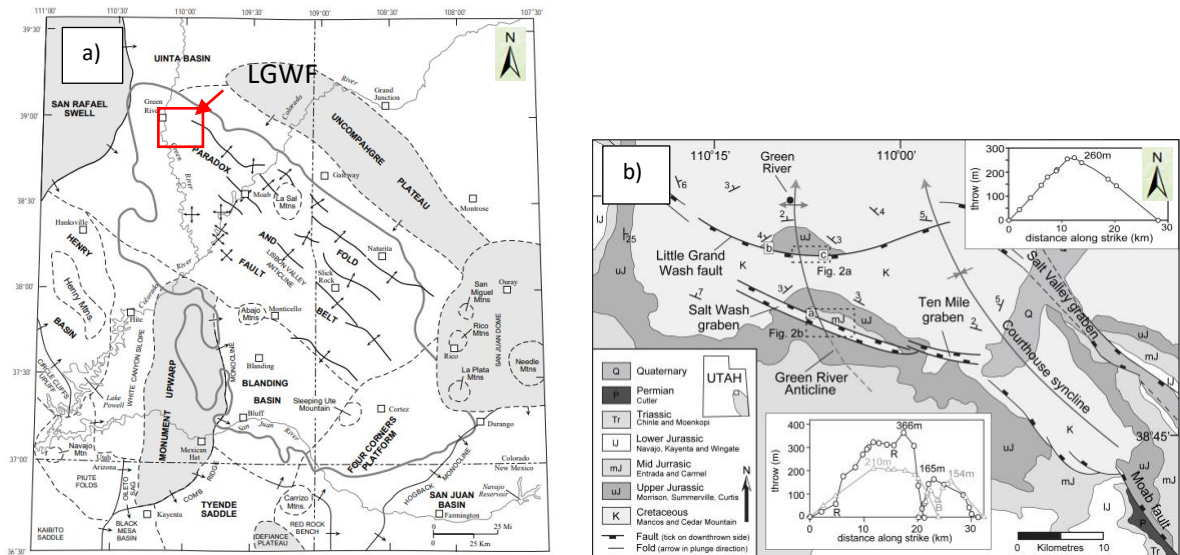
Figure 3 a) Regional structural setting of the Paradox Basin, illustrating NNE-SSE and E-W trending fault development, and the location of figure 3 a. Modified from figure 2 in Nuccio & Condon (1996) b) Main structural elements illustrated on a topographic map of the green river area. Modified from figure 1 in Dockrill & Shipton (2010).

2.2 Stratigraphic overview:

A brief overview of the sedimentary units in the upper LGWF is presented in table 1.

Table 1: Stratigraphic overview: The data is compiled from field work of several authors (Dockrill & Shipton, 2010; Doelling, 2002; Greentown, 36-24H, 2009; Heath, 2004; Kampman, et al., 2013; Skurtveit, et al., 2020; Stockton & Balch, 1978; Urquhart, 2011; Williams, 2005; Zuchuat, et al., 2019a) and is further outlined in Chapter 4.2.

Group	Formation (abbreviation)	Members (abbreviation)	Lithology	Age
	Mancos Formation	Tununk (K_{mt})	Shale	Early Cretaceous
Dakota group	Cedar mountain Formation (K_{cm})	Ruby Ranch Member	Shale	Early Cretaceous
		Buckhorn conglomerate	Conglomerate	
	Morisson Formation	Brushy Basin member (J_{mb})	Shale-silt	Late Jurassic
		Salt wash member (J_{ms})	Interbedded silt-sand	Late Jurassic
San Rafael group	Summerville Formation (J_s)		Silt	Jurassic
	Curtis Formation (J_c)		very fine Sand	Jurassic
	Entrada Formation (J_e)	Slick rock member	Sand	Jurassic
		Earthy Facies	Silt – very fin sand	
	Carmel Formation (J_c)		Interbedded Silt-shale, evaporites	Jurassic
Glen Canyon group	Navajo Formation (J_n)		Sand	Early Jurassic
	Kayenta Formation (J_k)		Sand	Early Jurassic
	Wingate Formation (J_w)		Sand	Early Jurassic

2.3 Basin development and depositional history:

2.3.1 Late Triassic/Early Jurassic: Glen Canyon Group

The Glen Canyon group act as the main reservoir in the studied system. The units consist of aeolian and low-energy fluvial depositional setting that deposit high porosity, well-sorted sandstones, bound by interdune or flood deposits of silty or muddy lithology. The units are massive, and in many places show thicknesses of several 100´s of meters (table 1). They were deposited in a back-arc, arid environment. These conditions often produce excellent reservoir rocks. The three units form a stacked aquifer system of permeable and porous aeolian and fluvial sandstone (Williams, 2005). Tectonic deformation from salt tectonics folded these units and allowed fluids to accumulate under traps such as the Green River anticline and the footwall of the LGWF (Jamison & Stearns, 1982).

2.3.1.1 Wingate (Jw):

The Wingate Formation forms massive thicknesses in south-eastern Utah (table 1). The aeolian sandstone facies imply the existence of a large Jurassic erg (Clemmensen, et al., 1989). This produces a sedimentary architecture of large-scale stratification of fine sandbodies and smaller, wet interdune deposits (Kocurek & Dott, 1981; Tunheim, 2015)

2.3.1.2 Kayenta (Jk):

During this time, the aeolian system shifted north. On the southern part of the aeolian system the Kayenta Formation was deposited. It is recognised by a thinner, darker layer between The Wingate and Navajo formations, characterised by its red colour (Averitt, et al., 1955; Greentown, 36-24H, 2009). Analyses of cross-bedding in these layers reveal a fluvial depositional system of low to moderate energy streams flowing eastward (Averitt, et al., 1955). Channels and floodplain deposits are typical, as they deposited wide and thin sandsheets (Røe & Hermansen, 2006). Desert conditions also briefly occurred in this area, evident by fossil mudcracks.

2.3.1.2 Navajo Sandstone (Jn):

The Navajo Formation is related to a renewed aeolian system that existed in the back arc setting in the early Jurassic (Blakey, et al., 1996). It is characterized by large scale cross-bedding, and it is large acknowledged that it were deposited during the presence of a large Erg that covered large parts of the western interior. It shows interdune deposits of finer grained sandstone (Hunter, 1981)

2.3.2 Middle Jurassic: The San Rafael group:

The San Rafael group that outcrop in central Utah are a vital part of the study area as it makes up the seal-bypass system that is present in the fault, while the Entrada dune facies store some of the CO_2 charged brine from the main reservoir. On a regional scale the group displays a thickening westward, and ranges from almost non-existent in the east to more than 2km deep in west-central Utah (Brenner

8

& Peterson, 1994) These units are believed to have been deposited in an intracratonic basin subducted along a NNE-SSW axis, known as the Utah Idaho trough (Thorman & Peterson, 2004).

Most interpretations of the San Rafael group interpret the Utah-Idaho trough as a foreland basin related to the Elko Orogeny in Nevada during the middle Jurassic (Bjerrum, et al., 1993; Burchfiel & Crabaugh & Kocurek, 1993; Davis, 1972; Thorman & Peterson, 2004). A quantitative basin analysis of the middle Jurassic strata of the Colorado plateau was done by Bjerrum & Dorsey (1995). They describe a foreland basin that experienced numerous uplifts and subsidence episodes as a result of several tectonic pulses of the Elko Orogeny.

2.3.2.1 Carmel Formation (Jcp):

The initial subsidence of the Utah-Idaho trough, flooded the aeolian system related to the Navajo sandstone in early Jurassic (Blakey, et al., 1996). This marine transgression is also described by Bjerrum & Dorsey (1995). The transgression led to the Carmel Sea, as the depositional environment of The Carmel Formation is interpreted as marine to coastal plain, and is generally thickening to the west (Blakey, et al., 1996). Its distal part consists of red mudstone and sandstone, and its proximal part, outcropping in east-central Utah, varies between limestone and mudstone. Further east it transitions into sandstone, and is defined as a separate formation called the "Page Sandstone". The system tracts, although slightly shifting all the time, are interpreted as a transgressive and high-stand system tract (Blakey, et al., 1996). An erosional surface named J-S-up separates the middle from the top Carmel Formation, and mark the onset of a marine regression. The retreating sea was replaced by arid continental conditions (Crabaugh & Kocurek, 1993).

2.3.2.2 Entrada Formation:

In most of the literature, the Entrada Formation is described as an aeolian system, being part of a large erg that covered much of the western interior (Crabaugh & Kocurek, 1993; Bjerrum & Dorsey, 1995; Blakey, et al., 1996). The Entrada sandstone is generally characterized by more aeolian facies to the east and more sabkha/shallow marine deposits to the west, with some variations depending on base level changes. In the Green River area the sequence is dominantly a sandstone from wet aeolian conditions, known as the Slickrock Member (Williams, 2005). There are also highstand episodes with sabkha and shallow marine deposition. Where these facies occur, they are unofficially defined as "earthy facies". The sequence of the upper part (earthy facies) show progradation (Crabaugh & Kocurek, 1998), implying that the shoreline transgressed eastward as the subsidence In the Utah-Idaho through increased (Zuchuat, et al., 2019a)

2.3.2.3 *Curtis Formation:*

At the boundary between the Entrada and Curtis formations, an erosional unconformity, J-3, mark the transition from an aeolian setting to the Curtis Sea. Fluvial erosion of the uplifted flexural bulge account for most of the unconformity (Bjerrum & Dorsey, 1995; Zuchat, et al., 2019a) Sedimentary samples and sequence stratigraphic studies have identified the lower Curtis Formation as a transgressive system tract, topped by a maximum flooding surface (Bjerrum & Dorsey, 1995). The middle and upper Curtis formation appear near Crystal Geyser (Zuchuat, et al., 2019a). The Curtis formation show upward coarsening and is interpreted as a high stand system tract, as it display deposits of both marine to tidal channels in a shore-face environment. At the time of the upper Curtis, the basin was mostly tide dominated in the study area, leading to deposition of a very fine grained sandstone (Zuchuat, et al., 2019b).

2.3.2.4 *Summerville Formation:*

The same highstand system tract also deposited the Summerville Formation as the equivalent coastal plain facies (Zuchuat, et al., 2019b; Zuchuat, et al., 2018). The Curtis-Summerville transgression can be attributed to a flexural basin subsidence after renewed thrusting in the Elko orogeny (Bjerrum & Dorsey, 1995). Following this high stand, a forced regression took place as we see the J-5 unconformity erodes, sometimes all the way down to the J-3 unconformity. After the J-5 unconformity, deposition of the upper Jurassic Morrison formation took place. This marine regression marks the end of deposition the San-Rafael Group in this area.

2.3.3 Late Jurassic: Morrison Formation

The Morrison Formation was deposited in a backbulge depocenter of a foreland basin system. This system was related to the Sevier Orogeny that stretched from Northern Canada to Northern Mexico. As a result, this depocenter stretched quite far, evident by the extent of the Morrison Formation in outcrops all over the western interior. The formation formed in a terrestrial setting, evident by fluvial, overbank and lacustrine deposits. Characterised by abundant presence of fossil dinosaur fauna, the Formation is studied quite extensively by palaeontologist and geoscientists. (Maidment & Muxworthy, 2019).

On the Colorado Plateau, the Morrison is Formation is separated into two lithostratigraphic members: The Brushy Basin Member (Jmb) and the Salt wash Member (Jms). Here the base of the formation is generally considered to be the J-5 unconformity. The salt wash member is defined by its high content of coarse-grained fluvial channel belt deposits, while finer grained overbank flood deposits define the Brushy basin member. The source drainage area being the Sevier forebulge, the eastward and lateral extent of the extent of the Salt-wash member are dictated by the base-level changes. These changes

are driven by the climatic and tectonic forces related to the sevier orogeny. The Low-stand sequences of show narrower multi-storey channels within the salt wash. During transgressional phases show higher preservation of the Brushy basin member. The Highstand show higher lateral extent of the Salt wash (Roca & Nadon, 2007). The upper part of the formation is characterized by a fall in base-level hypothesized to be caused by an north-eastward migration of the Sevier forebulge (DeCelles, et al., 1995). This resulted in a widespread unconformity between the Late Jurassic Morrison Formation and the Early Cretaceous Cedar Mountain Formation (Willis, 1999).

2.3.4 Early Cretaceous: The onset of the western interior seaway

The increased flexural loading of the Sevier Orogeny, would eventually replace the forebulge setting, with a foreland basin, leading to a new transgression that would eventually open the western interior seaway. (Blakey & Ranney, 2018).

2.3.4.1 Dakota Group:

The Dakota group was deposited in a foreland basin setting of the Sevier fold-and-thrust belt. It is characterized by fluvial to upper shoreface deposits. It outcrops over the entire western interior. In East-central Utah, its sub-units, The Dakota and Cedar Mountain Formation is found overlying the Morrison formation. These units are genereally thinner in East-Central Utah (<50 meters thick)

The Cedar Mountain Formation (K_{cm}) is interpreted as a fluvial setting in eastern Utah, with as much as 10 members identified in various locations (Kirkland, et al., 2016). The Buckhorn Conglomerate Member, formed within incised-valleys eroded into the underlying Brushy Basin Member of the Morrison Formation (Currie, 1998; Garrison, et al., 2007), The Ruby Ranch Member, a purple to dark gray, muddy sandstone, siltstone, and mudstone deposit and the Poison Strip Sandstone are all found in the green river area (Currie, 1998; Kirkland, et al., 2016). These fluvial patters are interpreted as flowing northeast towards an inland-sea (Garrison, et al., 2007).

2.3.4.2 Mancos Shale Formation: Tununk Shale Member (Kmt)

The Tununk Shale member of the Mancos Shale outcrops in the southern portion of the study area, in the Little Grand Wash hanging wall. It is a massive gray marine shale unit. Although it is eroded quite thin in the study area, the unit can reach 400m thickness in other parts of the Colorado Plateau. It was deposited in an asymmetric foreland basin, that at the time formed much of the depression that allowed transgression of the western interior seaway (Currie, 1998; Livaccari, 1991). The marine transgression that took place is also the product of a global greenhouse effect during the cretaceous. During this global high stand, the Tununk shale was deposited during the western margin of this basin. It is characterized by a series of secondary regressive-transgressive sequences (Li & Schieber, 2017).

2.3.5 Uplift and erosion

2.7-4.5 km of strata covered the western Colorado plateau during the Late Cretaceous, evident by Apatite fission track methods (Dumitru, et al., 1994). Erosion and orogenic collapse of the Laramide Orogeny uplifted and eroded these strata from the plateau over a period of 75 mill. years. (Fan & Carrapa, 2014). As a result, the stratigraphy in study area was buried to depths of 3km (Nuccio & Condon, 1996) (Fig. 3).
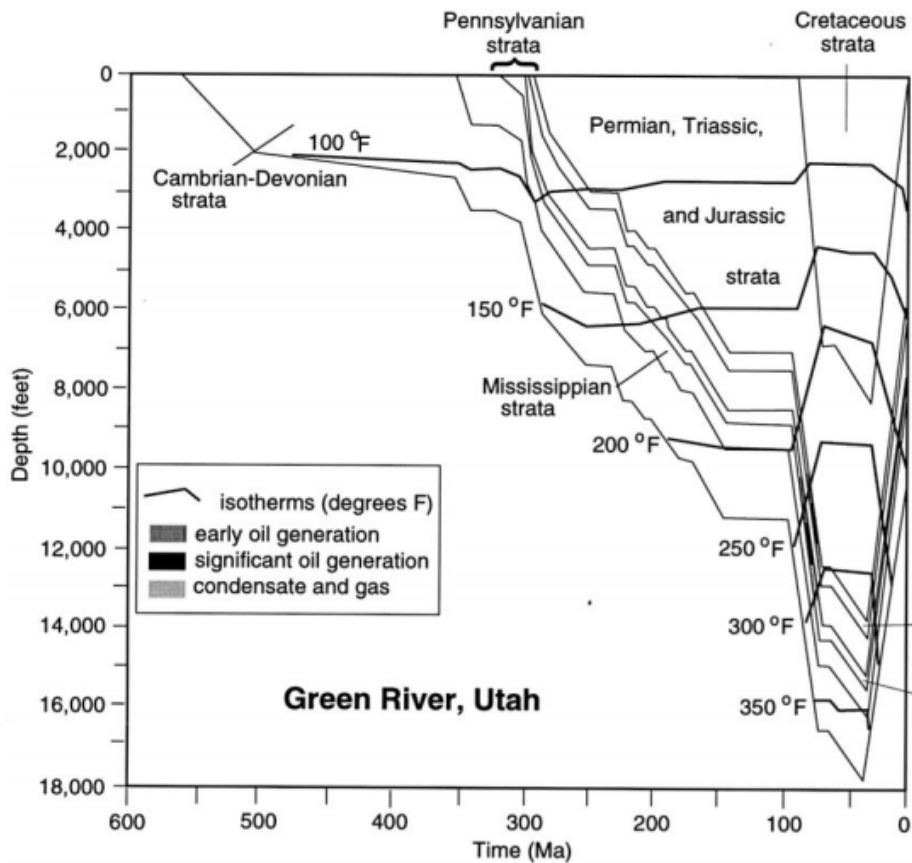
Figure 3: Burial, thermal and petroleum generation analysis from the Green River area. Jurassic strata have been buried at depths of 9000 feet (3km). Taken from figure 10 in Nuccio & Condon (1996)

Chapter 3: Theoretical background

3.1 seismic interpretation:

3.1.1 Seismic data:

A seismic image displays subsurface architecture in the form of surfaces of reflected energy (reflectors). These surfaces are processed by geophysicists and software from traces of reflected waves. Each geological unit has a set of physical properties that determines its acoustic impedance (the way acoustic pressure propagates trough that medium). Contrasts between different units mark a change in Acoustic Impedance (AI). At the interface some wave energy is reflected, and some are transmitted. The difference in reflected/transmitted energy determines if the reflected wave has a positive or negative amplitude (peak or trough). This is expressed by a reflection coefficient. A large contrast yields a high wave amplitude. In 1D this forms a seismic trace. 2D and 3D seismic images are essentially composed of these seismic traces (Kearey & Brooks, 1991). The AI indicates the mediums seismic wave velocity, most importantly for the Primary (compressional) and Secondary (shear) body waves (Sheriff & Geldart, 1995).

3.1.2 Seismic resolution:

The smallest level of details a geophysical image can capture is the seismic resolution. The resolution is dependent on the dominant wavelength, λ, of the seismic signal. The wavelength is related to the seismic velocity *v* and the dominant frequency *f*. They are related by the expression in equation 1.

Equation 1:

$$\lambda = \frac{v}{f}$$

The velocity is dependent on the density and elastic properties of the medium the wave intrudes. The frequency is dictated by the wave energy. As waves lose energy with travel time, deeper parts of a seismic signal will have a lower frequency (Kearey & Brooks, 1991). In addition, deeper parts of the crust are generally denser due to mechanical and chemical compaction (Bjørlykke, 2015) and have a higher seismic velocity, making it harder to distinguish the reflected waves. As a result the seismic resolution decrease (Herron, 2011). Seismic resolution in the vertical direction is limited by seismic tuning thickness that is equal to a quarter of a wavelength. This is known as the limit of seperability

13

(Rafaelsen, 2006; Simm & Bacon, 2014). Geological features may be detectable in a seismic image even though they cannot be resolved and constrained to a single reflector. This is known as the limit of detectability and range from $\lambda/20$ to $\lambda/30$ (Simm & Bacon, 2014)

Lateral resolution is dependent on the Fresnel zone, the area of the wavefront from which the dominant part of the reflection originates. A given point of reflection reflects itself on a larger area the further away it propagates (Fig. 4a). This can be the case if the seismic transmitter is far away, or if the reflected surface is dipping away from its source (Lebedeva-Ivanova, et al., 2018). This is comparable to pointing a flashlight facing a blank surface like water. Knowing the lateral resolution limit is important, when understanding lateral variability like facies changes, channels, stratigraphic architecture (Lindsey, 1989). Diminishing the Fresnel zone can be achieved by reconstructing wave migration events, in either space or time, to the location the wave was reflected in the subsurface rather than the location it was recorded at the surface. This process is known as seismic migration and yields a more accurate seismic image (Sheriff, 1996). The Post-migration Fresnel zone can in theory be condensed to an ellipse with a minor axis radius of $\lambda/2$ in 2D seismic. In 3D seismic data it can be condensed into a circle with diameter $\lambda/2$ (Fig. 4b) (Kearey & Brooks, 1991; Sheriff, 1996).
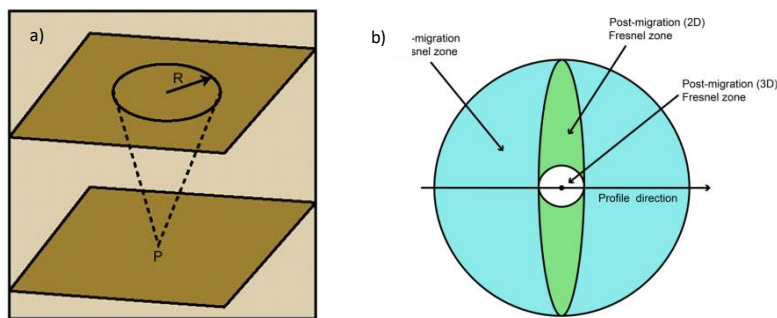
Figure 4: The Fresnel Zone. a) A given point of reflection reflects itself on a larger area the further away it propagates. b) The Post-migration Fresnel zone can in theory be condensed to an ellipse with a minor axis radius of $\lambda/2$ in 2D seismic. In 3D seismic data it can be condensed into a circle with diameter $\lambda/2$. From fig. 5 in Sheriff (1996)

Real seismic data contain a combination of signal and noise that may vary based on frequency, internal variations in lithology and microstructures. The noise is understood to be caused by vibration of the ground from the seismic wave (Simm & Bacon, 2014).

3.2 Seismic modelling

Due to the limitations of seismic resolution and dip-illumination, and lack of impedance contrast between the fault and surrounding rocks (Bond, 2015; Rotevatn & Fossen, 2011), many of the secondary fault structures that are involved in fluid leakage are difficult to detect in seismic (Andersen, 2020). To solve these problems, seismic modelling can be utilized. By modelling the seismic expression of a geomodel based on well/outcrop data, it can bridge the gap between field observations and seismic interpretation. This allows the study of how objects and processes that are below seismic resolution or for various reasons are hard to detect, affect the seismic image (Lecomte, et al., 2015). Based on studies of the modelled seismic, we can develop Seismic-modelling techniques that provide information on sensitivity and limitations of seismic data. Knowledge gained from these studies have the potential to improve our understanding of real seismic surveys (Anell, et al., 2016).

A multitude of methods can be used for seismic modelling. The most frequently used are:

a) 1D convolution modelling: Utilized in simple modelling of 1D models, such as modelling the trace of well logs. It is often used for correlating logs with subsurface seismic surveys. These are fast, efficient and require relatively little data. Their downside is the lack of detail as they do not address the effect of lateral variations on the reflectivity (though some measures can be made to account for this). As such it is a poor choice used for interpreting complex geology (Lecomte, et al., 2016)

b) 2(3D) full wavefield modelling: Finite difference modelling that generates complete synthetic seismograms based on solutions to the differential wave equation. It essentially models a seismic wave from the source as it is transmitted and reflected within the geomodel. This generates seismic that can be processed in the same way as real seismic data (Lecomte, et al., 2015; Lecomte, et al., 2016).

c) 2(3)D ray-based modelling: Here the full wavefield is not modelled, making this approach more cost and time effective compared to the above method. Instead of direct numerical solutions to the wave equation, the method follows ray theory, which is a high-frequency approximation of the wave equation (Lecomte, et al., 2015).

In this study, we apply a simplified version of the ray-based modelling, an analytical filter designed with a few key parameters. A Pre-Stack Depth Migration (PSDM) filter is used to generate seismic images using a Point-Spread Function (PSF). Pre-defined parameters such as angle of maximum illumination (ISR span) and a wavelet (Fig. 5a-c) are applied to the PSDM filter. This is a 2(3)D convolution method, where the PSF is used to produce reflectivity data for the model based on the geophysical input data. Reflectivity logs are extracted along vertical lines, each log being convolved

with a wavelet to form a synthetic trace (Fig. 5d) (Lecomte, et al., 2015; Lecomte, et al., 2016). The synthetic images show subsurface reflectivity in the depth domain unlike time domain in real seismic data. A coloured noise-model is generated by convolution of a random white reflectivity model with the same PSF as the synthetic seismic. The noise model reproduces the same filtering effect that the geological models get in the seismic modelling. (Faleide, et al., In review).

Setting a high ISR span and a high frequency wavelet allows for the generation of PSDM images that show perfect illumination (Fig. 5e). This allow us to model ideal seismic acquisition with resolution of a few meters (resolution of λ/4 laterally and vertically) and illumination of dips up to 90°. Such images will never be attainable in real life, as the angle of maximum illumination does not generally exceed 40-50°, and the lateral resolution cannot get smaller than λ/2, even in 3D seismic. (Lecomte, 2008; Lecomte, et al., 2015). These images are still very useful when compared to a realistic seismic image to find its limitations (Anell, et al., 2016).
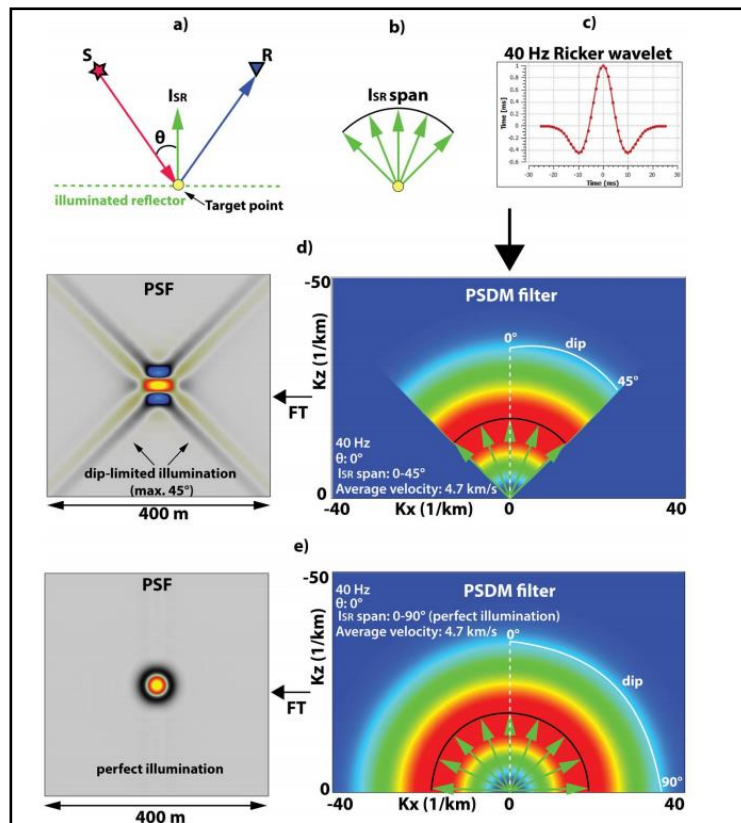
Figure 5: shows the parameters used for generating PSDM images from simulated PSF. a) A seismic survey shot through a target point is modelled based on survey information and velocity model. b) An ISR span can be used in the absence of survey information. c) A wavelet and frequency for the PSDM filter is determined. d) ISR span and wavelet are added to generate the PSF and PSDM filter with normal illumination (45°, the effect of dip limitations produces cross-pattern) and E) perfect illumination (90°, no cross-patterns). Modified from Lecomte, et al. (2015)

3.3 Fault zone architecture in siliciclastic rocks:

When studying fluid flow through a fault zone, the faults intrinsic architecture is a critical part to consider. Fault geometry can either restrict or enhance fluid migration, by acting as a barrier, conduit or a combination of the two (Braathen, et al., 2009; Dockrill & Shipton, 2010; Wibberly, et al., 2008). Fault zones are heterogeneous, and are generally divided into a central, narrow fault core, enveloped by a wider damage zone (Claine, et al., 1996). The fault core defines the boundary between the footwall and hanging-wall. Most of the throw of the fault is accumulated in the fault core, with only a few percent encountered in the damage zones (Schueller, et al., 2013). Therefore, the fault core is the most densely deformed part of the fault, and is often composed of fault gouge, fault breccia, cataclasites, lenses and diagenetic features (Braathen, et al., 2009; Torabi, et al., 2019; Wibberly, et al., 2008).

The fault core itself and the elements making up the fault core architecture are overall small and hence are not expected to yield any resolvable seismic signatures. Only lenses of a certain size could be resolvable (Childs, et al., 2009).

The damage zone is defined as the volume of deformed rocks around the fault surface (Kim, et al., 2004). Intensity of deformation increases as offset is accumulated and the fault continues to propagate (Shipton & Cowie, 2001). There is a non-linear relationship between damage zone width and fault throw. The damage zone also appears wider in the hanging wall than in the footwall as shown by Beach, et al. (1999) and later substantiated by Schueller, et al. (2013).

In siliciclastic fault zones, two different styles of brittle deformation occur. In Low porosity rocks, shear and tensile fractures are the dominant deformation structure, while in high-porosity facies, deformation bands are dominant (Fig. 6) (Fossen, et al., 2007.). In many cases, faults with large offsets are sealing, due to the presence of shale gauge on the slip surface, or clusters of deformation bands (Shipton & Cowie, 2001; Torabi, et al., 2019).
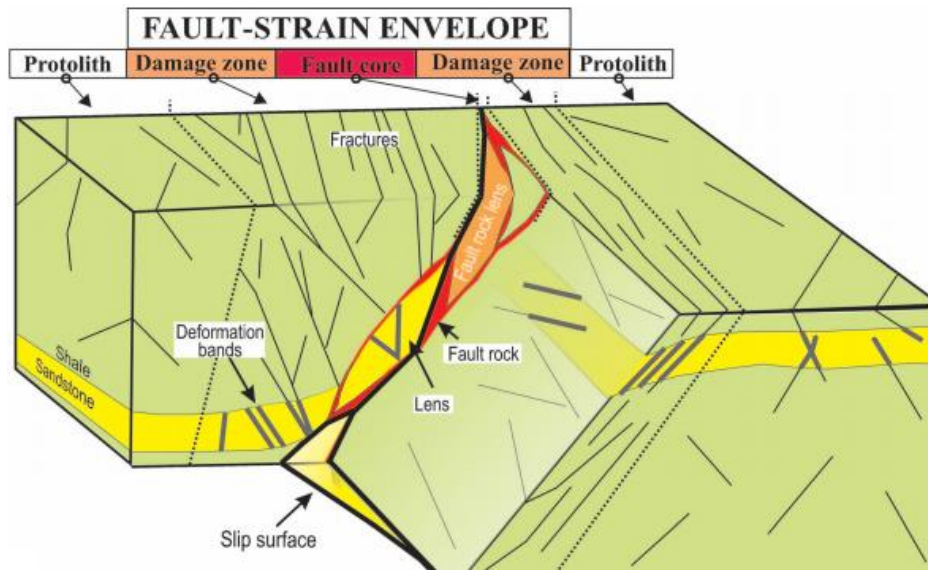
Figure 6: Illustration of typical normal fault architecture in siliciclastic strata. From Fig. 2a in (Braathen, et al., 2009)

Deformation bands are tabular structures that result from strain localization processes in high porosity rocks. Most common deformation bands cause lower porosity and permeability compared to the host rock. The thickness is usually at the millimetre (mm) to centimetre (cm) scale, and the offset is generally not greater than a few cm. They are formed by grain reorganization from different compaction or dilation mechanisms (Fossen, et al., 2007.) There are different types of bands, classified by either kinematics or by deformation. By compaction mechanisms and host rock porosity, they are Compaction bands, shear bands and dilation bands (Aydin, et al., 2006). The most common are shear-compaction bands. Deformation bands in damage zones are often clustered in the inner damage zone. A cluster is defined as decimetre-wide zones or swarms packed with deformation bands (Schueller, et al., 2013). Deformation bands, particularly compaction bands, may disrupt fluid flow due to their low permeability. When deformation bands cluster, they can form a low permeability envelope around the fault core, baffling fluid flow. This is discussed by Torabi & Fossen, (2007), Torabi, et al. (2013) and modelled by Fredman, et al. (2007), Fredman, et al. (2008), Shipton, et al. (2005), Tveranger, et al. (2007). Some studies indicate that compaction band clusters also has a potential effect on its seismic velocity due to its increased density, compared to its host rock (Fredericks, et al., 2013). Relationships between permeability and p-wave velocity of wet sandstones indicate a vague decrease in p-wave velocity in lab testing by Kassaba & Weller (2015).

Fractures are present in the fault damage zone. Faults propagate from a network of joints and micro-fractures when an applied stress exceed the rocks shear strength (Crider & Peacock, 2004). They can open in three different modes: from tensile stress, or shear stress acting in or out of the fracture plane. Shear fractures are common in fault damage zones and range in size from microcracks to faults in the

upper crust. The elastic properties and the shear strength of a rock mass changes as the unit is fractured. Fractures can also increase the fluid conductivity of tight sedimentary rocks (Boadu, 1997; Braathen, et al., 2020). The fractured damage zone is therefore expressed as a zone of increased permeability and reduced seismic velocity, compared to the host rock (Boadu & Long, 1996). Fractures can be bedding parallel or trough going depending on a variety of factors. Unlike high porosity sandstones, shales and siltstones have an anisotropic behaviour due to its bedding. Trough-going fractures is needed to form fracture corridors, that allow fluids to escape through a seal (Ogata, et al., 2013). Bedding parallel fractures typically enhance lateral flow due to the high permeability (lateral permeability of shales can be up to 900md) and low mechanical strength of the rock along its bedding, also making it prone to hydrofracking (Carey, et al., 2015; Major, et al., 2017). Micro cracks and cracks generally increase in frequency closer to the fault core, and drastically decrease seismic velocities (Gardner, et al., 1974).

3.4 CO_2, brine and rock interactions

When CO_2 is trapped in rock formations, it can behave differently depending on the reservoir depth, water solubility and CO_2 concentrations. It is generally dissolved in water up to the solubility limit, then the remaining CO_2 accumulate in a free gas cap due to the buoyancy of the lower density gas. Water solubility generally increase with depth and temperature, allowing deeper reservoir water to dissolve more CO_2, as well as increasing its acidity (Duan & Sun, 2003). At depths where the lithostatic pressure exceed 7.2 Mpa, it becomes a supercritical fluid (Fig. 7) (Desimone & Tumas, 2003). Deep geological storage of anthropogenic CO_2 will in most cases involve injection at depths more than 800 m, where the CO_2 is in a supercritical state. Compression of the gas to a supercritical fluid allows more CO_2 to be sequestered. This is due to the high-density of the fluid (~600 kg/m^3) relative to gaseous CO_2 and the reduced buoyancy forces in water-filled reservoirs (although the system maintains some buoyant drive between CO_2 and brine) (Benson, et al., 2005). In either case, a gas cap will accumulate beneath any effective seals, and be expressed by stronger impedance contrast in geophysical images (Shi, et al., 2013). In onshore, shallow analogues, CO_2 will be in a gaseous and dissolved state. Studies of the seismic response of CO_2 in porous sandstones, hypothesize that a free gas cap show a higher anomaly in geophysical images than a supercritical state fluid cap (Agofack, et al., 2018; Yamabe, et al., 2016).
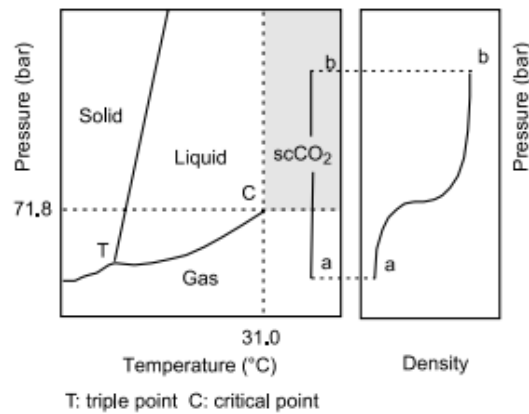
Figure 7: Phase diagram of co2 and its density as a function of pressure. From figure 3.1 in Desimone & Tumas (2003)

A common occurrence from long term CO_2 exposure in reservoirs is mineral precipitation of calcite. When water under high pressure is saturated with CO_2 it has a low PH value, yielding high solubility of calcite ($CaCO_3$). Calcite precipitation is a consequence of a pressure drop of CO_2 charged brine, causing degassing. Studies identify that this depressurization reduces calcite solubility in salt water, as well as removes CO_2 from solution, rising pH and cause $CaCO_3$ to precipitate (Tsujia, et al., 2019). Although mineralization affects the physical, hydraulic and elastic properties of rocks (Jarrard, et al., 2003) the evolution of these properties trough time has not been well characterized. Some studies indicate changes in permeability/porosity (Frery, et al., 2015; Manzocchi, et al., 1999) and imply that increased mineralization affects the fluid behaviour within geologic formations. This decrease in porosity is expected to increase total density of the reservoir, leading to a slight increase in P-wave velocity (Tsujia, et al., 2019).

Fracture stiffening is another effect of prolonged CO_2-brine-rock interaction. Low porosity siliciclastic rocks like shales and siltstones often display ductile behaviour when exposed to deformation and high shear stress (Skurtveit, et al., 2020). Fractures exposed to calcite precipitation stiffen and can thus recover 50% of its lost velocity, and maintain its initial permeability. This makes a CO_2 exposed, fractured damage zone less detectable in geophysical images, and more likely to persist as fluid conduits (Aben, et al., 2017).

Travertine deposits can form when the rate of CO_2 degassing is sufficiently high, and the brine contain the right precipitants (Pentecost, 2005). This normally happen when supersaturated fluids experience extremely rapid depressurization, an event generally only occurring when deep seated brine are ejected up to very shallow depths (Gratier, et al., 2012). The travertine can form veins that grow laterally from top to bottom or from centre to edge (Frery, et al., 2015; Gratier, et al., 2012). These veins thus have the ability to deform and uplift rocks, potentially fracturing effective seals and increase fluid connectivity (Gratier, et al., 2012).

Chapter 4: Data and methodology

This chapter gives an outline of the data and methods utilised to generate 2D synthetic seismic in this study. The basis of the geological models is a N-S cross section intersecting the central part of the Little Grand Wash Fault, near Crystal Geyser (Fig. 8). The cross-section is based on the latest updated Green River bedrock map by Burnside, et al. (2013), Heath (2004) and Kampman, et al. (2013) and is illustrated based on a wide variety of source-work listed in table 2. The methodology of generating synthetic seismic images from a 2D cross section is presented in chapter 4.1. The data background for the models is presented in section 4.2 and 4.3.
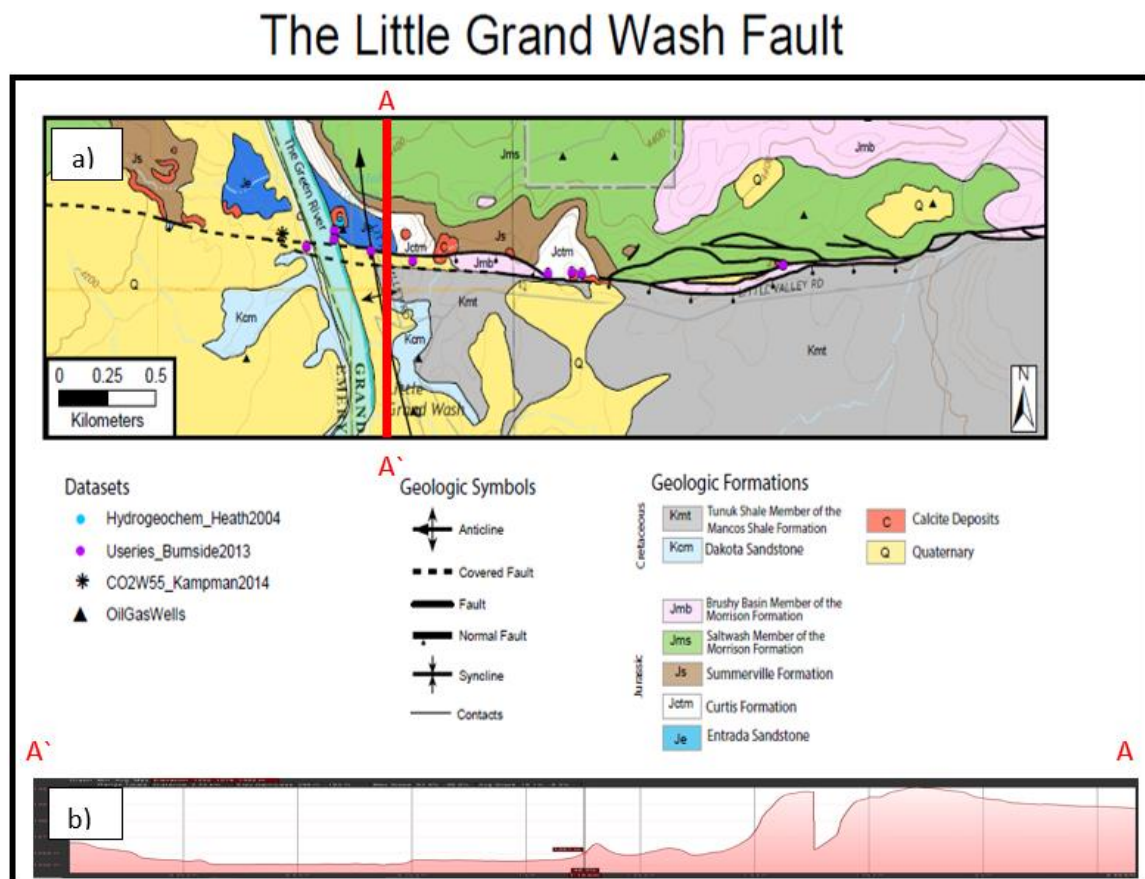
Figure 8: a) Bedrock map of the Little Grand Wash Fault, based on fieldwork (Burnside, et al., 2013; Kampman, et al., 2013; Heath, 2004) B) The basis of the geological models. A N-S cross section intersecting the central part of the Little Grand Wash Fault.

4.1 Methodology: Generating synthetic seismic

In this study, a 2D PSF-based convolution modelling approach was used to generate synthetic seismic sections of the LGWF in seismic modelling software. The theory behind the 2(3)D PSF-based convolution modelling approach is described in Chapter 3.2.

The interpreted geological models were illustrated in a graphical editing software. A numerical computing program, were used to associate the illustrated image is with elastic properties using a script that interpret the image colour codes. A script containing a series of functions for analysis and display of seismic data, has previously been modified to generate SEG-Y files (a SEG-Y file is a format designed for storing geophysical data developed by the Society of Exploration Geophysicists). The script generate these files based on data input of elastic properties and PNG files displayed in grayscale colours. In this study, the script is run using the numerical computing program matlab. The generated SEG-Y files are used as input in the seismic modelling program. Synthetic images were generated by using a PSDM filter, where geophysical parameter values, like wavelet, frequency and maximum angle of illumination is defined.

A step-by step explanation of the workflow going from Outcrop and well log data to 2D synthetic seismic images is provided in chapter 4.1.1-4.1.2.

4.1.1 Modelbuilding

2D cross-section models is created in a graphical editing software based on outcrop and well log data (Fig. 9 a-b). Adobe illustrator was utilized in this study. The project is set up as a pixelated format, where one pixel is equivalent to 1 m^2. This simplifies the transition from field outcrop and well data to the model, as most geological features like layer thicknesses and fault facies are stated in meters. This also allows for the addition of features that are smaller than seismic resolution. Such features may indirectly cause changes in reflectivity of nearby visible features. Studying such effects is a useful application of seismic modelling. Another aspect is that it allows for an easier definition of seismic sampling interval when modelling (one sample equal one pixel).

Each geological feature in the model that has different elastic properties compared to its surroundings is identified as a graphical object. The boundaries of each object are made sharp with no blank space in between. This is to avoid unidentified colours in the figure that can make the exported model inadequate at a later stage when using the numerical computing script. Before exporting the image in a PNG format, it is converted to grayscale colours (Fig. 9 c), which can be mathematically identified by the script. This allow each object in the model to be represented by a colour code between 0 and 255.

In the script different color coded objects are identified as "blocks". The different blocks are assigned elastic properties (V_p, V_s and density), which are needed for generating seismic reflections (Fig. 9 d). The matlab script converts 32 bit PNG files to SEG-Y files (Fig. 9 e). SEG-Y files store geophysical data within each graphic pixel. In this study, SEG-Y files for each of the elastic properties V_p, V_s and density is generated. V_s is calculated based on the input of V_p data from a pre-determined V_s/V_p ratio. The

density values generated in the Matlab script is derived from Gardner's relation (Eq. 2) (Gardner, et al., 1974).

Equation 2:

$$p = a\text{V}^{¼}$$

"*p*" equals overall density, "*v* " is equivalent to the primary wave velocity and "*a*" equals 0.31 when "*v*" is in m/s. This relation allows for the acoustic impedance to be estimated from velocity information exclusively. Thus p-wave velocity data is the primary input of elastic properties assigned to the objects of the model. In addition, a SEG-Y file containing seismic noise data (noise SEG-Y) is also generated.
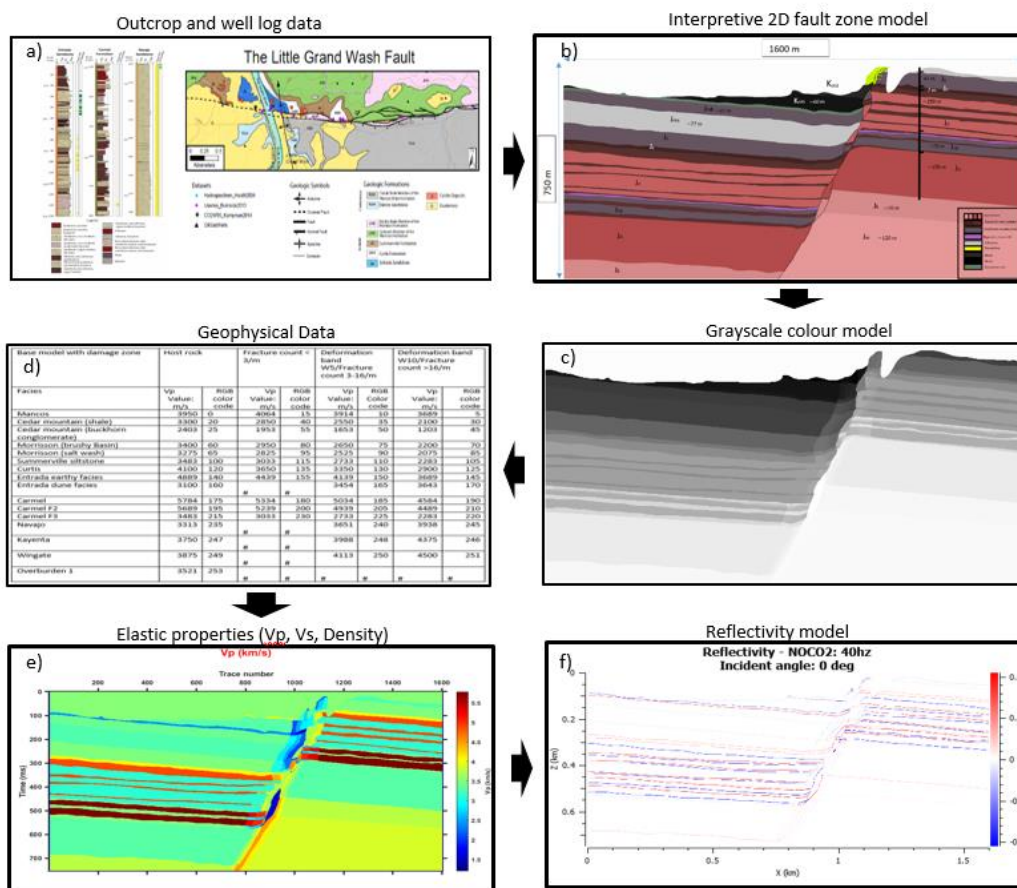
Figure 9: A workflow explaining the main steps going from outcrop and well log data to 2D reflectivity model. a) Examples of data utilized for building the geological model of LGWF. This data includes lithology, layer thicknesses, CO_2 concentrations, damage zone data, layer dips, densities and permeability. b) Interpreted cross section. One pixel is equivalent to 1 m^2 C) Grayscale colour model generated from b). D) Geophysical data is calculated based on a) or derived directly through seismic surveys, and associated to specific grayscale colour codes. e) Elastic properties are generated in the form of SEG-Y files. These are images where each pixel stores geophysical data. They are generated by merging c) and d) in numerical computing programs such as Matlab or Python. F) Reflectivity model is generated based on the SEG-y files in seismic modelling software.

4.1.2 Seismic modelling

In this study, the seismic modelling program SeisRoX was utilized. SeisRoX merge the generated SEG-Y files and the geological models to create a reflectivity model using the Zoeppritz equations (Shuey, 1985) (Fig. 9 f). The program generates synthetic PSDM images using an analytical PSF, which contain the necessary information on geophysical parameter values. The seismic images are presented using a Pixmap style. A "Seismic" colormap is chosen, where a peak (Positive AI contrast) correspond to a red reflector, and a trough (Negativ AI contrast) to blue (Fig. 10). This is equivalent to a European (Normal) polarity convention (Kearey & Brooks, 1991).
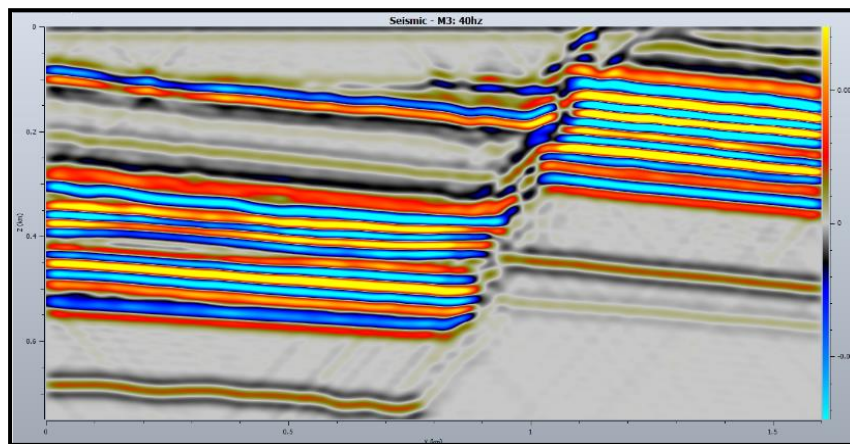
Figure 10: Output seismic model from modelling in SeisRoX. 2D Synthetic seismic is generated based on the reflectivity model in SeisRoX. Note the wavelet scale on the right hand side.

The sensitivity of the generated synthetic seismic to each model objects is tested. The testing is performed with variations in the following geophysical parameters:

Dominant frequency, level of noise and angle of maximum illumination.

Previous studies has determined these parameters to be the most relevant for fault zone illumination (Andersen, 2020; Anell, et al., 2016; Lecomte, 2008; Lecomte, et al., 2015). Other parameters such as the incident angle is set to 0-5° and wavelet type as Ricker wavelet. As the frequency, level of noise and angle of maximum illumination have been shown to be the most important during previous sensitivity testing (Andersen, 2020; Anell, et al., 2016; Lecomte, et al., 2015) alternative wavelets and incident angels where not tested. This is for the sake of the quantity of models and the capacity of this study.

Another script is utilized for calibrating the seismic data to the same wavelet scale. The wavelet scale is a measure that quantify the strength of peak or a trough. Calibration is achieved by creating a neutral SeisRoX Model, modelling a single reflector in the centre of the cross section we wish to calibrate (Fig. 11 a). This model is then used as a common reference that all the other models are calibrated to (Fig. 11b). This step is important when presenting the data. It allows for extrapolating the images for

comparison using the "difference plot" function in the 2D wiever (Fig. 11 c). This allow us to quantify any variations in reflectivity between the different models.

A final step in the modelling process is adding seismic noise to make the synthetic seismic more realistic and comparable to original seismic data. The noise model is calibrated to the same reflectivity range as the input geological model. Using the difference plot function, the signal-noise ratio is defined before images are merged and the final synthetic section is presented (Fig. 11 d).
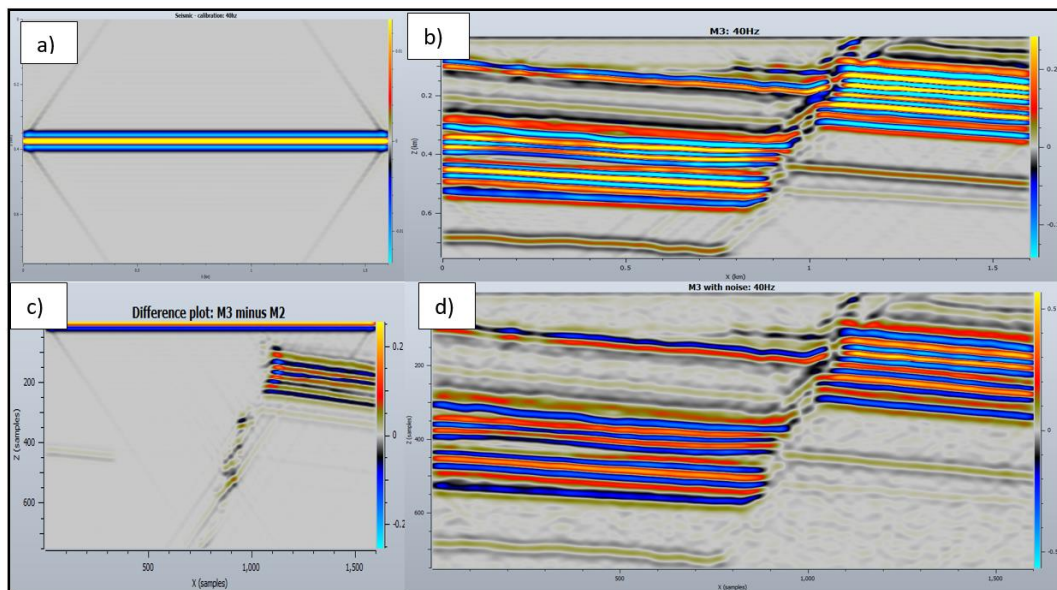
Figure 11: The synthetic seismic is calibrated to a similar amplitude scale range as the other studied models, a) Calibration model. A single reflector in the centre of the cross section. b) Calibrated version of figure 10. Note the wavelet scale on the right hand side. c) The difference plot function in SeisRoX´s 2D wiever window allow us to quantify any variations in reflectivity between the different models. d) Seismic noise is added using the difference plot function.

4.2 Data: Modelbuilding

This chapter address the background of the different objects within the models. This include structural and stratigraphic components of the cross section and the extent of the CO_2 plume. A variant with 1 kilometre overburden is also presented. The interpretations displayed in the 2D cross sections are supported by literature containing outcrop descriptions of lithology, geometry, and well log data. Where this information was missing, the model is supported by literature containing data from similar outcrops, lab studies of corresponding strata, and statistical approaches to the distribution of geological features. Each presented model is labelled M1 to M6. Corresponding Grayscale color model is attached in Appendix 1-6.

4.2.1 Base Model: M1

The base model (M1) address the Stratigraphic interpretations, and is presented in figure 13. The data background for the interpretations is presented in table 2. Thicknesses have been logged from the well CO2W55 (Kampman, et al., 2013; Skurtveit, et al., 2020). Where direct well data is not available, the thicknesses are based on outcrop observations in the area (Doelling, 2002; Greentown, 36-24H, 2009; Heath, 2004; Urquhart, 2011). Interpretations of recent fieldwork has corrected the fault throw in the central fault area to ~300m (Braathen & Liberty, 2020, Personal communication) The fault slip surface geometry is based on outcrop observations of the Moab fault segment in Bartlett wash, cutting trough the same stratigraphic units (Berg & Skar, 2005) (Fig. 15b). Where the lithology varies, primarily trough the Carmel-Entrada-curtis sequence, fault lenses are expected to occur (Berg & Skar, 2005). Trough the clean sandstone segments without significant clay mineral content, like the majority of the Navajo and Wingate Formation, an even fault slip surface is expected. This is due to the more homogeneous distribution of strain accommodated by the deformation bands (Torabi, et al., 2013). The fault lens between the kayenta and Navajo formation (Fig. 13) is added due to potentially tighter lithology of the kayenta formation (Averitt, et al., 1955). Facies-variations within the Carmel and Entrada formations are interpreted based on a well log from Kampman, et al. (2013) (Fig. 13). In the Entrada Sandstone two facies-variations were added: The Aeolian dune facies, and the "Earthy facies" (Skurtveit, et al., 2020). For the Carmel formation three different facies-variations were used based well logs interpretations in Kampman, et al. (2013): A tight facies characterized by interbedded silt/shale, a courser one of interbedded sand/silt and a thin layer of gypsum/evaporates.

Table 2: Stratigraphic overview with applied thicknesses used in model, and corresponding source work.

unit		Applied value in model	Source	Lithology
Tununk Member (K$_{mt}$)		350 m	(Doelling, 2002; Urquhart, 2011)	Shale
Cedar mountain Formation (Kcm)	Ruby Ranch Member	65 m	(Urquhart, 2011)	Shale
	Buckhorn conglomerate	5 m	(Doelling, 2002)	Conglomerate
Morrison Formation	Brushy Basin Member (J$_{mb}$)	135 m	(Urquhart, 2011)	Shale-silt
	Salt wash Member (J$_{ms}$)	90 m	(Urquhart, 2011)	silt-sand
Summerville Formation (J$_s$)		47 m	(Urquhart, 2011)	Silt
Curtis Formation (J$_c$)		7 m	(Urquhart, 2011)	Sand-Shale
Entrada Formation (J$_e$)		150 m	(Greentown, 36-24H, 2009; Kampman, et al., 2013; Skurtveit, et al., 2020)	Sand
Carmel Formation(J$_c$)		70 m	(Greentown, 36-24H, 2009; Kampman, et al., 2013; Pijnenburg, et al., 2015)	Silt-shale, evaporites
Navajo Formation (J$_n$)		150 m	(Greentown, 36-24H, 2009; Kampman, et al., 2013)	Sand
Kayenta Formation (J$_k$)		70 m	(Greentown, 36-24H, 2009)	Sand
Wingate Formation (J$_w$)		120 m	(Greentown, 36-24H, 2009)	Sand
Regional dip of strata (deg. °)		Sub-horizontal to 25°	(Dockrill & Shipton, 2010; Braathen & Liberty, Personal communication, 2020)	
Fault offset		300 m	(Braathen & Liberty, 2020 Personal communication)	
Fault lenses			(Berg & Skar, 2005)	
Travertine mound			(Frery, et al., 2015; Williams, 2005; Burnside, et al., 2013)	
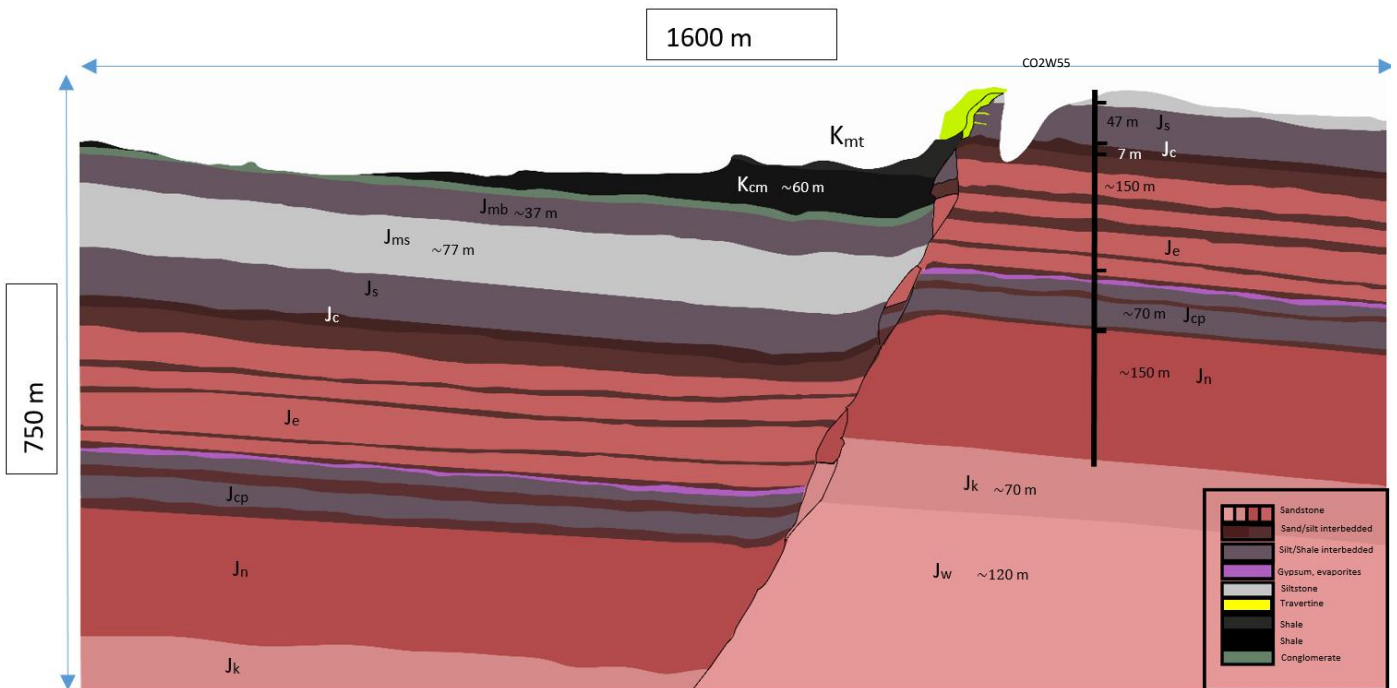
Figure 13: Graphical illustration of the base model (Model 1) of the N-S cross section through the LGWF. Its greyscale color equivalent is attached in appendix 2. Each object in this model is colour coded and classified by lithology described in the legend. Shale and sandstone has colour schemes, making it easier to differentiate between the different formations. The L4 travertine, mound east of the cross section is included.

4.2.2 Model including damage zone: M2

Model 2 display the fault damage zone. The damage zone is not defined by sharp boundaries, but by a gradual increase in fractures/deformation bands towards the fault core. Dividing the damage zone into zones of degree of deformation is therefore necessary to create realistic illumination of the damage zone. The fault damage zone is added in the form of object borders (Fig. 14). In this study, the siliciclastic damage zone objects is defined by its dominant style of deformation that is depending in the physical properties of the strata. In low porosity rocks, brittle shear and tensile fractures are expected to occur, while in high-porosity facies, deformation bands are expected to be dominant (Ogata, et al., 2013; Torabi, et al., 2020). The size of the damage zone within a given facies, is calculated based the dominant style of deformation. A dominantly fractured damage zone generally strain the rocks further away from the fault, versus a damage zone consisting primarily of deformation bands (Berg & Skar, 2005; Botter, et al., 2014). Fluid leakage is expected to occur through fracture corridors in tight rocks (Ogata, et al., 2013) evident by bleaching of rocks around such corridors. High porosity rocks are expected to form deformation bands that impede fluid flow. Near the fault core, a cluster of deformation bands can locally act as efficiently as a fault core slip zone when it comes to sealing capabilities (Torabi, et al., 2013). A mixed damage zone of deformations bands and fractures is not expressed in the damage zone size. This is done partly because seismic resolution will not be able to

resolve these nuances, and that they are already differentiated in damage zone velocities (described in chapter 4.3).
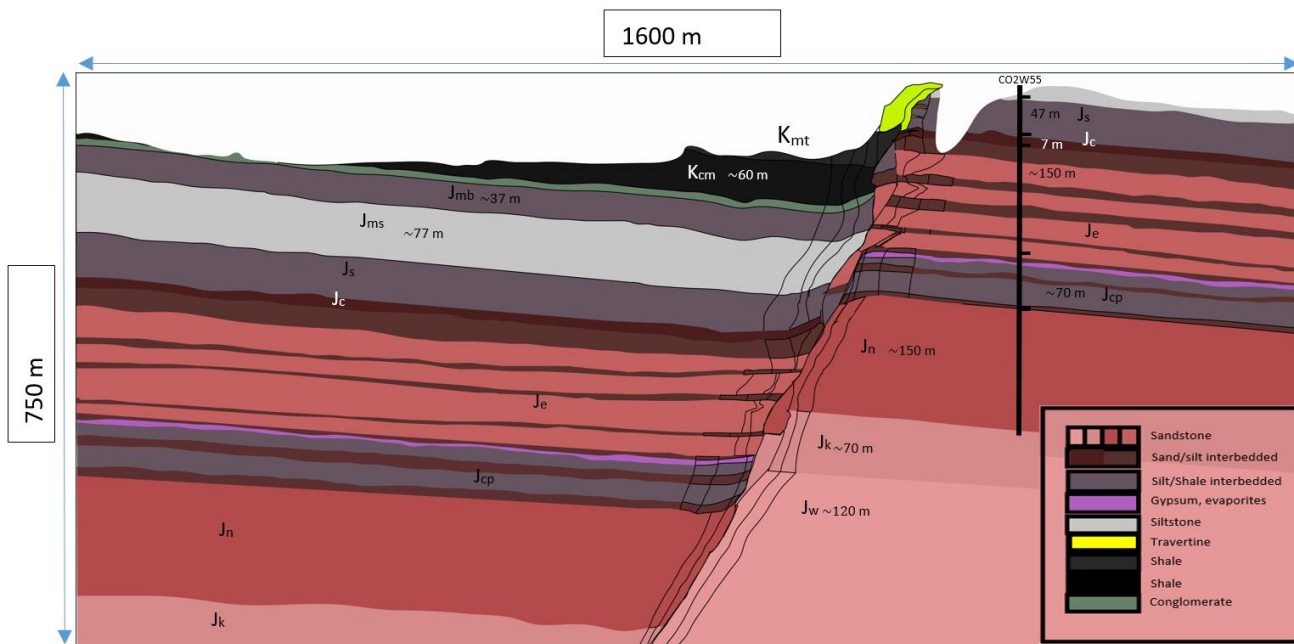
Figure 14: Graphical illustration of Model 2: The fault zone with added damage zone.

Where outcrop data was lacking, the size of the deformation band damage zone is derived from (Schueller, et al., 2013), a study that calculates several degrees of deformation based on 106 outcrops of similar faults in porous sandstones (Fig. 15a). The study reveals a non-linear relationship between damage zone width and fault throw, and concludes that the damage zone appears wider in the hanging wall than in the footwall, largely based on the distribution of deformation bands. The model presents a way of predicting damage zone width and deformation bands distribution based on fault throw. For the Entrada formation, outcrop data from the Moab fault segment in Bartlett wash, Utah (Berg & Skar, 2005) was utilized (Fig. 15b). The offset is lower than the LGWF (200m), yet the data is considered applicable for the use of this model, as damage zones of faults with displacement larger than 100 m cannot get wider indefinitely since developed faults localize most of the deformation to the slip surface, and can accumulate throw most efficiently (Torabi, et al., 2020). For this study, the distinction of an inner and outer damage zone was concluded. The inner damage zone is equivalent to Schueller, et al.´s (2013) definition of 10 deformation bands per meter (W10), while the outer zone is equivalent

to 5 deformation bands per meter (W5). Technically, the W1 damage zone defines the outer limit, but it is not expected to be detectable/visible in seismic, and is therefore not present in the model.
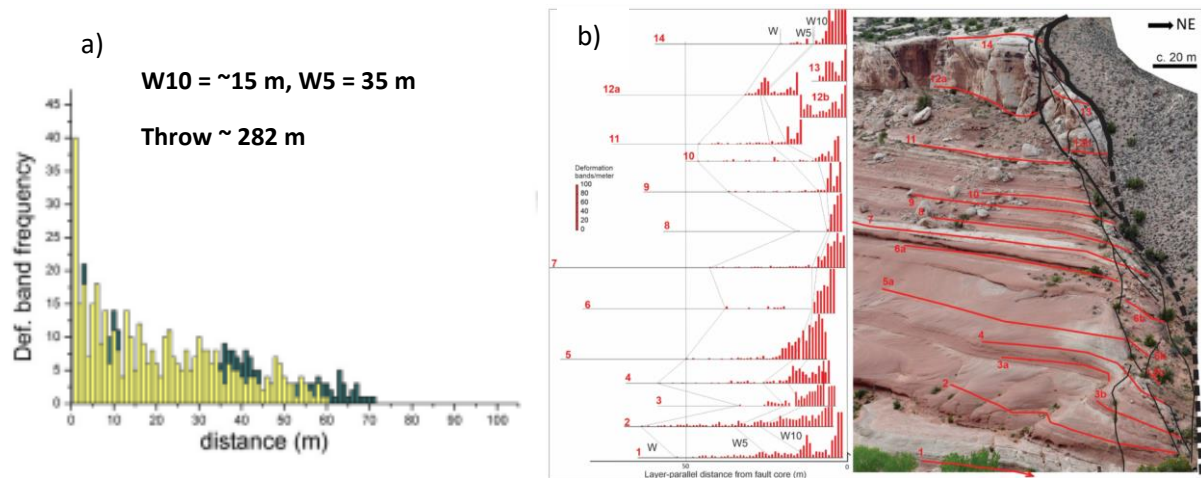
Figure 15: Damage zone width for high porosity stratigraphy. a) A damage zone size estimate of a fault offset of 282m, considered applicable the LGWF. Modified from Fig. 16 in Schueller, et al. (2013). b) Based on the 200m throw of the Moab fault segment in Bartlett wash, a deformation band damage zone size for the Entrada sequence is measured (Berg & Skar, 2005). This segment is also implying the presence of fault lenses within the same strata in the LGWF.

The size of the fractured damage zone is based on field outcrop data. The Moab Tongue unit in Bartlett Wash, is similar in lithology to the Curtis formation as it appear in Crystal Geyser (Zuchuat, et al., 2019a). Scanlines containing fracture data of this unit is used (Fig 16 a) (Torabi, et al., 2020). Fracture analysis from the upper strata in the LGWF is also performed by Dockrill & Shipton (2010). This dataset displays high fracture frequencies (>16/m) in the fault ramps, and inner damage zone (Fig 16 b). The fractured damage zone was divided into three zones of deformation based on these two outcrops. The outer Zone is defined by a linear fracture frequency of less than 3/m, the intermediate zone by 3-16/m and the inner zone is defined by a frequency of >16/m. A linear fracture count of more than 3/m was interpreted as statistically high enough to produce trough-going fractures, based on a study of fracture corridors by Ogata, et al. (2013). Bleaching In the "Earthy Facies" of the Entrada Formation support this estimate (Skurtveit, et al., 2020).
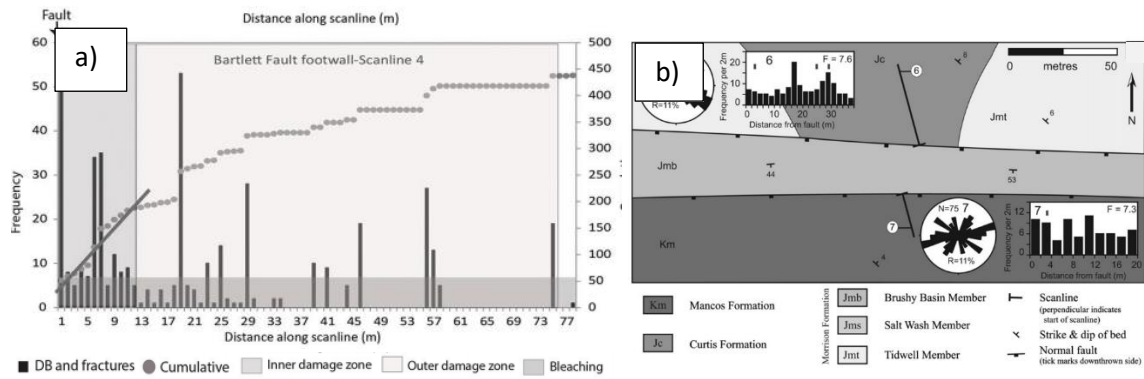
Figure 16: Fracture data used for building the damage zone of this model. a) Scanline "e" from the footwall of the Moab fault in Bartlett wash. The scanline contains fracture data for the Moab Tongue unit, and is considered an equivalent to the Curtis fm. Around the Crystal Geyser. The grey lines show the general slope of the cumulative distributions. Modified from Fig. 5 in Torabi, et al. (2020). b) Fracture data from the Mancos and Curtis formation used in this study. Modified from Fig. 4b in Dockrill & Shipton (2010)

4.2.3 Adding CO_2 fluid paths and mineralization: Model 3 and Model 4

Model 3 display the objects affected by CO_2 fluid paths and mineralization. For the resolution assigned to this model, CO_2 and mineralization do not cause any visible structural or stratigraphic changes, and therefore no new ojects are added. Their prescence is primarily expressed trough their effect on its host rock elastic properties, that is elaborated in chapter 4.3. The presence of CO_2 is expected to be constrained within the footwall of the fault as the fault core itself is considered sealing. (Torabi, et al., 2013) indicate that a deformation band cluster can theoretically withhold more than 80 m of oil column (a cluster is defined as decimeter-wide zones or swarms packed with deformation bands). In Schueller, et al. (2013), This is considered comparable to deformation degree of W10 or more. In this model, W10 is defined as a zone of reduced permeability comparable to the fault slip zone in the entrada sandstone. In the upper sequences juxtaposition analyses (Fig. 17) imply that shale smear gouge is expected to create a sealing fault core in the Entrada-Cedar mountain sequence (Dockrill & Shipton, 2010). A third argument for fault sealing capabilities is that mineralization and travertine deposits is almost exclusively observed in fault FW (Jung, et al., 2014). Therefore, CO_2 related features is limited to objects within the FW, primarily the high porosity reservoir units and the innermost fractured damage zone where the fracture count is statistically high enough to produce fracture corridors (Ogata, et al., 2013). Mineralization like bleaching occur within high porosity layers at most depths within our model, while travertine and calcite vein deposits are expected to primarily occur in the uppermost 10 meters (Pentecost, 2005). The model is presented in figure 18.
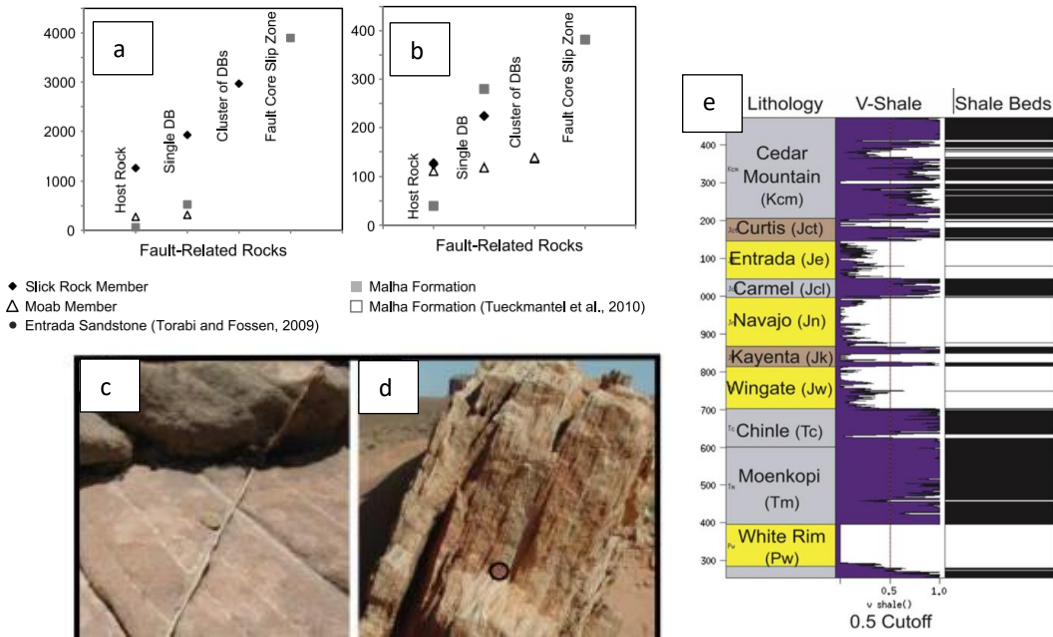
Figure 17: Evidence for fault sealing capabilities: a-b) The vertical axis on A is column height in cm maintained in a deformation band cluster from fig. 10 in Torabi, et al. (2013). Field data from Torabi & Fossen (2007) and Tueckmantel, et al. (2010) is also used. pictures of single deformation band (c) and band cluster (d) in the Entrada sandstone. From Fig. 1 in Torabi, et al. (2013) e) A juxtaposition analysis of LGWF by Dockrill & Shipton (2010) predict a representative V-shale curve that define the shale content of the stratigraphic sequences. modified from Fig. 7 in (Dockrill & Shipton, 2010).
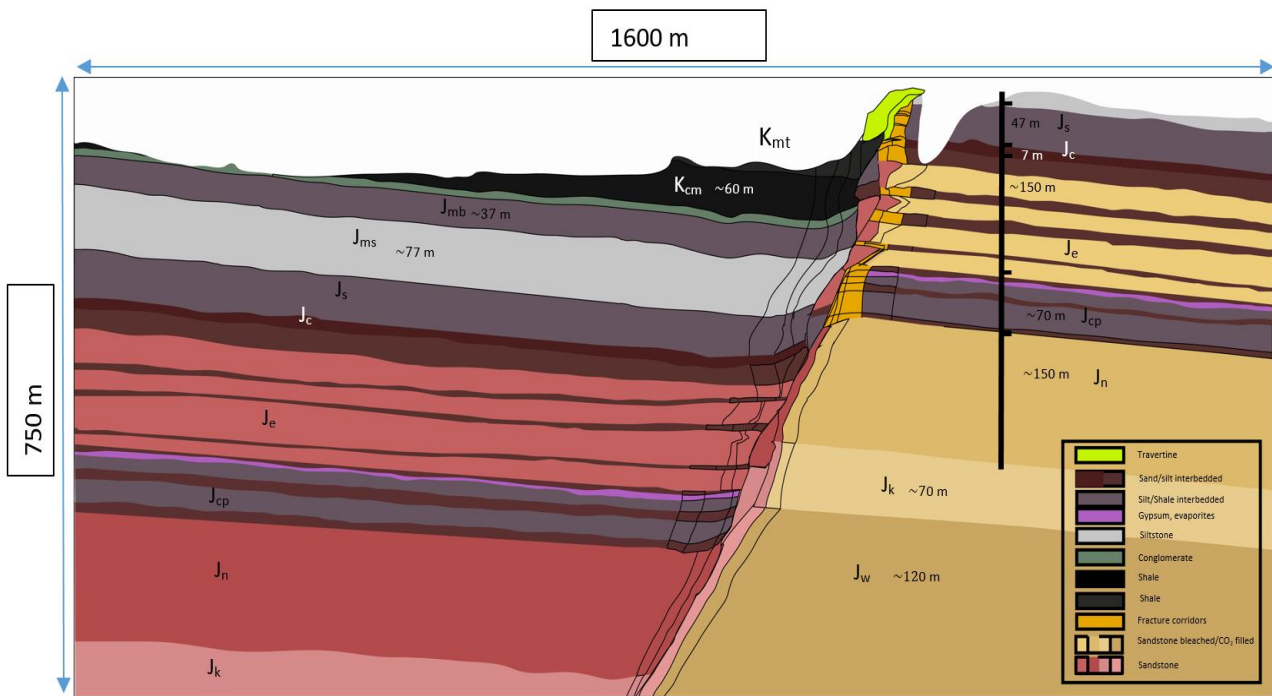
Figure 18: Graphical illustration of Model 3 and 4: The cross section with added damage zone and objects that are bleached and/or CO_2 filled (primarily in the Footwall in massive sandstones and innermost fractured damage zone where fracture count is high).

4.2.4 Overburden model: Model 5 and Model 6

The overburden models are designed to study the effect of supercritical CO_2, with 1 km of flat laying strata added. The upper strata of the Horda platform, imaged by seismic data of the Troll field, is used as a basis for illustrating the overburden. This is joined with the original/CO_2 filled model via adobe illustrators "image trace" function. The transition between the original geology and the overburden is achieved by extending K_{mt} and J_{ms} to create an angular unconformity. The added lithology is constrained to seafloor (loose sediment), dense rocks (shale) and high porosity rocks (sandstone). Bleaching and long term CO_2 exposure is not tested in this version of the model, it is primarily designed to target the geophysical expression of supercritical CO_2 leakage. The interpretive models M5 and M6 is presented (Fig. 19 and Fig. 20).
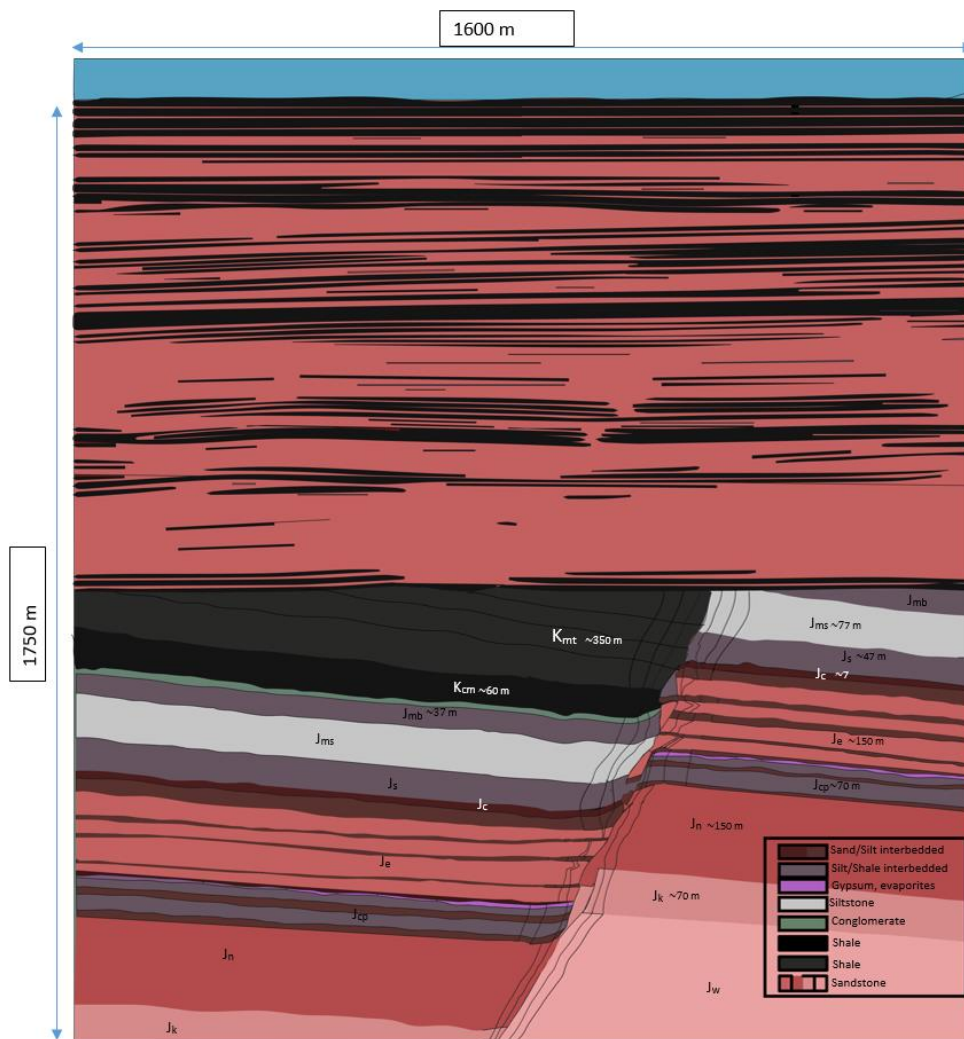
Figure 19: Graphical illustration of Model 5 (M5) designed for comparison with the CO_2 filled model, and to test the seismic response of the damage zone at reservoir depths. The overburden is based on the stratigraphic architecture of the upper kilometre of the Troll field. The lower model is the base model with damage zone. An angular unconformity is created to join the two geological sketches.
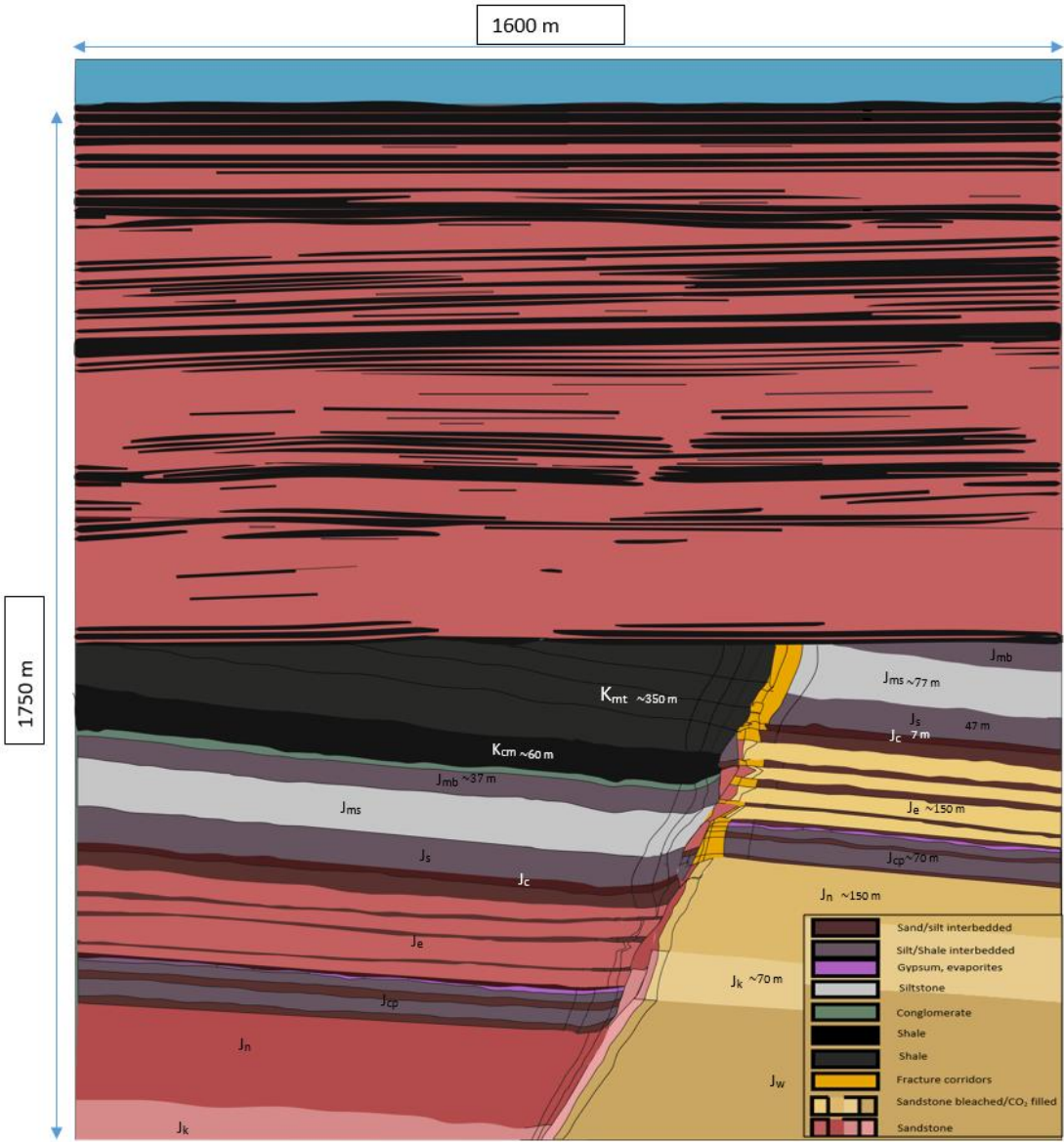
Figure 20: Graphical illustration of Model 6 (M6) designed to test the seismic response of supercritical CO_2. The overburden is based on the stratigraphic architecture of the upper kilometre of the Troll field. The lower model is the CO_2 filled model. An angular unconformity is created to join the two geological sketches.

4.3 Data: Elastic properties

This chapter address the data-background for the elastic properties assigned to each object in the different models. Applying CO_2 and mineralization to the models is achieved through assigning different elastic properties to the objects compared to the base models as these processes do not cause any visible structural or stratigraphic change. Velocity models displaying the estimated input V_p values for the models is attached in Appendix 1-6. Exact velocity calculations are attached in appendix 7-8.

4.3.1 Velocity of the stratigraphic units

Estimating the velocities for the stratigraphic units in the base-model, is attained either through direct measurement performed in past seismic surveys, or trough calculations based on total rock density.

A seismic survey on the salt valley anticline (Paradox Basin) was performed in 1978 by the United States Geological Survey (USGS) (Stockton & Balch, 1978). The survey provided velocity data on most of the Formations that are present in the upper LGWF. Not all values were considered applicable for our base model. The values for the Entrada Formation are likely slightly different in the salt-valley anticline than near Green River. The Dewey Bridge Member is described as red, earthy silty sadstone. This description is considered lithologicallly equivalent to the Curtis Formation near Crystal Geyser, as it is described in (Zuchuat, et al., 2019a). The Slick Rock Member is considered similar to the one in the LGWF. The following values were applied on these units in the base-model (table 3).

Table 3: Seismic survey by USGS providing Vp values. From table 1 in Stockton & Balch (1978).

Unit	Velocity: V_p m/s
Sandstone (Fine) Wingate	3875-4000
Navajo Sandstone	3850-3950
Kayenta Formation	3750-3900
Entrada (Slick Rock mbr.)	3100
Curtis (Dewey Bridge mbr)	4100
Summerville Formation	3200-3300
Morrisson Fm. (Brushy Basin member)	3400
Morrisson Fm. (Salt Wash member)	3275
Mancos Shale	3850-3950

For the cap rocks - The Earthy member and the Carmel Formation, there was limited amounts of data on elastic properties available. Therefore, a generalized approached was applied using Wyllie's

Equation (eq. 3). Similar to Gardners relation (eq. 2) it is most reliable when the rock is under substantial pressure, is saturated with brine, and contains well-cemented grains. Given that the burial depth at the time of deformation was around 3 km for these sequences (Fig 3), these equations are considered applicable.

Equation 3:

$$\frac{1}{v} = \frac{\varphi}{v_f} + \frac{1-\varphi}{v_m}$$

φ is the rock porosity, v_f is the pore fluid velocity, estimated as 1550 m/s for brine (Duan & Sun, 2003) and V_m is the rock matrix velocity. Porosity and density values for these units were provided from well CO2W55. Data for the Carmel formations silt/shale and silt/sand lithology's is described in table 4 (Pijnenburg, et al., 2015). Porosity and density of the "Earthy Member" was provided in (Skurtveit, et al., 2020) and (Pijnenburg, et al., 2015) (table 4). Based on this data, a mineral weight percentage composition based on thin section analyses was used to calculate a rock matrix density. A culmination of several lab experiments (Fig 21) have been used correlate rock matrix density with V_m (Sowers & Boyd, 2019). A total rock mass velocity (V_p) is calculated based on the porosity data and V_m using Wyllie's equation. These velocities are also listed in table 4.

Table 4: Calculated velocities for the Carmel formation and the Earthy facies of the Entrada formation. Mineralogy of facies from CO2W55 is used to calculate a total rock matrix density. From Table 5.1 in (Pijnenburg, et al., 2015) and table 1. in (Major, et al., 2017). The Sandy Carmel Claystone (reservoir interface) is used to calculate velocity for the coarser facies in the Carmel Formation described in (Kampman, et al., 2013). Abbreviations: Quarts (Qrtz.), Alkalie feldspar (K-Fsp), Calcite (Cal.), Dolomite (Dol.). Mineral densities from table 2 in Salazar, et al. (2014) is used when calculating rock matrix density.

Unit		Velocity : V_p m/s	Porosity	Qrtz (w%)	K-Fsp (w%)	Cal. (w%)	Dol. (w%)	Ilite (w%)	Other (w%)	Rock matrix density (g/cm^3)	Source
Earthy member		4600	7%	55	7	7	7	24		2.66	Major, et al., 2017; Skurtveit, et al., 2020
Carmel	Silt/Shale	5800	4%	5	4		8	79	4	2.80	Pijnenburg, et al., 2015
	Sand/Silt	4600	7%	20	14			65	1	2.61	Pijnenburg, et al., 2015
	Gypsum/ Evaporites	5700	5%						100	2.96	Sowers & Boyd, 2019
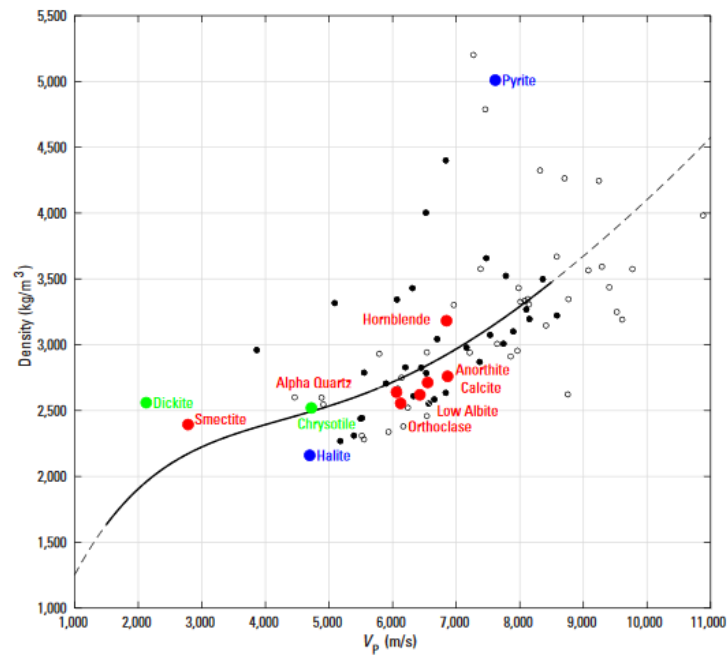
Figure 21: Rock matrix density and velocity correlations, from Fig. 1 in (Sowers & Boyd, 2019).

4.3.2 Damage zone velocity:

In order to apply a damage zone to the geological model, estimates on how the damage zone change the p-wave velocity compared to the protolith is necessary.

Fracture velocity change

The fractured damage zone is characterized by increased permeability and reduced seismic velocity, compared to the host rock (Boadu & Long, 1996; Fredman, et al., 2007). Micro cracks and cracks are expected to drastically decrease p-wave velocity (Gardner, et al., 1974). In tighter sedimentary rocks like the Curtis, Carmel, Summerville and Mancos formations a decrease in velocity is applied to the damage zone.

Authors that previously modelled damage zones in siliciclastic rocks estimate a V_p decrease of up to 45% compared to the host-rock velocity (Fig.22 a) (Botter, 2016). For the tightest rocks in the studied system, with high p-wave velocities, a 45% decrease was found to be too extreme. Therefore, When assessing the seismic velocity decrease of fractured rock, a liner fracture count-V_p correlation from (Boadu & Long, 1996) was applied (Fig. 22 b). In the innermost damage zone (>16 fracture/m) the velocity decrease was set to ~1200 m/s compared to the host rocks. The same velocity data is applied

in the fractured fault lenses. For the intermediate fractured damage zone, a velocity decrease of 750 m/s is applied. In the outer fractured damage zone, a decrease of 450 m/s is applied.

a)	Changes of V_P		Changes of V_S		Changes of ϕ	
	Max increase	Max decrease	Max increase	Max decrease	Max decrease	Max increase
Siliciclastics *Sigernes*	10–40 %	45 %	5–45 %	45 %	5–10 %	10 %
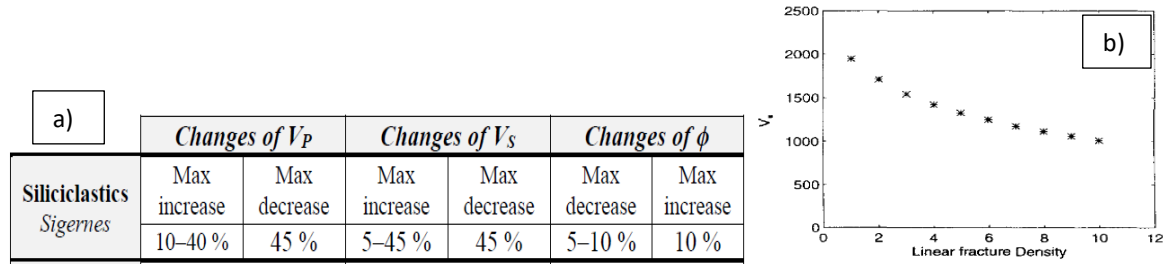
Figure 22: a) Approximate velocity changes in the fault core and inner damage zone compared to the protolith. From table 2 in (Botter, et al., 2014). b) A Linear fracture count and V_p correlation used in this study. From fig 11b in Boadu & Long (1996).

Deformation band and p-wave velocity

High porosity rocks like the Navajo sandstone and the Entrada dune facies generally have a damage zone consisting of deformation bands. In the model, the deformation band damage zone is expressed as areas of low degrees of mineralization by CO_2 and generally higher p-wave velocity (Shipton, et al., 2002; Torabi, et al., 2013; Tsujia, et al., 2019). This is because a certain number of deformation bands are compaction bands that cause a severely reduced porosity and permeability. Compaction bands are more likely to occur on high porosity units (Schueller, et al., 2013; Shipton & Cowie, 2001; Torabi & Fossen, 2007; Torabi, et al., 2013).

Velocity experiment on the Slick rock member lab samples, and in outcrop, is performed by Fredericks, et al. (2013) (Fig. 23). The innermost deformation band damage zone displays an increase in seismic velocity, although there are large porosity variations in deformation band dataset. For this study, the samples were considered comparable to the Navajo sandstone, that has a porosity of 18% (compared to 27% in the Slick Rock Member) (Torabi & Fossen, 2007). A general increase of 300 and 800 m/s was applied to these three units for the W5 and W10 respectively. The same estimates were applied to the Wingate Sandstone.

For the Kayenta formation, the abundance of compaction bands is expected to be less than in the aeolian units due to its finer lithology. The unit was considered lithologically comparable subaqueous units of the slick-rock member where velocity experiments are performed (Fredericks, et al., 2013) (fig. 23). Here a velocity increase of 200 m/s and 600 m/s is applied to W5 and W10 respectively. There is also expected to be a lack of mineralization from CO_2-charged brine in the W10 zone due to the reduction in fluid permeability described in (Torabi, et al., 2013; Shipton, et al., 2002; Fredman, et al., 2007). Therefore, the velocity effect of mineralization CO_2 and (outlined in chapter 4.3.3 and 4.3.4) is not applied here.
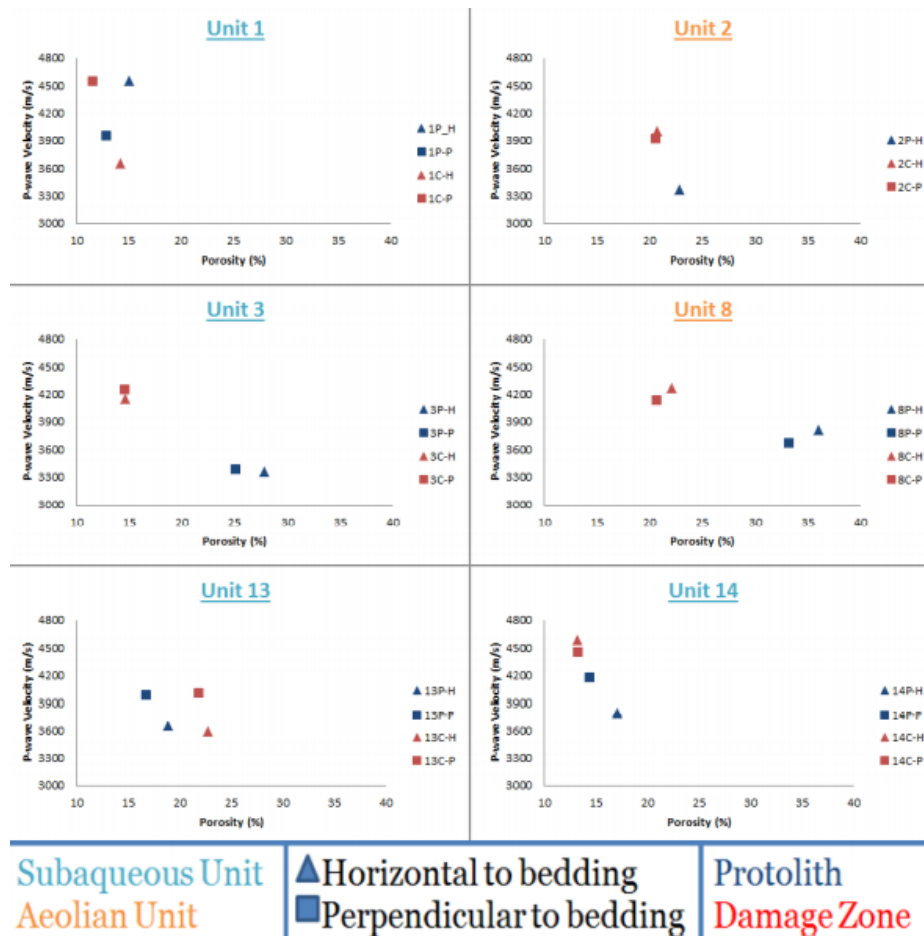
Figure 23: Data background for V_p estimates in the deformation band damage zone. Deformation bands cause a higher increase in p-wave velocity in the aeolian units compared to the subaqueous units. From (Fredericks, et al., 2013).

4.3.3 CO_2 plume velocities

This chapter address the effect of CO_2 on elastic properties of rocks.

4.3.3.1: Free CO_2

Studies show that P-wave velocity is reduced in the presence of CO_2. This is most clear in the presence of free gas in the pore space, but a reduction is also expected when it is dissolved in brine (Agofack, et al., 2018) and when occurring in a supercritical state (Yamabe, et al., 2016). A study by Agofack, et al. (2018) estimate a drop in V_p values of 300-400m/s depending on the degree of saturation of the free CO_2 gas (noted SCO_2). A decrease of 50-100 m/s is estimated when the pores are solely filled with brine saturated with CO_2 (Fig. 24). The p-wave dispersion remain relatively consistent for the frequency range 10-100Hz, however a slight increase in dispersion is seen at 40-50Hz frequency range (Fig. 24). The methodology that test the response of CO_2 at pore pressures up to 7.5 Mpa is used in this study.

The ratio of the volume of total CO_2 (free and dissolved, $V_{CO_2}^{Pf}$) over the total volume of fluid in the pore

space (V_f^{Pf}) is used to calculate SCO2 as defined in equation 4 (Agofack, et al., 2018). This equates to

the ratio of the volume of free CO_2 in the pore space ($V_{CO_2}^{free}$) over the total volume of the

pore fluid (V_f^{Pf}).

Equation 4:

$$S_{CO_2} = \frac{V_{CO_2}^{free}}{V_f^{Pf}} = 1 - \frac{V_{CO_2}^{Pf}}{V_f^{Pf}}$$

This method assume the CO_2 plume remains constant laterally within the objects it is applied to, ignoring any temporary concentration decrease from geyser eruptions. All volumetric values are calculated in liters since the data is given in molar mass/L.
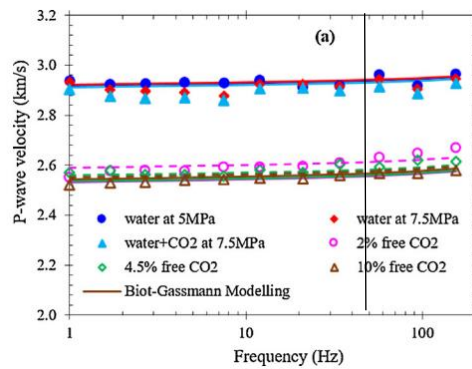
Figure 24: free co2 (SCO2) and assiciated v_p changes in a dry castlegate sandstone with porosity of 29%. This is deemed an acceptable analogue to the high porosity units in our model. Modified from fig. 13a in (Agofack, et al., 2018). Slight increase in dispersion is seen at 40-50Hz frequency range (black line).

Well log data from the LGWF report that free gas and CO_2-charged fluids were first encountered in the basal 35–150 m of the Entrada Sandstone (Kampman, et al., 2013). In this study, analysis of the CO_2 saturation was done, and a total saturation of mmol/L within the Navajo Sandstone was presented (Kampman, et al., 2013). For this study, this CO_2 concentration was expanded up into the Entrada Formation and down to the Wingate Formation so as to apply for the entire model. Based on the conclusions of Kampman, et al. (2013), the amount of free CO_2 gas was assumed to be >0% in the depth range of 35-150 meters (Fig. 25). Since the solubility of the brine increase with temperature and pressure, solubility values was estimated for a hydrostatic pressure gradient of 9.8 Mpa/km based on data from (Duan & Sun, 2003) (Fig 25).
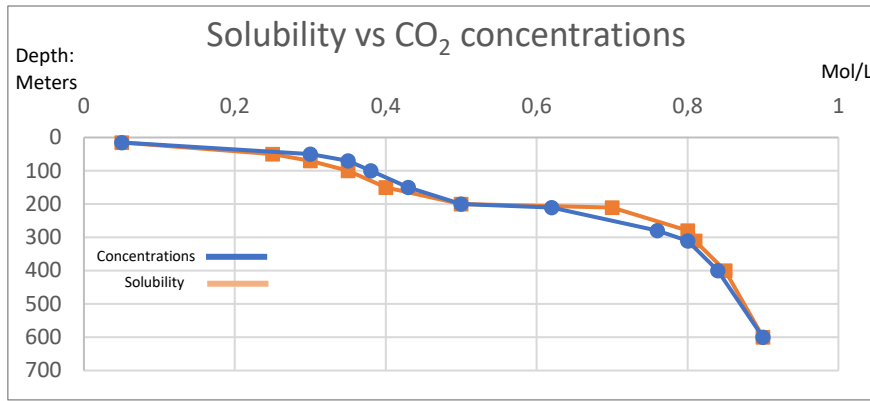
Figure 25: Calculated CO_2 Solubility in moles/L of NaCl rich water. Calculated based on a hydrostatic pressure gradient of 9.8 Mpa/km. From table 4 in *(Duan & Sun, 2003)*. Estimated CO_2 concentrations is also presented based on data from *(Kampman, et al., 2013)*.

To convert the molar difference between solubility and concentrations (Δn) into liters of $V_{CO_2}^{free}$, the ideal gas law was used (eq. 5):

Equation 5:

$$V = \frac{n*R*K}{p} = V_{CO_2}^{free} = \frac{\Delta n * 0.831 * K}{p\,(Mpa)}$$

Where *P*, *V* and *T* are pressure (Mpa), gas volume (Liter, in this case $V_{CO_2}^{free}$) and temperatures (Kelvin) respectively. *n* is molar mass, in this case it equals Δ*n*. *R* is a gas constant set to. 0.831 *L Mpa K⁻¹ mol⁻¹*. Concentrations given is in Mol/L. Therefore the pore fluid volume $V_f^{Pf} = 1$ Liter. Based on these estimates, four different zones of different CO_2 concentrations was applied.

Table 5: Estimated concentrations of S_{CO_2} and the associated anomalies, constrained to different depths. the molar difference between solubility and concentrations (Δn), pressure and temperature used to calculate this is also listed.

Δn	S_{CO_2}	V_p anomaly	Depth	Pressure (Mpa)	T (Kelvin)
0.05	2-3.5%	-300	35-70m	0.35-0.7	273
0.07-0.01	4.5-7%	-400	70-100m	0.7-1	273
0.05	2-3.5%	-300	100-150m	1-1.5	273
< 0	0	-150	150-600m	1.5-6	303

Velocity anomaly from free gas within fractures was also considered. Fracture porosity range from 0.1-5%, but is typically very low. (Tiab & Donaldson, 2016) For a 5% fracture porosity, that is theoretically possibly within the innermost damage zone, a slight decrease in V_p if free CO_2 concentrations exceed 5% (about -75m/s) is possible. Therefore, this anomaly is added to the "Earthy member" of the Entrada formation. For the outer damage zone, the porosity is too low to illuminate any free CO_2, meaning the effect on seismic reflectivity is neglible. (There may still, however, be highly effective conduits). The V_p/V_s ratio when free CO_2 is present is also reduced from 2 to 1.75 in the study by Agofack, et al. (2018).

This parameter was not possible to constrain to specific objects within our model, therefore it was not applied.

4.3.3.2: Supercritical CO2

For pressures above 7.5 Mpa, CO_2 exists in a supercritical state (Desimone & Tumas, 2003). For the model with an applied 1 km overburden, the normal rock velocities were unchanged, but the objects filled with dissolved and free CO_2 was replaced with V_p value estimates for a supercritical CO_2 plume. Fully saturated supercritical CO_2 can reduce velocity by up to 300m/s according to experiments done by Yamabe, et al. (2016) (Fig 26). This study model CO_2 distribution in random-distributed model where a CO_2 saturation of the pore volume = 50% and yield a V_p anomaly of -200m/s (Yamabe, et al., 2016). A fully saturated plume is estimated to have a V_p anomaly of -300m/s. Full saturation is applied where free CO_2 was highest in the normal model. The values used for the CO_2 filled overburden model is based on this study and listed in table 6.
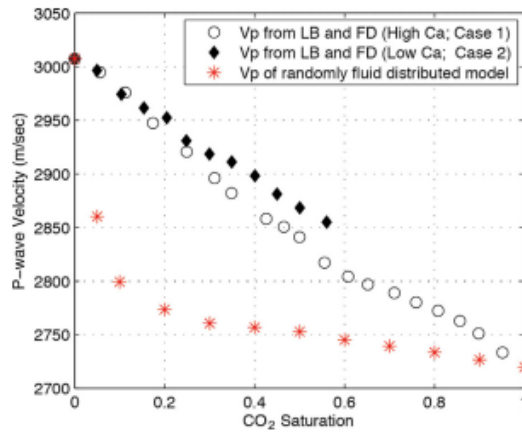
Figure 26: V_p anomalies in a porous rock containing a plume supercritical CO_2. The horizontal axis describe the saturation within the pores of the rock. For this study, anomalies related to saturations of 20%, 50 and 100% was applied. From fig. 4 in Yamabe, et al. (2016).

Table 6: V_p anomalies related to supercritical CO_2 plume

V_p anomaly	Depth	CO_2 Saturation
-150	35-70m	50%
-300	70-100m	100%
-150	100-150m	50%
-50	150-600m	20%

4.3.4 Mineralization:

The elastic properties of rocks are expected to be influenced by mineralization around the grains (chapter 3.4). Mineralogical changes in the Mancos, Entrada, Summerville and Carmel successions is presented in table 7 and based on XRD scans of well log data from CO2W55 (Major, et al., 2017;

Pijnenburg, et al., 2015). These data provide the mineralogical composition of these units due to CO_2 exposure, making it possible to calculate a rock matrix density and velocity using the same method as in chapter 4.3.1. Wyllie's equation (eq. 3) is then used to calculate a new total rock velocity. The Summerville formation is considered close in lithology to the Curtis formation, therefore the same change in velocity was applied there. The authors conclude that porosity is reduced with prolonged bleaching, and density is either reduced or increased based on the initial mineralogy and form of mineralization. This can produce either a net increase or decrease in velocity depending in which effect is dominant, which is reflected in the calculated values.

For the remaining units, a more generalized approach was applied based on porosity changes during mineralization. A recent study quantify the V_p anomaly in high porosity sandstones during mineralization, estimating an average net velocity increase of 300-1000 m/s depending on the porosity reduction (Tsujia, et al., 2019). However, it is concluded that seismic velocity changes vary strongly depending on mineralization types as well as rock types. This study was considered to overestimate the increase in P-wave velocity in the synthetic samples, compared to the Green River samples. Therefore, the more modest p-wave increase result for the Berea Sandstone (Fig. 27) was applied to this study.

A porosity reduction of 5-7% is estimated for the Navajo Sandstone by Pijnenburg, et al. (2015) compared to the unaltered host rock. Rock matrix density of the altered Navajo Sandstone was not available, therefore the V_p anomaly was calculated based on the method described above (Tsujia, et al., 2019). Since data was lacking, the same estimate was applied to the Kayenta and Wingate formations. The velocity of the CO_2 altered samples is presented in table 7.
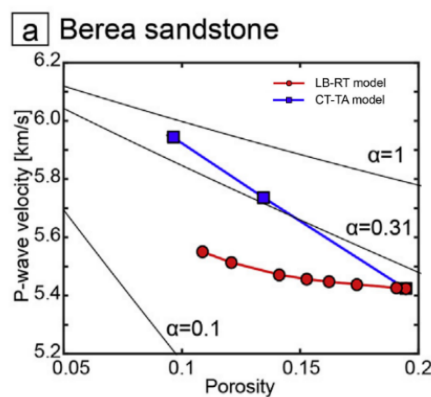
Figure 27: a) Evolution of V_p during mineralization in the Berea sandstone over a period of 25 days. This sample was considered the best estimate for the Green River samples. Modified from Fig.7b in Tsujia, et al. (2019).

Table 7: Velocity changes due to mineralization of rocks. Dataset used to calculate rock matrix density with prolonged CO_2 exposure is based on XRD mineralogical composition of tested samples in weight % from well CO2W55. From table. 1 in (Major, et al., 2017). b) Mineralogy of CO_2 exposed Carmel claystone is from table 5.1 in Pijnenburg, et al. (2015).

Samples (CO_2 exposed)	V_p anomaly (m/s)	Porosity Changes	Qrtz. (w%)	K-Fsp (w%)	Cal. (w%)	Dol. (w%)	Clays/Ilite (w%)	Source
Wingate Formation	+200							(Tsujia, et al., 2019)
Kayenta Formation	+200							(Tsujia, et al., 2019)
Navajo Formation	+200	-5-7%						(Pijnenburg, et al., 2015)
Carmel (F1) Formation	-500	-2-3%	6	3	2	8	81	(Pijnenburg, et al., 2015)
Entrada Formation (Slick rock mbr.)	+300	-8%	58	5	4	6	27	(Major, et al., 2017) (Torabi, et al., 2013)
Curtis Formation	-100							(Major, et al., 2017)
Summerville Formation	-100	-2%	32	17	38		13	(Major, et al., 2017)
Mancos Formation	+800	0%	16	6	61	1	15	(Major, et al., 2017)

During prolonged exposure to CO_2 and mineralization, fractures are expected to stiffen and reclaim 50% of its pre-damaged seismic velocity, in addition to being more resistant to closure and preserving permeability (Fig. 28) (Aben, et al., 2017; Skurtveit, et al., 2020). This recovery in velocity is added to the CO_2 exposed fractured damage zone.
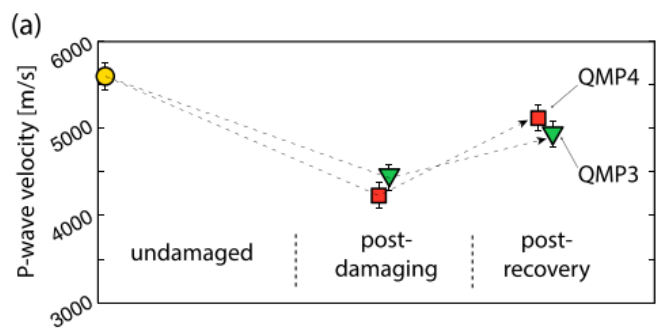
Figure 28: 64 day CO_2 exposure to fractured rock sample caused a 50% recovery in lost velocity. In this study, normal fault fractures decreased p-wave velocities by 26%. During mineralization, the velocity climbs back up by 13% giving a net decrease to 87% of pre deformed rock. From Fig 1. In Aben, et al. (2017).

4.4 Geophysical modelling parameters

The sensitivity of the generated synthetic seismic to the added CO_2, overburden and of damage zone was tested. A recent seismic survey of the area, 1km east of Crystal Geyser was conducted in November 2020. In the shallow CO_2 filled model, the geophysical parameters were adjusted to resemble this survey (Liberty et al, 2021). Where conditions differed from this survey, conventional seismic parameters were utilized. The following values of these parameters are:

i) Dominant frequency:

Base model:

A real seismic survey within the study area was performed in November 2020 (Liberty, Personal communication (2021)) The survey had centre frequencies of 50Hz, that in some cases reached 250hz. Based on this, and that a discrepancy in p-wave velocity is expected at 40Hz, the modelled frequencies is set at 40Hz, 100hz and 200Hz. For simplification, the frequencies are the same throughout the entire model.

Overburden model:

High resolution P-Cable seismic can provide imaging with frequencies ranging from 20-250 Hz depending on depth (Petersen, et al., 2010; Planke, et al., 2009). Conventional seismic frequencies of 80Hz were tested on the deep model. Below 1 km of overburden, the frequency is reduced to 40Hz as waves lose energy with travel time, and deeper parts of a seismic signal will have a lower frequency (Kearey & Brooks, 1991). P-cable frequency of 200hz that decreased to 100hz with depth were also used. 100Hz was considered attainable by p-cable technology at reservoir depths (Planke, et al., 2009).

ii) Level of noise: The testing is constrained to the object visibility with and without noise. The CO_2 flux building up to geyser eruption is expected to cause significant amount of noise (Liberty, Personal communication, 2021). Therefore, the level selected for the CO_2 filled models (M3 and M4) is set at 20%. Without free gas CO_2, noise is constrained to 15%, as this level was deemed comparable to conventional seismic.

iii) Angle of maximum illumination: 30°, 45° and 90° (perfect illumination) is tested.

Chapter 5: Results

The synthetic seismic images displaying the main results from this study are presented in figure 29-40. In the first section of the results (section 5.1), the effect of altering the frequency band, angle of illumination and adding seismic noise is addressed. This chapter presents optimal survey parameter values for ideal stratigraphic and fault zone resolution by testing the sensitivity of Model 1 and Model 2 (M1, M2).

Section 5.2 presents results dedicated to illuminating CO_2 leakage in the LGWF. The brine saturated/free CO_2 gas plume is illuminated by studying Model 3 (M3). The effect of mineralization of the stratigraphy is illuminated by studying Model 4 (M4). This chapter also correlates the objects related to CO_2 leakage with the modelled synthetic seismic. Seismic survey parameters aimed at targeting CO_2 leakage are also presented.

Section 5.3 is dedicated to illuminating the seismic response of leakage in a system comparable to a real storage-site at a suitable depth. Model 5 (M5) and Model 6 (M6), the LGWF with an added overburden and supercritical state CO_2 plume was studied. Building on the findings of section 5.2, similar synthetic signals of leakage as studied in M3 are targeted to illuminate supercritical CO_2 leakage.

5.1 Optimizing survey parameters:

M1 and M2 are used for seismic modelling of various dominant frequencies of the Ricker wavelet and angle of illumination. Section 5.1.1 addresses the vertical resolution of the stratigraphy in response to frequencies ranging between 40-200Hz and noise level of 15%. Chapter 5.1.2 address the visibility of the fault damage zone (DZ) and slip surface to the effect of frequency and angle of illumination ranging from 30° to 90° (perfect illumination).

5.1.1 Stratigraphic resolution: changing the dominant frequency and adding seismic noise.

The effects of adding seismic noise and changing the dominant frequency of the Ricker wavelet for synthetic seismic of M1 is recorded (Fig. 29). The frequency is altered between 40, 100 and 200 Hz. Noise causes a significant dimming effect on reflectors (Fig. 29 b, d, f). The Entrada Formation, that displays high internal impedance contrast internally (Fig. 29 a), is significantly dimmed in the presence of noise (Fig. 29 b). Increased frequency generally improves the overall resolution of M1.

The synthetic seismic log trace is compared to the model stratigraphy for the different frequencies (Fig. 30). The synthetic 40Hz image is not capable of distinguishing internal stratigraphic variations of

the Carmel and Entrada facies (Fig. 29 a, Fig. 30). The transition between the two formations is characterized by an increase in AI contrast (peaks and troughs are stronger). At the 100Hz frequency, most stratigraphic surfaces are resolvable, but thickness variations are difficult or impossible to constrain (Fig. 29 c, Fig. 30). Nearly all stratigraphic surfaces and thickness variations are illuminated at 200Hz (Fig. 29 e, Fig. 30).

M1 (40 hz)   M1 with noise (40 hz)

M1 (100 hz)   M1 with noise (100 hz)

M1 (200 hz)   M1 with noise (200 hz)
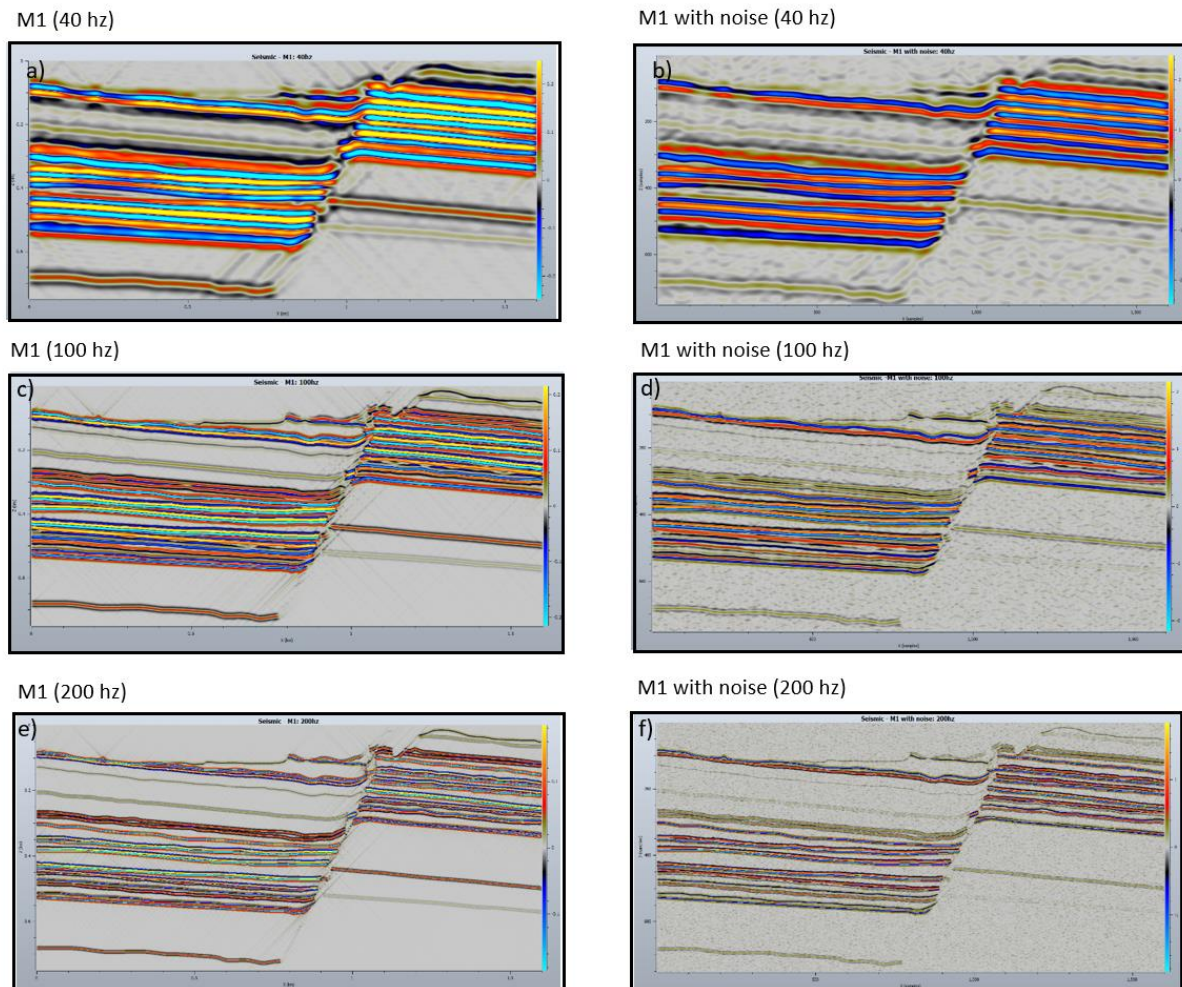
Figure 29: The effect of noise and frequencies of the stratigraphy of the base model (M1). a) 40Hz b) 40Hz with noise c) 100Hz d) 100Hz with noise e) 200Hz f) 200Hz with noise. Frequency increases the stratigraphic (vertical) resolution. Noise creates a significantly dimming effect on the impedance contrasts between the facies.
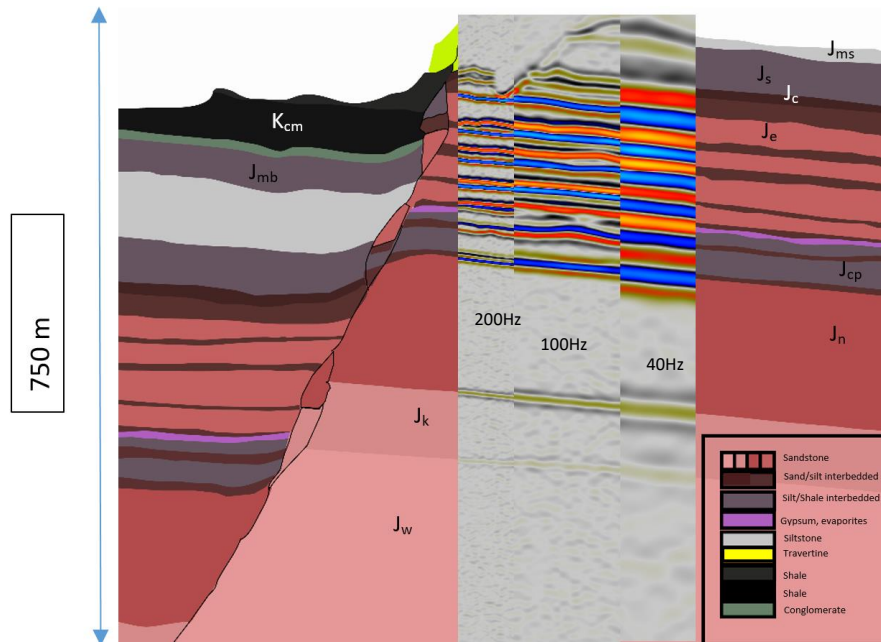
Figure 20: Synthetic trace at increased frequencies from 40 to 200Hz. Stratigraphic variations are illuminated with increased frequency. Nearly all units are resolved at 200Hz.

5.1.2 Fault zone resolution: the effect of dominant frequency and angle of illumination.

A portion of Model 2 focusing on the fault zone a range of frequencies from 40-200 Hz displays how, as the dominant frequency increases, the seismic resolution improves significantly (Fig. 31), The heterogeneity within the DZ starts to be resolved in the seismic (Fig. 31).

At a frequency of 40Hz, the fault zone is distinguishable from the surroundings. Several reflectors dim toward the fault zone (1: Fig. 31 a). A decrease in velocity discrepancy between facies, as deformation bands increase velocity while fractures decrease it, account for this dimming effect. Still, the fault is primarily visualized due to the offset of layers that can be correlated across the fault (Fig. 31 a). As frequencies increase to 100Hz a defined contrast between the DZ and protolith is observed (2: Fig. 31 b). The signals related to fault lenses also become clearer (3: Fig. 31 b). The slip surface is not possible to directly constrain as it is obscured by the DZ. (Fig. 31 b). The inner fractured DZ is resolvable from 200Hz as the lateral resolution increases. Objects associated with a defined velocity loss of 750-1200 m/s becomes visible (4: Fig. 31 c). These objects are associated with fracture corridors (see chapter 4, section 4.3.2).
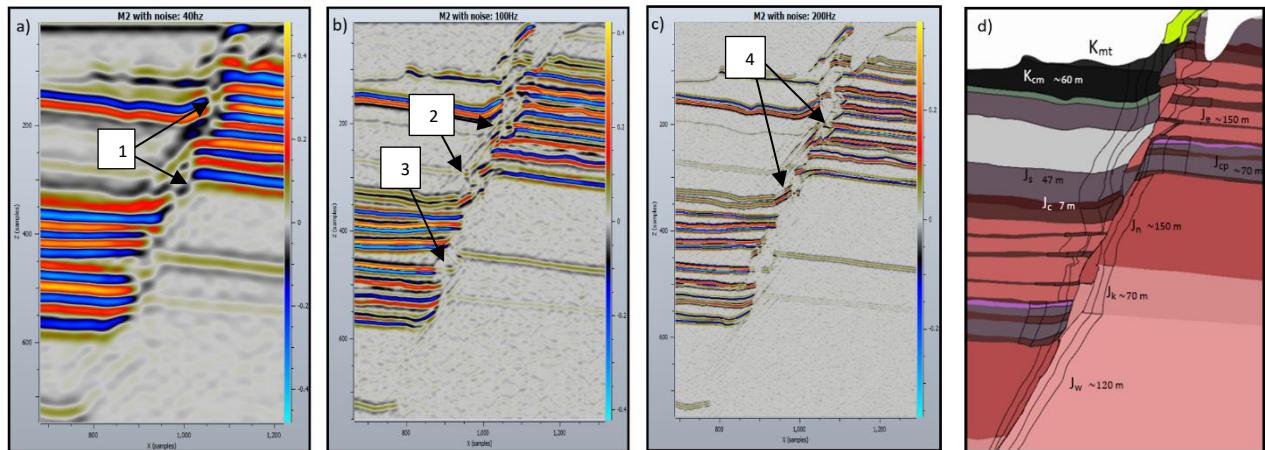
Figure 31: Damage zone resolution in response to dominant frequency a) 40Hz. Signal 1 highlighted b) 100Hz. signal 2-3 is highlighted. c) 200Hz. Signal 4 highlighted. d) Equivalent part of the graphical illustration of M2 for object reference.

M2 was also used to test the effect of changing the angle of illumination, as steeply dipping features unresolvable at low illumination angles are often fault related (Fig. 32). The optimum frequency for this depth, 200Hz, was used as it illuminated the majority of the damage zone (Fig. 31 c).

At 30° illuminations, the entire fault zone is characterized by cross patterns and the extent of the damage zone cannot be constrained (Fig. 32 a). At 45° this phenomenon is reduced to the fault zone, and the inner damage zone is visible (Fig. 32 b). The illumination of the folded layers in the hanging wall is also moderately improved with an increase in maximum illumination angle up to 45°. At perfect illumination (Fig. 32 c), no cross pattern occurs, and most objects of the fault DZ is visible. Angle of illumination show a significant impact on DZ visibility, as the inner fractured DZ, fault lenses and the fault slip surface is visible at perfect illumination.
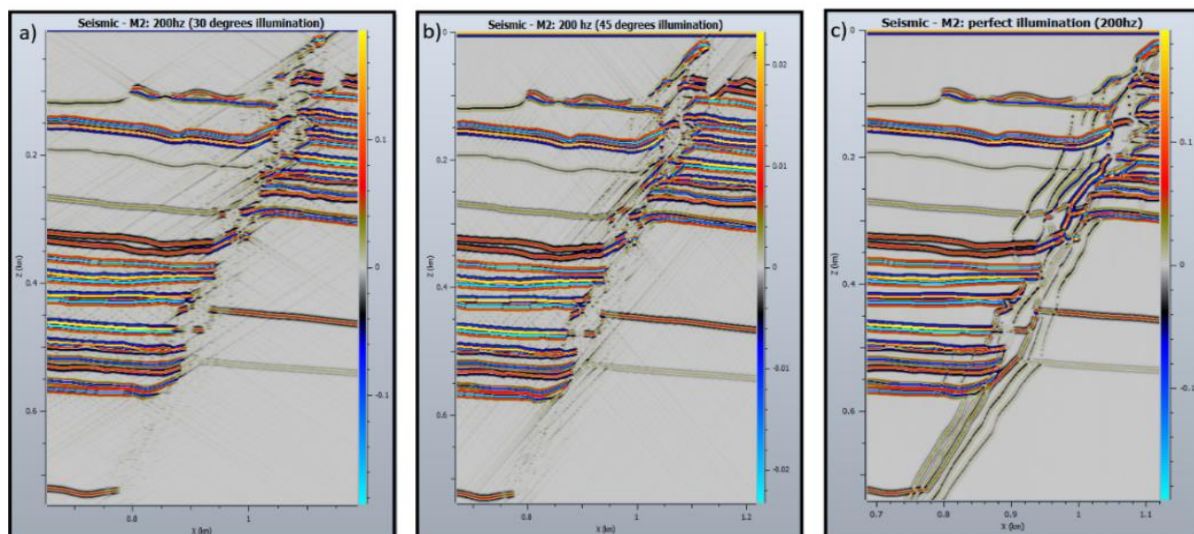
Figure 32: changing the angle of illumination - effect on DZ visibility. a) 30° illumination b) 45° illumination c) 90° (perfect) illumination.

5.2 Synthetic Seismic illumination of CO_2:

Models M2 - M4 is presented at high frequency (200Hz) seismic with a 45° illumination angle (Fig. 33). M3 records the addition of a CO_2 plume (Fig. 33 b). The difference between M2 and M3 is primarily visible in the fault zone (Fig. 33 a-b). The effects of mineralization (M4) illustrate a drastic decrease in impedance contrast in comparison to both M2 and M3 (Fig. 33 c). This effect is further addressed in section 5.2.2.

The corresponding difference plots shows that the CO_2 plume primarily affects reflectors in the fault footwall and inner damage zone (Fig. 34 a). The effect of mineralization produces reflectivity changes in the Carmel Formation in the hanging wall, as well as the fault zone and footwall (Fig. 34 b). The difference between M2 and M3 is illuminated by changing different parameters in section 5.2.1. The effects of mineralization is studied further in section 5.2.2.
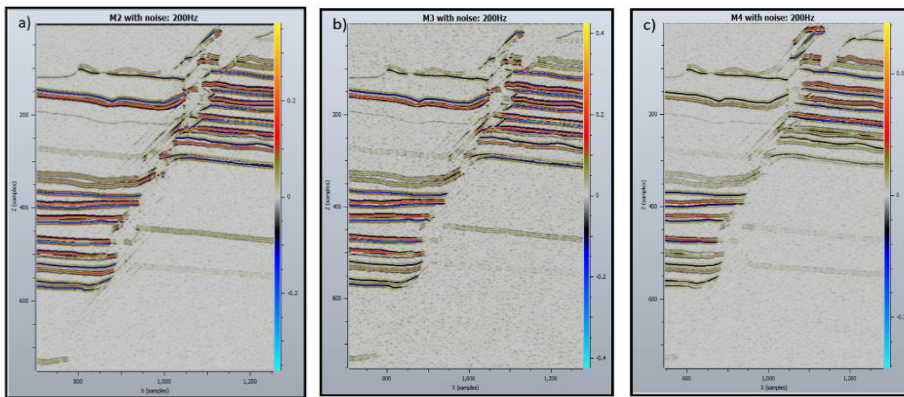
Figure 33: Progressive development of the LGWF. a) M2 added damage zone – for comparison b) M3 Added CO2 c) M4 Added bleaching
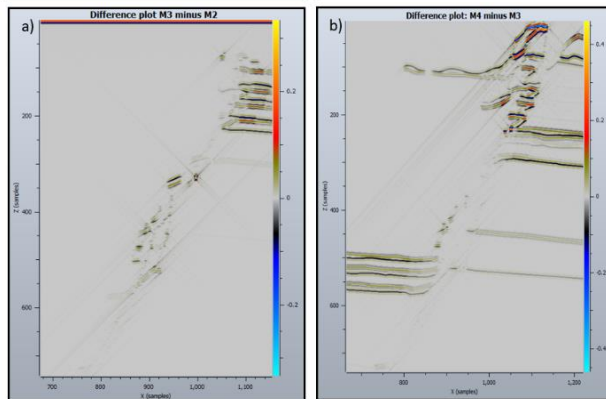
Figure 34: Corresponding difference plot between M2, M3 and M4 displaying objects that alter between each model. a) Adding CO_2. b) System after prolonged bleaching

5.2.1 Free CO_2 gas:

Figure 35 display M3 compared to M2 at different frequencies and angle of illuminations. Difference plots (Fig. 35 c, f) imply an increased contrast between fault facies and the Slick Rock-Earthy facies interfaces in the presence of free CO_2. The reflectors corresponding to the Navajo – Carmel interface also appear to be affected.

At 40 Hz and low illumination angles (30° illumination) no visible difference between M2 and M3 is observed. At higher frequency seismic (100Hz) the differrences between M2 and M3 is vaguely visible where a few reflectors are dimming close to the fault core (1: Fig. 35 e). Within the Navajo sandstone the DZ-protolith boundary appears slightly dimmer compared to M2 (2: Fig. 35 e). This corresponds to the velocity decrease of free CO_2 in the high porosity reservoir compared to the denser, unaffected inner DZ (W10). A few reflectors are affected across-fault (3: Fig. 35 e). No visible differrence is seen at the seal-bypass system at this scale, despite difference plots implying a differrence on the order of +- 0.1 (Fig. 35 f).
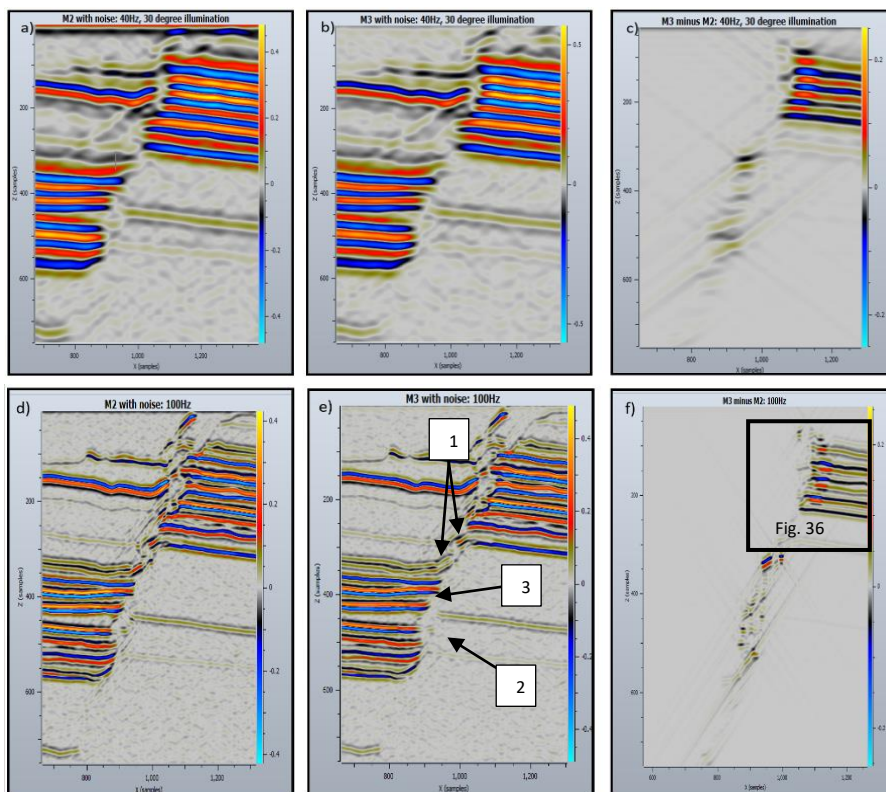
Figure 35: Increasing the angle of illumination and frequency, increase the visibility of the CO_2 plume. The signals of free CO_2 are vaguely visible at 100Hz frequency. a) M2: 40Hz, 30° illumination b) M3: 40Hz, 30° illuminations. c) Difference plot between a) and b). d) M2: 100Hz, 45° illumination e) M3: 100Hz, 45° illuminations. f) Difference plot between d) and e) and the extent of fig. 36.

Differrence plots image changes in the response between M2 and M3 in the seal-bypass system (Fig 35 f). This section is further studied (Fig. 36). Within the FW, the presence of free CO_2 appears to sligthly strengthen reflectors corresponding to reservoir-seal interfaces (4: Fig. 36 b). This effect CO_2 is vague. Increasing the frequency to 200Hz illuminate these reflectors within the fault damage zone, at the interfaces between the W5 DZ and the fracture DZ (3-9 f/m) (5: Fig. 36 d). These effects are on the scale of 5-20 m, and the amount of gas in this area correspond to 4.5% SCO_2 and a velocity decrease of 400 m/s. The same signal is much clearer in ideal seismic resolution, at frequencies of 200Hz, 0% noise and perfect illumination (6: Fig. 36 f). A few nearby reflectors are dimmed within objects that are unaffected by CO_2 (fault lenses, across fault objects) (7: Fig. 36 b, 8: Fig. 36 d).
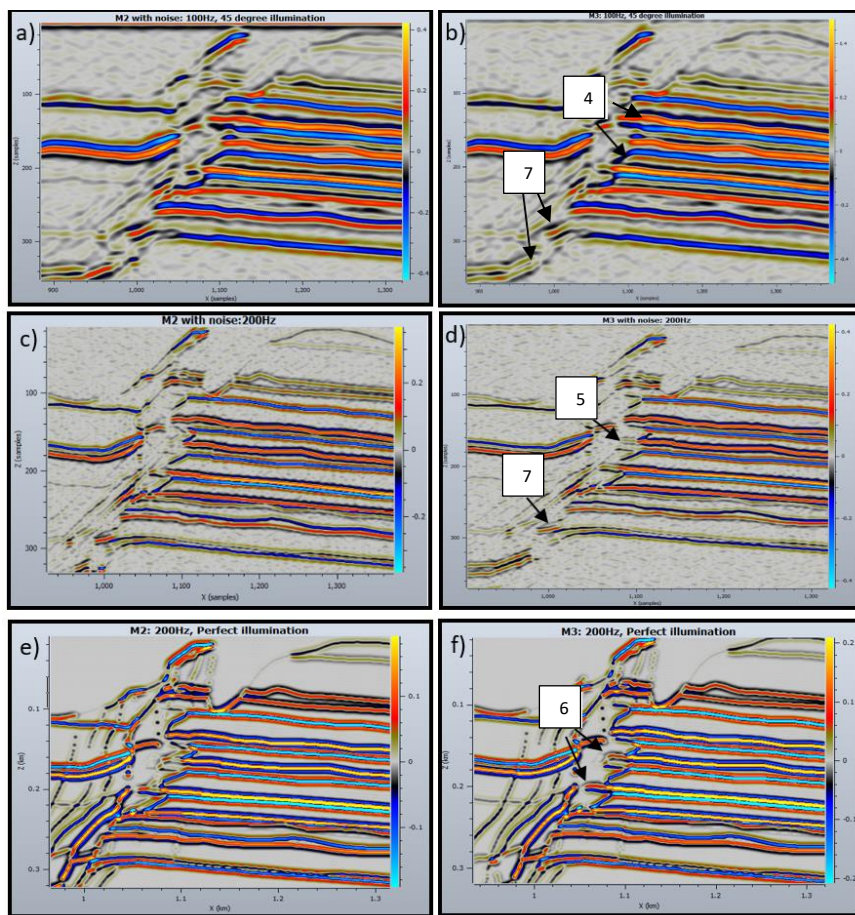
Figure 36: The seal-bypass system with added CO_2 (M3) compared to no CO_2 (M2) at different seismic survey parameters. a) M2: 100Hz, 45°illumination. b) M3: 100Hz, 45° illumination. Signal 4 and 7 highlighted. c) M2: 200Hz, 45° illumination. d) M3: 200Hz, 45° illumination. Signal 5 and 7 highlighted. e) M2: 200Hz, perfect illumination. f) M3: 200Hz, perfect illumination. Signal 6 highlighted. Differences between M2 and M3 are further illuminated in higher frequencies.

5.2.2 Extended exposure of CO_2

In this study, elastic properties are significantly affected by the mineralization occurring from CO_2-rock interactions (Chapter 4.3.4). Accordingly, the resulting geophysical images (Fig. 37) imply a significant dimming effect in the presence of mineralization compared to M3, particularly within the inner fault

damage zone (1: Fig. 37 a-b). Several reflectors are either weakened or not resolvable, particularly within the Carmel Formation (2: Fig. 37 b). The dimming effect of the DZ interfaces (3: Fig. 37 b) correspond to the fracture velocity recovery. A reverse in polarity is seen at the reflector corresponding to the Curtis-Summerville interface (4: Fig. 37 b). Overall, the mineralization produce a significant response (differrence of +- 0.4) in comparison to that of a system unaffected by CO_2 (Fig. 37 c).
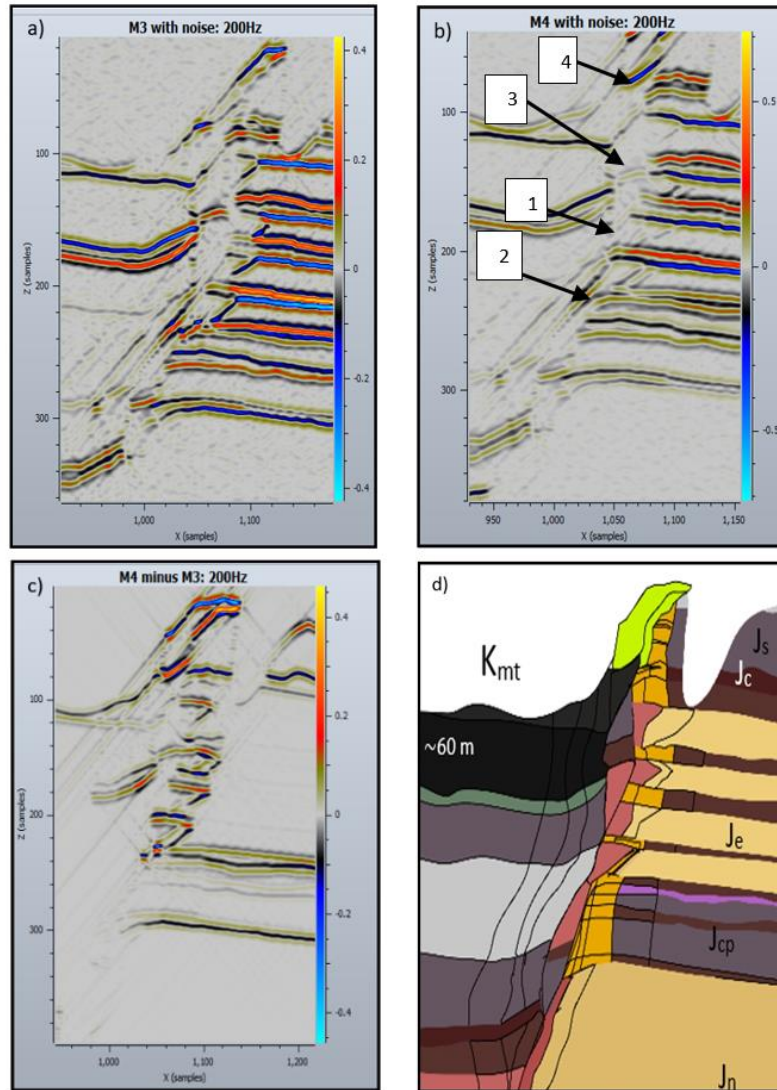
Figure 37: The effect of bleaching. a) M3, 200Hz b) M4, 200Hz. Signal 1-4 highlighted. c) difference plot between M3 and M4. d) Graphical illustration of M4 for object reference. Note that amplitude scale differs slightly for b), as the calibration script was not able to fully calibrate the amplitudes.

5.3 Supercritical CO_2 leakage:

An increase in impedance contrast is observed throughout the entire seismic section in the presence of supercritical CO_2. This is seen at both normal (40-80Hz) and high-frequency (100-200Hz) seismic (Fig. 38, frequencies are reduced with depth as explained in chapter 4.4). This presents some challenges.

Distinct overburden reflection affects the seismic image with an overall increased reflectivity of the surrounding strata, making it challenging to target the location of the CO_2 plume, and identify CO_2 leakage. This effect appears to be more problematic at higher frequencies (Fig. 38 d). All the synthetic seismic images contain coherent, strong reflections in the overburden. A reflector corresponding to the boundary between the overburden and the seafloor is altered in the presence of CO_2. (1: Fig. 38 b). Bright spots at the reflectors correspond to the interfaces between the Entrada Slick Rock and Earthy Facies Members is seen in the presence of CO_2 (2: Fig. 38 b).
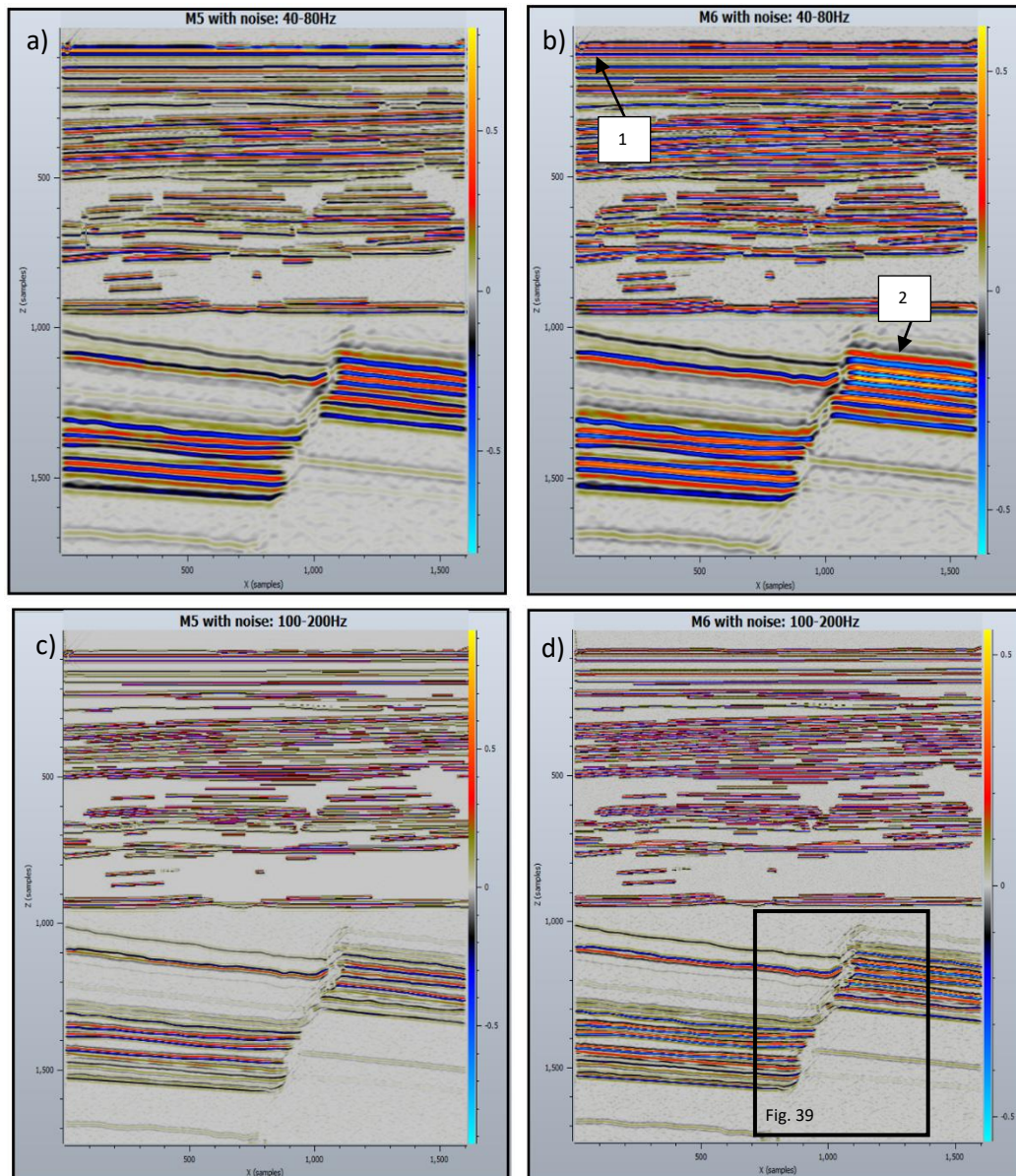
Figure 38: Model 5 and 6 display the system with an added overburden. The angle of illumination is set to 45˚. M6 (added CO_2) display increased reflectivity throughout the entire model compared to M5. This increased contrast is more localized at the 40Hz frequency. a) M5, 40-80Hz b) M6, 40-80HzHz c) M5, P-cable frequencies 100-200Hz d) M6, P-cable frequencies 100-200Hz. Note that amplitude scale differs slightly between M5 and M6 as the calibration script was not able to fully calibrate the amplitudes.

The fault damage zone can be detected even at 40Hz (3: Fig. 39 a). Focusing on the reservoir-seal interfaces it is possible to further study the bright spots, and recognize that the signal is similar to M3. These signals are also more localized to the objects related to leakage, compared to higher frequency seismic. (4: Fig. 39 b, d). At the 100Hz frequency seismic, the contrast is stronger between the DZ and the protolith in the presence of CO_2 (5: Fig. 39 d). Similar to M3, the interfaces between the W5 zones and the fracture DZ (3-9 f/m) correspond to this outer boundary, as reflectors start to dim at this point. This corresponds to the decreased velocity discrepancy between seal and reservoir, as fracture decrease seal velocity, while DB increase reservoir velocity. Similar to M3, increased impedance contrast between reservoir-seal interfaces in the DZ are observed in the presence of supercritical CO_2 (6: Fig. 39 d). The overall impact of CO_2 on reflectors throughout the entire system is more dominant in the high frequency, high illumination seismic (Fig. 39 d, Fig. 38 d). Reflectors are affected across the entire fault zone, making the interpretations presented (Fig. 39 d) of questionable accuracy.
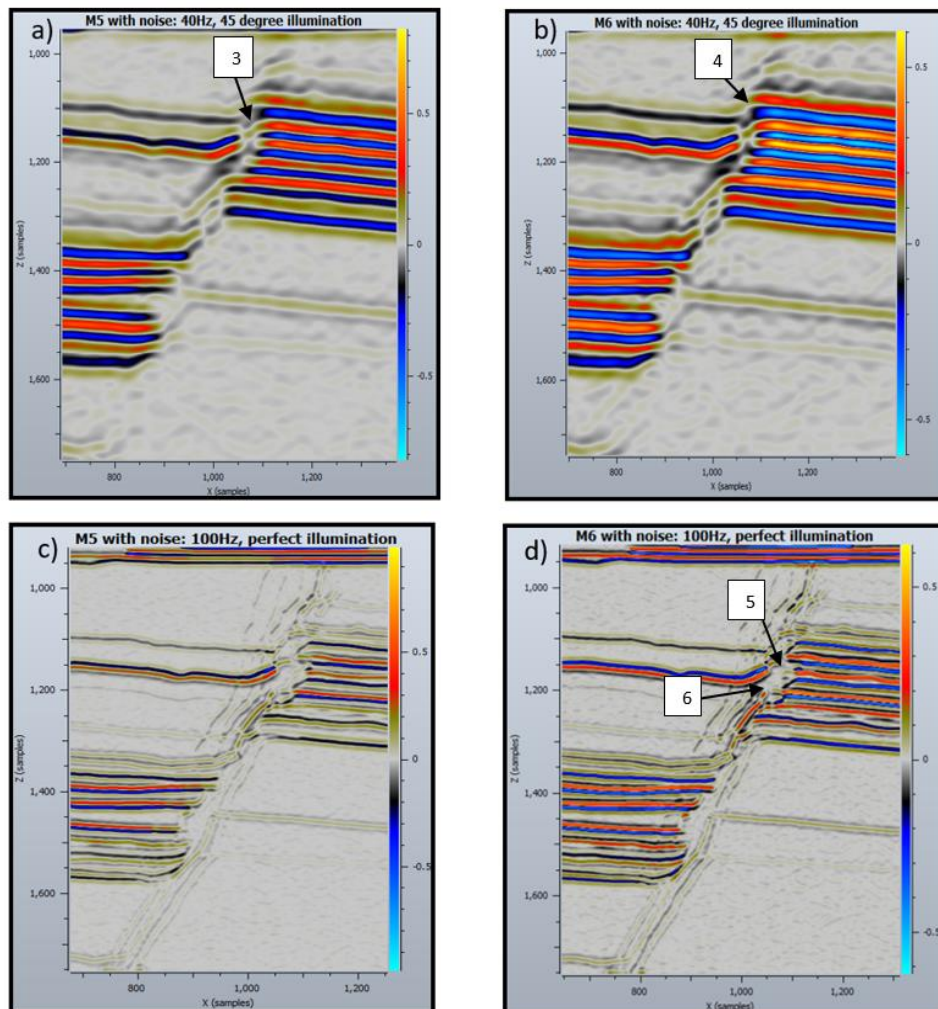
Figure 39: In both frequencies, adding CO_2 affect the entire system with increased impedance contrast. However, for the intermediate frequencies (40Hz) the CO_2 plume is more localized to the objects related to leakage. a) M5 40Hz. 45° illumination b) M6 40Hz. 45° illumination c) M5 100Hz. 90° illumination d) M6 100Hz. 90° illumination. Note that amplitude scale differs slightly between Model 5 and 6, as the calibration script was not able to fully calibrate the amplitudes.

Calibration of amplitudes for Model 5 and Model 6 was challenging using the method outlined in chapter 4.1.2. This issue was concluded to be noise-related, as the noise-free models was better calibrated. Therefore, some of the signal observations in figure 39 was verified using the noise-free synthetic images (Fig. 40).
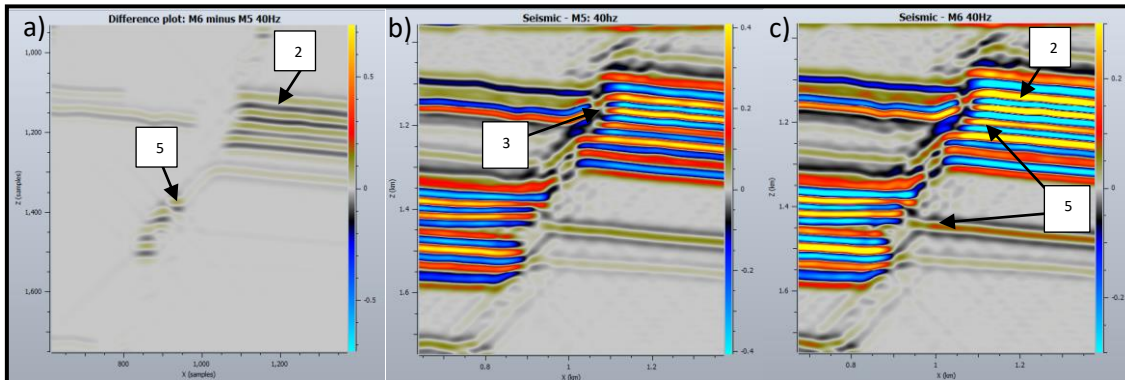
Figure 40: Noise-free versions of models 5 and 6 were better calibrated to the same amplitude scale. They were therefore utilized to verify some signals related to leakage. Signal 3, 2 and 5 were recognized. a) Zoomed in difference plot between Model 5 and Model 6 illustrating differences in impedance contrast in the fault FW, DZ and upper tight rocks in the HW. Signal 2, 5 is highlighted b) Zoomed in part of Model 5 (Without CO_2) at a frequency of 40 Hz. Signal 3 is highlighted. C) Model 6 (CO_2 filled model) with recognised signal2, 5 related to CO_2 plume

5.4 Result summary:

The main findings of this study can be summarised by the following observations:

a) Stratigraphic variations and fault architecture are easier to resolve in high frequency seismic (100-200Hz) compared to intermediate frequencies (40-80Hz). The level of noise has a dimming effect on stratigraphic reflectivity and overall resolution. High illumination angle increase the visibility (resolvability) of the entire fault zone. This applies to all models.

b) Increasingly dimmer reflectors toward the inner fault damage zone characterize objects corresponding to fluid conduits.

c) In the seal-bypass system, the fault zone is a seismically dim area compared to the protolith. As a result, stratigraphic interfaces between reservoir and seal are obscured within the fault damage zone.

d) In the presence of free CO_2 (> 4.5% SCO_2) an increased reflectivity in reflectors corresponding to reservoir-seal interfaces is observed in difference plots. These signals are visible without difference plots within the damage zone in high resolution seismic.

e) Even at low frequency seismic, mineralization causes a significant dimming effect on reflectors throughout the entire fault zone.

f) With an added overburden, most of the signals (Found in M2 and M3) related to leakage and damage zone are resolvable.

g) Adding overburden appears to amplify the effect of CO_2 content. Clear bright spots appear at the reservoir-seal interfaces, even though the velocity effect of supercritical CO_2 is less than that of a free gas cap. This effect is resolvable at conventional frequencies. Overall, adding CO_2 produces an increased impedance contrast throughout the entire section.

Chapter 6: Discussion

This seismic modelling study of the Little Grand Wash Fault (Utah, USA), with its natural CO_2 leakage system, has been tailored to explore impacts of realistic fault architecture, limitations caused by resolution, and influence of gas mobility. In the following I return to some of the key observations and relate possible implications and interpretations.

6.1 How realistic and well constrained is the tailored fault model?

The quality and reliability of the synthetic seismic images are the result of combining geological model building and seismic modelling (Alaei, 2012). The geological model building are primarily based on literature from the study area and corresponding rocks, as fieldwork was not possible to conduct (Covid-19). Therefore, not all objects assigned to the LGWF models are completely representative of the real fault zone. In addition, measurement of geophysical properties of the rocks within the study area were not performed. To compensate for this, a series of velocity estimates were made (chapter 4.3). No geological models can yield a perfect representation of nature. Still, knowledge of how the model is simplified in comparison to nature is necessary to access the models reliability to target CO_2 leakage. Therefore, how the geological model compare to nature is addressed in the following section.

The elastic properties assigned for the models in this study are only conceptual values based on literature studies. Retrieving realistic values for CO_2 exposed, faulted and deformed siliciclastic rocks are difficult without physical rock property measurements of each of the geological units. In addition, the only input of elastic properties are p-wave velocities. In reality S-wave velocities, density and elasticity also affect the propagation of seismic waves (Herron, 2011; Sheriff & Geldart, 1995). Moreover, objects that were included in the geological models were treated as homogenous features for the sake of simplification. However, in nature these rock units are internally varying both laterally and vertically in terms of elastic properties. Velocities for the deeper parts of the model are likely underestimated, as the data acquisition from Stockton & Balch (1978) are from a different geological system, exposed to different burial depths compared to the LGWF. Deeper parts of the system are generally denser due to mechanical and chemical compaction (Bjørlykke, 2015). The model is not able to account for this effect as the data sources are from different cites with different burial histories.

Stratigraphic interpretations presented (Chapter 4.2) are based on well logs from CO2W55 (Kampman, et al., 2013). Recent field data imply these interpretations to be flawed. Real seismic survey performed by (Liberty, Personal communication, 2021) display nuances within the Navajo, Carmel and Entrada formations, not captured in the models. The stratigraphic interpretations was based on the well log from (Kampman, et al., 2013) by selecting the most dominant facies variations and drawing them as

surfaces. The net signals of the stratigraphic surfaces in the real seismic produced a different seismic trace (Fig. 41 a) compared to the modelled seismic (Fig 41 c).
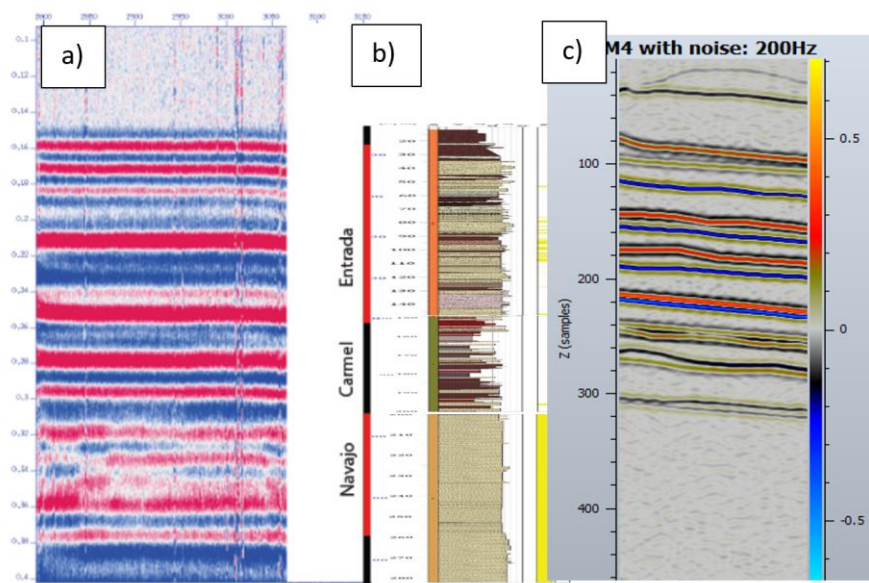
Figure 41: Comparing real versus modelled seismic data of the LGWF. a) Seismic data from (Liberty, Personal communication (2021)). Stratigraphic units are correlated to reflectors on the right hand side. b) Illustration of well log sample by (Kampman, et al., 2013) used in this study. c) Part of Model 4 in this study that correspond to the depth range of a) and b). The Synthetic trace is different from the real seismic trace, implying misinterpretation in both stratigraphy and noise level.

The structural interpretation is also simplified in this study. For the fault damage zone the modelling was limited to one mode of deformation per lithology. Fractures were assigned to tight rocks while Deformation bands where assigned to high porosity units. In reality both modes of deformation can be present within all units in a Siliciclastic damage zones (Torabi, et al., 2020). This imply that the porosity-permeability properties that the velocities and CO_2 content are based on is flawed in the geological model.

Faults zones are complex 3D structures, so interpreting them as a 2D structure is not ideal. The stratigraphic architecture, the fault facies, and ultimately the geophysical properties vary laterally, and affect the connectivity within the reservoirs (Botter, et al., 2014). Creating 2D geological models, limits the seismic modelling to 2D seismic sections unable to present an accurate distribution of the fluids and structures within the system.

In this study the system is modelled as a stable and constant leakage scenario with little variation in reservoir pore-pressure. The reality is that the LGWF is part of a complex and dynamic pressure system that respond to the pressure communication between the deep formations and geyser eruptions. There are several indices of this. Pressure gradient measurement from CO2W55 showed a formation overpressure of 1.28 Mpa (Kampman, et al., 2013) compared to the hydrostatic pressure gradient used in this study. Naturally, this also affect the brine solubility and CO_2 gas cap size, and ultimately the

seismic velocities. A seismic survey performed near Crystal Geyser (Liberty, Personal communication, 2021) detected an increased noise level prior to geyser eruption events, compared to the static noise level of this study. Noise-level and CO_2 saturation are not the only factors affected by these conditions. Studies also indicate that reservoir overpressure may increase the abundance and development of fracture corridors, further increasing fault zone permeability and altering its seismic response (Welch, et al., 2011).

6.2 Seismic modelling vs real seismic

Aside from geological models, the other part dictating the quality and reliability of the synthetic seismic are seismic modelling techniques and survey parameters. In the method presented (Chapter 4.1) the modelling process is not a perfect imitation of a real seismic survey, as some shortcuts are made. In this section, the survey parameters and the PSF based-synthetic modelling technique in comparison to real seismic is discussed.

For a survey covering reservoir depths, a frequency of 200Hz is simply not attainable as seismic waves lose too much energy with travel time. Seismic modelling also have the ability to display seismic images with perfect angle of illumination (Lecomte, et al., 2015) something that is not attainable in a real survey due to the seismic wave diffractions (Herron, 2011).

Ray-based seismic modelling does not account for seismic wave diffractions and frequency reduction with depth (Lecomte, et al., 2015). In real seismic, frequency is reduced with depth as the seismic waves lose energy to the objects and velocities increase. In the normal models (M1-M4) this effect is not present, while for M5-M6 frequencies are reduced by 50% by the time it reaches the fault zone. This is a simplification, as frequency loss is more complexed and nuanced in real surveys. (Kearey & Brooks, 1991).

Another aspect of seismic modelling is the addition of seismic noise. A real seismic noise model is of a much higher frequency than the reflected seismic data (Herron, 2011; Lecomte, et al., 2015). In addition, noise is not a constant property of a geological formation, rather it can shift depending on the pressure situation and activity in the subsurface. This is the case for the LGWF as shown by the seismic survey by (Liberty, Personal communication (2021)). A seismic emitter "thumped" the ground every 30 seconds for about 30 hours while a fixed geophone recorded the signal. This produced a trace that evolved trough time and displayed an increased amount of noise prior to Geyser eruptions (Fig. 42). The noise model in this study proved to not be as dominant as in the real seismic data.
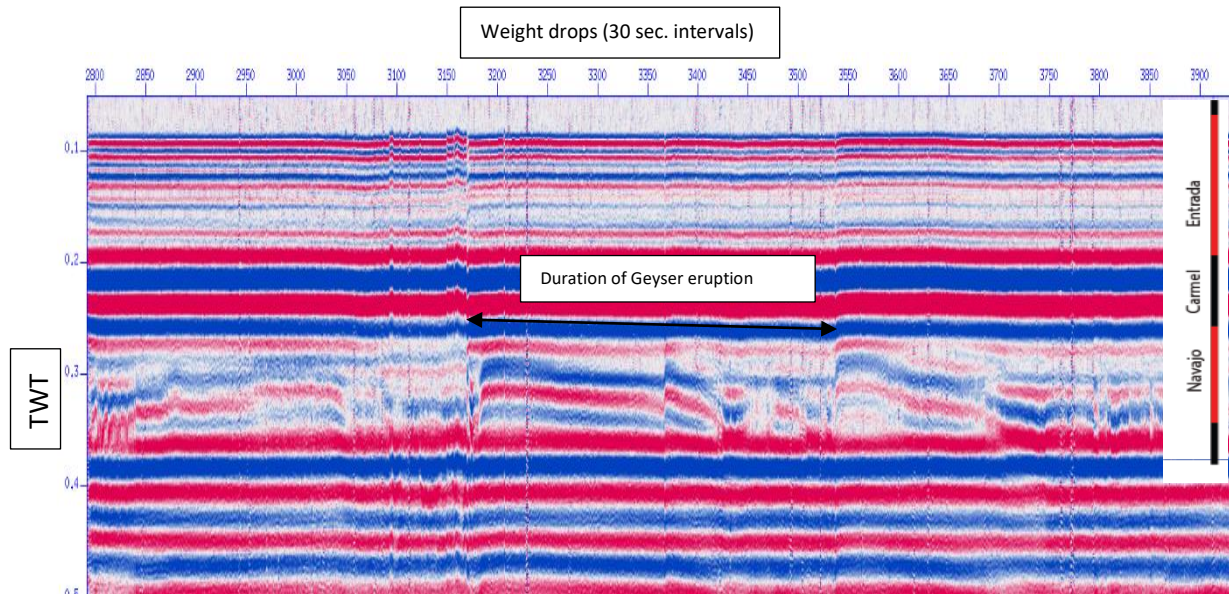
Figure 42: Seismic from the Crystal Geyser. 1 dimensional (log) sample attained from a fixed geophone and seismic emitter that has "thumped" the ground every 30 seconds for about 30 hours. This profile is a 10-hour section. These intervals define the horizontal axis. Two Way Travel-time (TWT) define the vertical axis. Geyser eruptions are expressed by a clear response in reflectivity within the reservoir followed by a build-up of seismic noise. From (Liberty, Personal communication (2021))

6.3 How is CO_2 leakage trough fault zones revealed in seismic studies?

This study target CO_2 leakage by illuminating the seismic response of three fundamental features in the models: The fault damage zone, the CO_2 plume and the mineralization following CO_2 exposure. The models design the CO_2 leakage scenario based on the interplay of these features. How these features are expressed in the modelled seismic data, and how they compare to real scenarios is discussed in the following two sections.

6.3.1 Fault architecture and fluid conduits in seismic:

The results from this study illuminate several features related to the fault zone, most importantly permeable leakage pathways in the damage zone. The results suggest that the seismic expression of a siliciclastic DZ is a dimmer area compared to the protolith, and the dimming effect increases towards to the fault core (Chapter 5.1.2). In this study, the effect can be accounted for by two properties of the fault zone: lithology and dominant mode of deformation. Reflectors associated with a sealing unit that dims toward the fault core correspond to a significant loss in velocity (-750-1200m/s) associated with fracture corridors (Boadu & Long, 1996; Botter, 2016; Ogata, et al., 2013). Similarly, porous rocks that are deformation band (DB) dominated experience a relative increase in velocity (Botter, 2016; Fredericks, et al., 2013). The exception to this are sealing units of shales, that self-seal at reservoir-pressures, increasing its velocity (Carey, et al., 2015). The CO_2 leakage scenario in this study is characterized by a zone of deformation band clusters within the porous inner DZ (W10-W5), and high

abundance of permeable fracture corridors within the sealing unit (F> 9/m). Where these zones overlap, stratigraphic interfaces within the DZ are obscured, accounting for the dimming effect of the fault zone (Fig. 43).

In the W10 zone, trough-going fractures may be not being accessible to the fluids due to the sealing DB clusters. However, the zone where trough-going fractures (statistically) occur, generally extend beyond the W10 damage zone (Childs, et al., 2009; Schueller, et al., 2013). The anisotropic nature of tight bedded rocks produces high lateral permeability (Carey, et al., 2015) allowing these fluid to leak trough a tight rock damage zone, similar to that of the LGWF. Therefore, the resulting signals from this study (Fig. 43 c) is most likely an indicator of fluid conduits at reservoir-seal interfaces in siliciclastic fault zones.
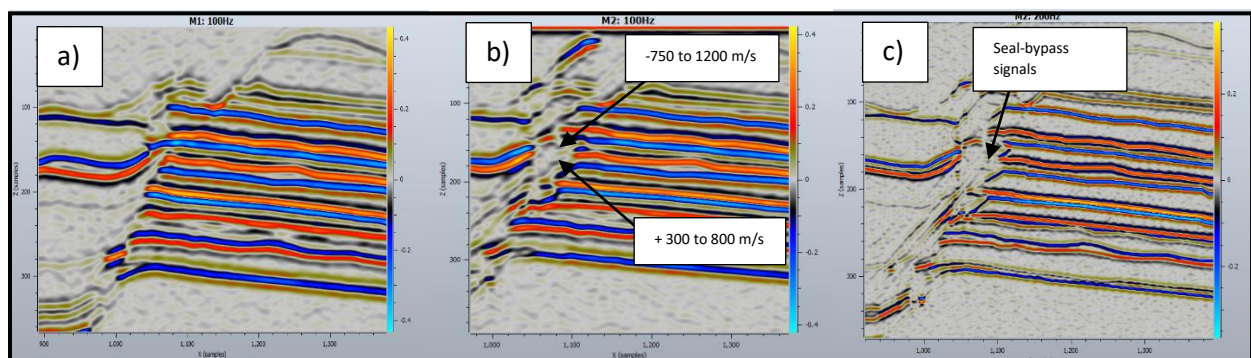
Figure 43: The fault damage zone is characterized by a seismically dim area, accounted for by high abundance of shear/compaction deformation bands and high fracture counts a) Synthetic seismic of model 1 – no damage zone b) Synthetic image of Model 2 – with damage zone. The velocity input that correlate with the seismic response of the DZ are illustrated c) Synthetic image of Model 2 – at 200Hz. Obscured stratigraphic interfaces in the DZ are associated to fluid-conduits in high resolution seismic.

The seismic modelling performed in this study are comparable to several seismic examples of offshore seismic data for subsurface damage zones. The best example are from seismic data of the Norwegian continental shelf (Fig. 44) (Alaei & Torabi, 2017).
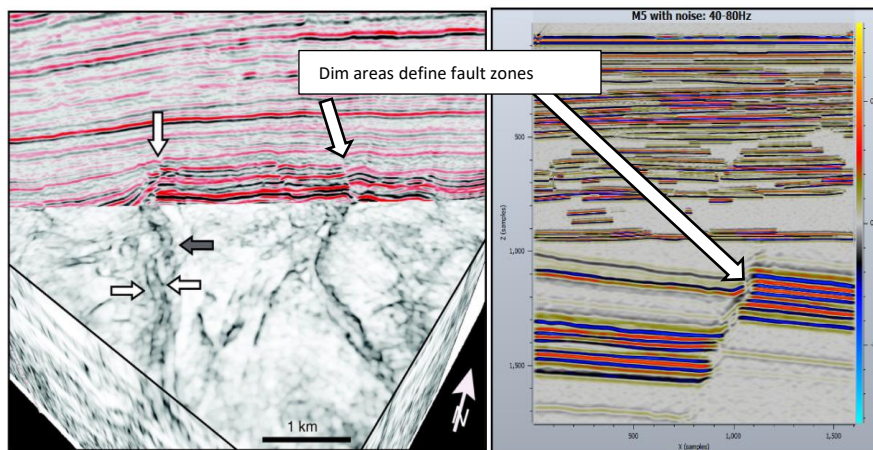
Figure 44: Fault damaged zone visualized in seismic. a) The data display normal faults in siliciclastic rocks on the Norwegian Continental Shelf. A coherence attribute volume displays fault zones in a time slice. In this seismic fault zones are distinguishable from the surrounding strata. The scale of the data is much larger than the modelled synthetic seismic, but still the fault is resolved as a white, dim line corresponding to the damage zone, similar to the results in this study. Modified from Fig. 5 in (Alaei & Torabi, 2017). b) The fault damage zone in M5 display a similar signal as in a).

6.3.2 CO$_2$ in seismic

The results suggest that the seismic expression of an upward migrating CO$_2$ plume increase the impedance contrast between porous and tight rocks, though these signals are initially vague and are primarily detected in difference plots (Chapter 5.2). For the overburden case, illumination of the supercritical CO$_2$ plume displayed a clearer versions of the same signals, and was visible even at conventional seismic parameters (40Hz). Signals of leakage within fault zones is the combined expression of the plume and the DZ. Since the DZ is a seismically dimmer area, a clearer contrast is observed in the DZ compared to the protolith (Chapter 5.2), though the signal is challenging to target under conventional seismic parameters, as the fault DZ objects are on the scale of 5-20 meters. Using parameters equivalent to p-cable frequencies (>100Hz) and illumination angle of > 45° is therefore ideal for illuminating CO$_2$ in fluid conduits, indicating that fluid migration may be challenging to target in using conventional seismic data.

The signals can be accounted for by the relative loss in seismic velocity of a porous media containing CO$_2$ (described in (Agofack, et al., 2018) in contact with tight rock containing little to no CO$_2$. The velocity decrease is assigned to the Slick Rock Member and the inner DZ of the Earthy Facies (see chapter 4.3.3) as authors observed past traces of CO$_2$ migration and degassing in these units (Fig. 44) (Ogata, et al., 2013; Skurtveit, et al., 2020; Torabi, et al., 2013). Overall, this yielded an increased discrepancy in velocity at the Reservoir – Seal interfaces (Slick rock mbr - Earthy Facies) (Fig. 45)
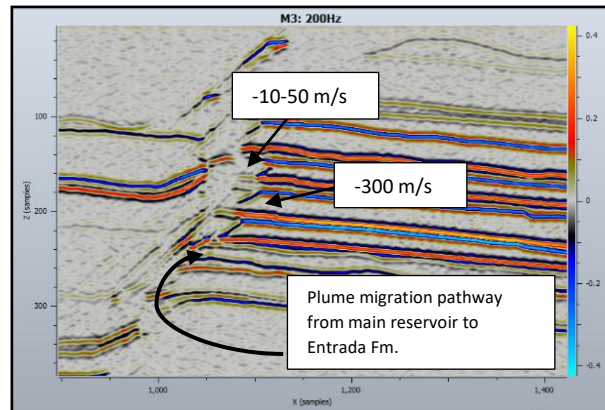
Figure 45: Synthetic image of Model 3. How velocity effects of the CO₂ plume account for the increased impedance contrasts in the Entrada Formation and within the initially dim damage zone is illustrated. A hypothetical plume migration pathway trough the Carmel inner fractured DZ is illustrated.

The synthetic seismic signals corresponding to the CO_2 plume in the Entrada Formation can be compared to studies that present seismic expressions of supercritical CO_2 in a confined reservoir (Furre, et al., 2017; Shi, et al., 2013). The increased reservoir-seal contrast is similar to the response of the supercritical plume surveyed in the Sleipner field on the Norwegian Horda-platform (Furre, et al., 2017) (Fig. 46).
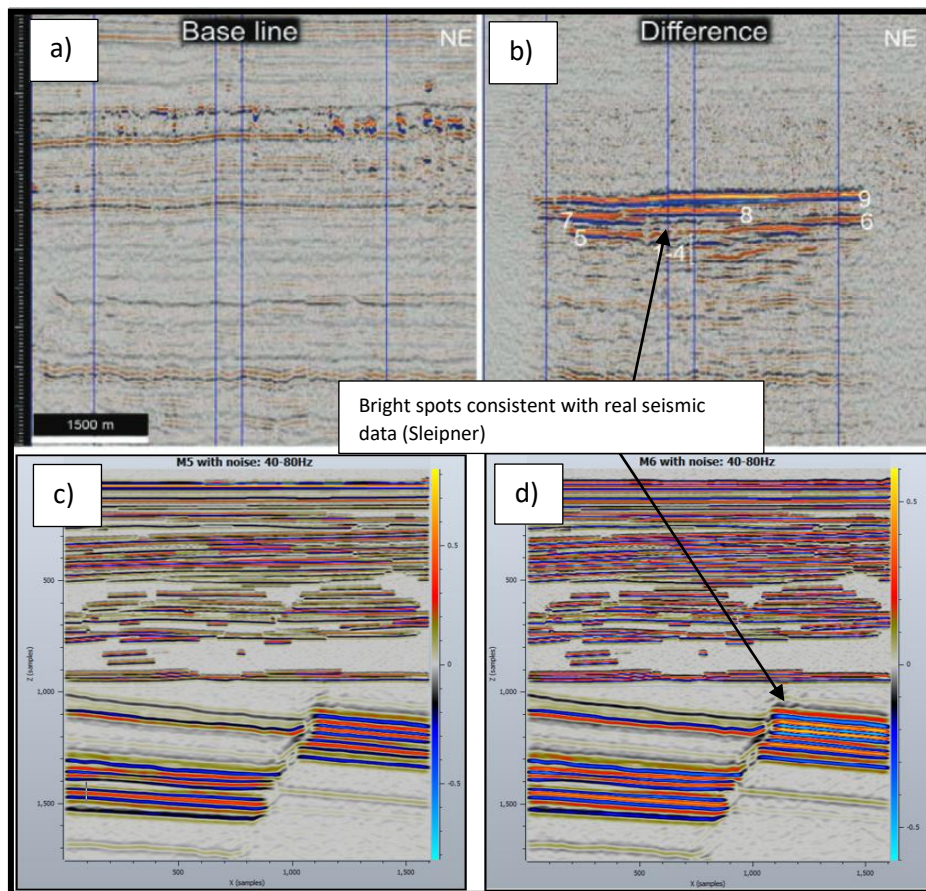
Figure 46 a) Seismic survey of the Sleipner storage cite, prior to CO₂ storage. b) After CO₂ storage. Similar impedance contrasts in the presence of CO₂ and at a much larger scale than the LGWF. Modified from fig. 2 in (Furre, et al., 2017). C) M5 close up of fault zone prior to CO₂ storage d) M6 Close up of fault zone illustrating bright spots, after After CO₂ storage.

The results suggest that the seismic expression of calcite deposits from prolonged CO_2 – rock interactions, is characterized by a dimming effect throughout the model. Calcite precipitation also appear to further dim the fault damage zone. Although the velocity data imply a net velocity decrease (see table 7, chapter 4.3.4), and the 5% added noise may dim the entire image (as discussed in Chapter 5.1.1) model inputs could not confidently account for these effects. The velocity increase within the high porosity units described by (Tsujia, et al., 2019) was expected to decrease the overall impedence contrast within FW, and increase the contrast between FW and HW, but the effect is not confined to these objects. The velocity recovery of the fractured DZ described in (Aben, et al., 2017) was expected to enhance stratigraphic interfaces within the DZ, but the opposite effect is observed. Overall, the results illuminating calcite precipitation are inconclusive, as the response could not confidently be accounted for by model inputs. Still, the results imply that if degassing of CO_2 charged brine takes place and precipitate carbonate minerals, some expression in seismic data is expected.

6. 4 Global significances: Seismic modelling of CO_2 leakage in the LGWF

Seismic modelling of onshore analogues, even with limited input of seismic data, has helped solve offshore interpretation issues in the past (Anell, et al., 2016). The model(s) utilized in this study are relatively simple compared to the actual geology of the LGWF (See section 6.1). Still, some aspects of fluid leakage could confidently be interpreted, even at conventional seismic frequencies. It is therefore reasonable to suggest that seismic modelling of the LGWF may aid seismic interpretations of CO_2 migration and fault sealing capabilities in the subsurface. To what degree this study is applicable to other storage prospects on a global scale, and how it may be used to solve interpretative problems in the future, is discussed in the following section.

The technical feasibility of CCS has been successfully demonstrated in offshore Norway both in the North Sea Sleipner project (Furre, et al., 2017) and in the Barents Sea Snøhvit project (Eiken, et al., 2011; Shi, et al., 2013; Tasianas, et al., 2015). Other prospects worth mentioning are the Smeaheia fault block Alpha prospect (Mulrooney, et al., 2020) and the Fri I and II prospects in the Northern Gulf coast (Meckel, et al., 2021). These sites are at depths of more than 800 meters storing CO_2 in supercritical conditions, and can mainly be studied trough seismic data. All of the systems hold several challenges in interpreting the storage and sealing capacity of the geology related to seismic resolution. Similar issues are likely to be encountered in future storage sites as well.

To make CCS economically feasible, storage cite sealing capabilities should ideally be evaluated prior to storage (Benson, et al., 2005). The applicability of the results to predicting leakage scenarios in seismic data, are illumination of fluid conduits in the fault DZ. These results could potentially be useful when evaluating storage prospects (that are similar to LGWF in lithology and fault offset) using p-cable technologies. Given our limited experience with CCS, monitoring of stored CO_2 in geological formations are also critical (Benson, et al., 2005). This study interprets plume signals in stratigraphic units, at conventional frequencies, that may be valuable for detection of early leakage. The synthetic images imply that a plume migrating from a storage reservoir can be resolved when situated at porous - tight rock interfaces in the overburden.

CO_2 leakage scenarios have been modelled in the form of gas chimneys in the reservoir overburden (uppermost 800 m) for the Snøhvit prospects in the Barents Sea (Tasianas, et al., 2015). In the modelled scenario, degassing and mineralization was expected to occur. An important aspect of modelling which was not possible to cover was quantifying the hydraulic properties of seal by-passing fluid conduits. It was argued that studying field analogues, using multi-frequency acoustic surveys and drilling into gas filled/mineralized strata could improve the model. The LGWF contains both well log data of the gas filled-CO_2 altered units (Kampman, et al., 2013), and seismic data displaying leakage (Liberty, Personal communication, 2021). Synthetic seismic images of mineralization could provide valuable input for both this and other models where degassing and mineralization would take place. Seismic modelling performed in this study estimate how CO_2 altered rocks appear in seismic, though the accounting for the results were difficult. The resulting images of Model 4 (Chapter 5.2.2) might still be useful when interpreting seismic surveys where gas chimneys or leakage from shallow fault zones (<800m depth) occur.

Storage of CO_2 will primarily be performed at depths >800 meters. Mineralization will not be similar to that in the LGWF as degassing will not occur until the uppermost 800 meters. The process of mineralization from degassing is estimated to take months or more depending on the saturation and host rock mineralogy (Aben, et al., 2017; Pentecost, 2005; Tsujia, et al., 2019). Relying on this signal alone to detect leakage is not ideal. At this point, a well is drilled, large amounts of CO_2 may already have been sequestered, and the economic loss may be substantial. The findings of this study also imply that degassing itself is challenging to detect without high-frequency p-cable seismic.

Chapter 7: Conclusions and further work

7.1 Concluding remarks

The results of the geophysical parameter sensitivity study revealed that the dominant frequency and the level of noise have a significant impact when illuminating the stratigraphic architecture and CO_2 plume in seismic images. The illumination angle and frequency are the parameters with the greatest impact on the fault zone resolution.

The modelling performed allowed for interpretation of some key aspects of CO_2 leakage in seismic data. The following signals are the main findings of this study:

I)   Increased reflectivity is seen at the reservoir-seal interfaces in the presence of a CO_2 plume. This response is resolvable in conventional seismic data (40Hz frequency) at reservoir depths. The expression is detectable at the shallow scenario for all frequencies and is resolvable at high frequencies.

II)   Fluid conduits are associated with obscured stratigraphic interfaces between tight and porous rocks in the fault damage zone. This is due to the velocity increase of porous rocks due to deformation band clusters, and the relative velocity decrease in fractured tight rocks. Overall the damage zone is a seismically dim area. These initially dim areas display increased impedance contrast when filled with CO_2. The confidence of these interpretations generally increase with seismic resolution, and apply for both deep and shallow storage scenarios.

III)   Results suggest that prolonged exposure of siliciclastic rocks to CO_2 impacts the seismic images. A dimming effect is seen throughout the entire model, but cannot be fully accounted for by model velocity-input. Literature imply that such a response may be resolvable after a period of only a few months.

Evaluation of potential fluid conduits prior to storage, and detecting any leakage as early as possible is needed to make CCS economically feasible. Resolving fluid conduits on the scale of 5-20 meters in the fault zone will likely be required to make these evaluations. In this study, fluid conduits could only confidently be interpreted at ideal values of geophysical survey parameters, such as dominant frequencies of >100 Hz and angle of maximum illumination between 45° and 90°.

67

Based on this and other studies of seismic modelling, i argue that synthetic seismic modelling of CO_2 leakage likely has the potential to aid monitoring and verification of geologically stored CO_2, as well as evaluation of fault sealing capabilities in future storage sites.

7.2 Future work:

This model has several limitations related to the fault zone and CO_2 plume (see Chapter 6.1), and illmunation of fluid conduits require high-resolution seismic data. A more detailed, 3D model may be able to illuminate more aspects of fluid conduits and CO_2 leakage in conventional seismic data. If the goals is to predict fluid-conduits prior to storage, there is room for an improved model of CO_2 migration in the LGWF with more nuanced fault facies and lateral variations in stratigraphic architecture.

Fluid leakage and mineralization in fault zones trough different lithologies than that of the LGWF (i.e carbonates and marine shales) may look very different in seismic data. Further seismic modelling of CO_2 migration in fault zones trough different lithologies may increase our general understanding of the behavior and seismic signals of CO_2 in the subsurface.

References

Aben, F. M., Doan, M.-L., Gratier, J. & Renard, F., 2017. Experimental postseismic recovery of fractured rocks assisted by calcite sealing. *geophysical research letters,* Volume 44, pp. 7228-7238.

Agofack, N., Lozovyi, S. & Bauer, A., 2018. Effect of CO2 on P- and S-wave velocities at seismic and ultrasonic frequencies. *International Journal of Greenhouse Gas Control ,* Volume 78, pp. 388-399.

Alaei, B., 2012. Seismic modeling of complex geological structures:. *Seismic waves -Research and Analysis,* Volume 11, p. 213–236.

Alaei, B. & Torabi, A., 2017. Seismic imaging of fault damaged zone and its scaling relation with displacement. *interpretation,* 5(4).

Andersen, I. G., 2020. *Effects of geophysical parameters on the seismic expression of the Maghlaq Fault, Malta: insights from outcrop-based 2D seismic modeling.* [Online]
Available at: https://bora.uib.no/bora-xmlui/handle/1956/22991?show=full
[Accessed 5 Febuary 2021].

Anderson, O. & Lucas, S., 1994. Middle Jurassic stratigraphy, sedimentation and paleogeography in the southern Colorado Plateau and southern High Plains, in Caputo, M.V., Peterson, J.A., and Franczyk, K.J., eds.,. *Mesozoic Systems of the Rocky Mountain Region, USA: SEPM, Rocky Mountain section,* pp. 299-314.

Anell, I., Lecomte, I., Braathen, A. & Buckley, S., 2016. Synthetic seismic illumination of small-scale growth faults, paralic deposits and low-angle clinoforms: A case study of Triassic successions on Edgeøya, NW Barents Shelf:. *Marine and Petroleum Geology,,* Volume 77, p. 625–639.

Averitt, P. et al., 1955. evisions in correlation and nomenclature of Triassic and Jurassic formations in southwestern Utah and northern Arizona. *American Association of Petroleum Geologists, bulletin,* 39(12), pp. 2515-2524.

Aydin, I., B. R. & P, I., 2006. Geological and mathematical framework for failure modes in granular rock. *Journal of Structural Geology,* Volume 28, pp. 83-98.

Baer, J. & Rigby, J., 1978. Geology of the Crystal Geyser and environmental implications of its effluent, Grand County, Utah. *Utah Geology*, pp. 5-6.

Bates, R. & Jackson, J., 1984. *American Geological institute: Dictionary of geological terms.* 3 ed. s.l.:Dolphin reference book, 360..

Beach, A., Welbon, A., Brockbank, P. & McCallum, J., 1999. Reservoir damage around faults: outcrop examples from the Suez rift.. *Petroleum Geoscience ,* Volume 5, pp. 109-116.

Benson, et al., 2005. *Underground Geological Storage. IPCC Special Report on Carbon Dioxide Capture and Storage,* Cambridge, UK: Cambridge University Press.

Berg, S. S. & Skar, T., 2005. Controls on damage zone asymmetry of a normal fault zone: outcrop analyses of a segment of the Moab fault, SE Utah. *Journal of Structural Geology ,* Volume 27, p. 1803–1822.

Bjerrum, C., Dorsey, R. & Becker, U., 1993. Onset of foreland-basin subsidence in the Middle Jurassic Utah-Idaho Trough, E Nevada and W Utah. *Geological Society America Abstr. with Progr.,* Volume 25, p. 10.

Bjerrum & Dorsey, 1995. Tectonic controls on deposition of Middle Jurassic strata in a retroarc foreland basin, Utah-Idaho trough, western interior, United States.. *Tectonics (Washington, D.C.),* Volume 14, pp. 962-978.

Bjørlykke, 2015. Compaction of sedimentary rocks: Shales, sandstones and carbonates.. In: *Petroleum geoscience: From sedimentary enviorments to rock.* s.l.:s.n., pp. 816-817.

Blakey, R., 2014. Paleogeography and Paleotectonics of the Western Interior Seaway, Jurassic-Cretaceous of North America. *AAPG Search and Discovery Article* , pp. 1-72.

Blakey, R. C. & Ranney, W., 2018. The Continental Arc, Sevier Orogeny, Western Interior Seaway and Flat-Slab Subduction: Cretaceous Period: Ca. 145–65 Ma. In: *Ancient Landscapes of Western North America.* s.l.:s.n., pp. 103-130.

Blakey, R., Havholm, K. & Jones, L., 1996. Stratigraphic Analysis of eolian interactions with marine and fluvial deposts (middle jurassic page sandstone and carmel formations, colorado plateau, USA. *Journal of sedimentary research ,* Volume 66, pp. 324-342.

Boadu, F., 1997. Fractured rock mass characterization parameters and seismic properties: Analytical studies. *Journal of Applied Geophysics,* Volume 37, pp. 1-19.

Boadu, F. K. & Long, L. T., 1996. Effects of fractures on seismic-wave velocity and attenuation. *Geophys. J. Int. ,* Volume 127, pp. 86-110.

Bond, C., 2015. Uncertainty in structural interpretation: Lessons to be learnt. *Journal of Structural Geology,* Volume 74, pp. 185-200.

Botter, C. D., 2016. *Seismic Imaging of Fault Zones: A synthetic workflow to study the impact of faults on.* Stavanger, NO: University of Stavanger: Faculty of Science and Technology, Department of Petroleum Engineering .

Botter, C., N. C., Hardy, S. & Isabelle Lecomte, 2014. From mechanical modeling to seismic imaging of faults: A synthetic workflow to study the impact of faults on seismic. *Marine and Petroleum Geology ,* Volume 57, pp. 187-207.

Braathen, A. & Liberty, L., 2020 Personal communication. recent, un-published field work in the Crystal Geyser.

Braathen, A. et al., 2020. Interaction of deformation bands and fractures during progressive strain in monocline - San Rafael Swell, Central Utah, USA. *Journal of Structural Geology,* Volume 141.

Braathen, A. et al., 2009. Fault facies and its application to sandstone reservoirs. *AAPG Bulletin,* 93(7), p. 891–917.

Brekke, H., Sjulstad, H. I., Magnus, C. & Williams, R. W., 2001. Sedimentary environments offshore Norway--- an overview. *NPF Special Publication,* pp. 7-37.

Brenner, R. & Peterson, J., 1994. Jurassic sedimentary history of the northern portion of the Western Interior Seaway, USA, in Caputo, M.V., Mesozoic systems of the rocky mountain region, USA. *SEPM, Rocky Mountain section,* pp. 233-272.

Burchfiel, B. & Davis, G. A., 1972. Structural framework and evolution of the southern part of the Cordilleran Orogen western United States,. *Am. J. Sci.,* Volume 272, pp. 97-118.

Burnside, N. M., Shipton, Z. K., Dockrill, B. & Ellam, R. M., 2013. Man-made versus natural CO_2 leakage: A 400 k.y. history of an analogue for engineered geological storage of CO_2. *GEOLOGY,* Volume 41, p. 471–474.

Campbell, A. & Baer, L., 1978. Little Grand Wash Fault–Crystal Geyser Area (CO_2 Gas). In: *Oil and gas fields of the four corners area.* s.l.:Four Corners Geological Society, pp. 666-669.

Carey, W. et al., 2015. Fracture-permeability behavior of shale. *Journal of Unconventional Oil and Gas Resources,* Volume 11, pp. 27-43.

Chadwick, R., Noy, D., Arts, R. & Eiken, O., 2009. Latest time-lapse seismic data from Sleipner yield new insights into CO_2 plume development.. *Energy procedia,* Volume 1, pp. 2103-2110.

Chen, D., Pan, Z. & Ye, Z., 2015. Dependence of gas shale fracture permeability on effective stress and reservoir pressure: Model match and insights. *Fuel,* Volume 139, pp. 383-392.

Childs, C. et al., 2009. A geometric model of fault zone and fault rock thickness variations. *Struct. Geol.,* Volume 31, pp. 117-127.

Claine, J., Evans, J. & Forster, C., 1996. Fault zone architecture and permeability structure. *geology,* Volume 24, pp. 1025-1028.

Clemmensen, L., Olsen, H. & Blakey, R., 1989. Erg-margin deposits in the Lower Jurassic Moenave Formation and Wingate Sandstone, southern Utah. *Geological Society of America bulletin,* 101(6), pp. 759-773.

Coulomb, C. A., 1776. Essai sur une application des regles des maximis et minimis a quelquels problemesde statique relatifs, a la architecture. *Mem. Acad. Roy. Div. Sav,* Volume 7, p. 343–387.

Crabaugh & Kocurek, 1993. Entrada Sandstone: An example of a wet aeolian system.. *The Dynamics and Environmental Context of Aeolian Sedimentary Systems. Geological Society Special Publication ,* Volume 72 , pp. 103-112.

Crabaugh & Kocurek, 1998. Continental sequence stratigraphy of a wet eolian system -- A key to relative sea level change. *SEPM Spec. Publ.,* Volume 59.

Crider, J. & Peacock, D., 2004. Initiation of brittle faults in the upper crust: A review of field observations. *Journal of structural geology,* Volume 26, pp. 691-707.

Currie, B., 1998.. Upper Jurassic Lower Cretaceous Morrison and Cedar Mountain Formations, NE Utahe-NW Colorado: relationships betweennonmarine deposition and early Cordilleran foreland-basin development. *.Journal of Sedimentary Research,* Volume 68, pp. 632-652.

DeCelles, P., Lawton, T. & Mitra, G., 1995. timing, growth of structural culminations, and synorogenic sedimentation in the type Sevier orogenic belt, western united states. *geology,* Volume 23, pp. 699-702.

Desimone, J. M. & Tumas, W., 2003. *Green Chemistry Using liquid and supercritical carbon dioxide.* 1 ed. s.l.:Oxford University Press, USA.

Dockrill, B. & Shipton, Z. K., 2010. Structural controls on leakage from a natural CO_2 geologic storage site: Central Utah, U.S.A. *Journal of Structural Geology 32 ,* p. 1768–1782.

71

Doelling, H., 2002. *Interim Geologic Map of the San Rafael Desert 30' x 60' Quadrangle, Emery and Grand Counties, Utah,* s.l.: (Open-file Report 404). Utah Geological Survey, p.21.

Duan, Z. & Sun, R., 2003. An improved model calculating CO_2 solubility in pure water and aqueous NaCl solutions from 273 to 533 K and 0 to 2000 bar. *Chemical geology,* Volume 193, pp. 257-271.

Dumitru, Duddy & Green, 1994. Mesozoic-Cenozoic burial, uplift, and erosion history of the west-central Colorado Plateau. *GEOLOGY,* Volume 22, pp. 499-502.

Eichhubl, P., Davatzes, N. & Becker, S., 2009. Structural and Diagenetic Control of Fluid Migration and Cementation Along the Moab Fault, Utah. *AAPG Bulletin,* Volume 93, p. 653–681.

Eiken, et al., 2011. Lessons learned from 14 years of CCS operations: Sleipner, IN Salah and Snohvit.. *Energy Proced,* Volume 4, p. 5541–5548.

Faleide, T. S. et al., In review. Impacts of seismic resolution on fault interpretations: Insights from seismic modelling. *Faleide et al. – fault mapping in seismics* .

Fan, M. & Carrapa, B., 2014. Late Cretaceous–early Eocene Laramide uplift, exhumation, and basin subsidence in Wyoming: Crustal responses to flat slab subduction. *Tectonics,* 33(4), pp. 347-595.

Fenneman, N. M., 1917. *Physiographic Subdivision in the United States.* s.l., Proceedings of the National Academy of Sciences of the United States 3, 17-22.

Fossen, H., Schultz, R., Shipton, Z. & Mair, K., 2007.. Deformation bands in sandstone: a review.. *Journal of the Geological Society, London ,* Volume 164, pp. 755-769.

Fredericks, K., Goodwin, L. & Tobin, H., 2013. *Petrophysical Properties of a Deformation Band Fault Zones in the Entrada Sandstone, Utah,* Pittsburgh, Pennsylvania: Search and Discovery Article #5086.

Fredman, N. et al., 2007. Sensitivity of fluid flow to fault core architecture and petrophysical properties of fault rocks in siliciclastic reservoirs: A synthetic fault model study:. *Petroleum Geoscience,* Volume 13, p. 305–320..

Fredman, et al., 2008. Fault facies modeling: Technique and approach for 3-D conditioning and modelling of faulted grids,. *AAPG bulletin,* Volume 92, pp. 1457-1478.

Frery, E. et al., 2015. Evolution of fault permeability during episodic fluid circulation: Evidence for the effects of fluid–rock interactions from travertine studies Utah, USA. *Tectonophysics,* Volume 651–652, pp. 121-137.

Furre, et al., 2017. 20 years of monitoring CO_2-injection at Sleipner. *Energy Procedia,* Volume 114, p. 3916–3926..

Gardner, G. H. F., Gardner, L. W. & Gregory, A. R., 1974. FORMATION VELOCITY AND DENSITY-THE DIAGNOSTIC BASICS FOR STRATIGRAPHIC TRAPS. *GEOPHYSICS,* Volume 39, pp. 770-780.

Garrison, J. et al., 2007. A multidisciplinary study of the Lower Cretaceous Cedar Mountain Formation, Mussentuchit Wash, Utah: a determination of the paleoenvironment and paleoecology of the Eolambia caroljonesa dinosaur quarry. *Cretaceous Research ,* Volume 28, pp. 461-494.

Gouveia, F., Johnson, M., Leif, R. & Friedmann, J., 2005. Aerometric measurement and modeling of the mass of CO_2 emissions from Crystal Geyser. *). Lawrence Livermore National Laboratory*, p. 57.

Gratier, J.-P., Frery, E., Deschamps, P. & Røyne, A., 2012. How travertine veins grow from top to bottom and lift the rocks above them: The effect of crystallization force. *Geology 40*, pp. 1015-1018.

Greentown, 36-24H, 2009. *Delta Petroleum Corporation: Well Completion or Recompletion Report and Log for Greentown State 36-24H (API: 4301931519)..* s.l.:Utah Department of Natural Resources – Division of Oil, Gas and Mining..

Gutierrezab, M., Katsukia, D. & AzraTutuncua, 2015. Determination of the continuous stress-dependent permeability, compressibility and poroelasticity of shale. *Marine and Petroleum Geology,* Volume 68, pp. 614-628.

Han, K. et al., 2015. Revealing fate of CO2 leakage pathways in the Little Grand Wash Fault, Green River, Utah. *American Geophysical Union, Fall Meeting 2015*.

Harper, K. T., Clair, L. L. S., Thorne, K. & Hess, W. M., 1994. *Natural History of Colorado Plateau and Great Basin.* 1 ed. s.l.:American Library Association CHOICE.

Heath, J., 2004. *Hydrogeochemical Characterization of Leaking Carbon Dioxide-Charged Fault Zones in East-Central Utah,.* s.l.:Master Thesis, Utah State university, USA.

Helffrich, G. R. & Wood, B. J., 2001. . "The Earth's mantle". *Nature,* Volume 412, p. 501–7.

Herron, D., 2011. *First Steps in Seismic Interpretation.* R. B. Latimer, Ed ed. Tulsa, Oklahoma: Society of Exploration Geophysicists.

Huffman, W. et al., 1996. The Field Geology of the Moab Fault. *Geology and Resources of the Paradox Basin: Utah Geological Association Guidebook 25.*

Hunter, R., 1981. *Stratification styles in eolian sandstones: some Pennsylvanian to Jurassic examples from the western interior USA..* s.l.:SEPM.

Jamison, W. & Stearns, D., 1982. Tectonic deformation of Wingate Sandstone, colorado national monument. *AAPG Bulletin,* Volume 66, p. 2584–2608..

Jarrard, R. et al., 2003. physical prop-erties of upper oceanic crust: ocean Drilling Program Hole 801C and the waning ofhydrothermal circulation.. *J. Geophys. Res. 108,* Volume 108, p. 2188..

Jung, N.-H.et al., 2014. Fault-controlled CO2 leakage from natural reservoirs in the Colorado Plateau, East-Central Utah. *Earth and Planetary Science Letters,* Volume 403, pp. 358-367.

Kampman, et al., 2013. *Scientific drilling and downhole fluid sampling of a natural CO2 reservoir, Green River, Utah,* Cambridge, UK: Copernicus Publications on behalf of the IODP and the ICDP..

Kassaba, M. A. & Weller, A., 2015. Study on P-wave and S-wave velocity in dry and wet sandstones of Tushka region, Egypt. *Egyptian Journal of Petroleum,* Volume 24, pp. 1-11.

Kearey, P. & Brooks, M., 1991. *An introduction to geophysical exploration.* 2 ed. Malden, Massachusetts: Blackwell Science.

Kim, Y., Peacock, D. & Sanderson, D., 2004. Diffraction imaging by focusingdefocusing: An outlook on seismic superresolution:. *Geophysics,* Volume 69, p. 1478–1490.

Kirkland, J. I., Suarez, M., Suarez, C. & Hunt-Foster, R., 2016. The Lower Cretaceous in east-central Utah—The Cedar Mountain Formation and its bounding strata. *Geology of the Intermountain West ,* Volume Vol. 3 , pp. 101-228.

Kocurek, G. & Dott, R. H., 1981. Distinctions and uses of stratification types in the interpretation of eolian sand. *journal of sedimentary research,* Volume 51.

Krylova, A., 2016. *A seismic model of fractured shale.* Houston: university of Houston texas.

Lebedeva-Ivanova, N. et al., 2018. Toward one-meter resolution in 3D seismic.. *Lead. Edge ,* Volume 37, p. 818–828. .

Lebedev, M., Iglauer, S. & Mikhaltsevich, V., 2014. Acoustic response of reservoir sandstones during injection of supercritical CO2. *Energy Procedia ,* Volume 63, p. 4281 – 4288 .

Lecomte, I., 2008. Resolution and illumination analyses in PSDM: A ray-based approach: The. *The Leading Edge,* Volume 27, , p. 650–663.

Lecomte, I. et al., 2015. Ray-based seismic modeling of geologic models: Understanding and analyzing seismic images efficiently:. *Interpretation,* Volume 3, p. 71–89.

Lecomte, I. et al., 2016. 2(3)D convolution modelling of complex geological targets beyond – 1D convolution:. *First Break,* Volume 34, p. 99–107..

Liberty, L., Personal communication (2021). Seismic survey of the LGWF.

Lindsey, J., 1989. The Fresnel zone and its interpetive significance:. *the Leading Edge,,* Volume 8, p. 33–39.

Livaccari, R., 1991. Livaccari, R.F., 1991. Role of crustal thickening and extensional collapse in the tectonic evolution of the Sevier-Laramide orogeny, western United States. *Geology,* Volume 19, p. 1104–1107.

Li, Z. & Schieber, J., 2017. Detailed facies analysis of the Upper Cretaceous Tununk Shale Member,Henry Mountains Region, Utah: Implications for mudstone depositionalmodels in epicontinental seas. *Sedimentary Geology*, 22 december, pp. 141-159.

Li, Z. & Schieber, J., 2018. COMPOSITE PARTICLES IN MUDSTONES: EXAMPLES FROM THE LATE CRETACEOUS TUNUNK SHALE MEMBER OF THE MANCOS SHALE FORMATION. *Journal of Sedimentary Research,* Volume 88, p. 1319–1344.

Maidment, S. & Muxworthy, A., 2019. A CHRONOSTRATIGRAPHIC FRAMEWORK FOR THE UPPER JURASSIC MORRISON FORMATION, WESTERN U.S.A. *Journal of Sedimentary Research, 2019,* Volume 89, p. 1017–1038.

Major, J., Eichhubl, P. D. T. & Jon, O., 2017. Effect of CO2–brine–rock interaction on fracture mechanical properties of CO2 reservoirs and seals. *Earth and Planetary Science Letters,* Volume 499, pp. 37-47.

Manzocchi, T., Walsh, J., Nell, P. & Yielding, G., 1999. Fault transmissibility multipliersforflow simulation models.. *Petrol. Geosci.,* Volume 5, p. 53–63.

Marzolf, J. E., 1993. Palinspastic reconstruction of early Mesozoic sedimentary basins near the latitude of Las Vegas: Implications for the early Mesozoic Cordilleran cratonal mar-gin, in Mesozoic Paleogeography of the western United States-II. *Mesozoic Paleogeography of the western United States-II,* Volume 71, pp. 433- 462.

Meckel, T. et al., 2021. Carbon capture, utilization, and storage hub development on the Gulf Coast. *Greenhouse Gases: Science and Technology; DOI: 10.1002/ghg.2082,* pp. 0-14.

Middleton, M., 1989. A model for the formation of intracratonic sag basins. *. Geophys. J. ,* Volume 99, pp. 665-676..

74

Mondol, N. H., Jahren, J. & Bjørklykke, K., 2008. *Elastic properties of clay minerals.* Trondheim: StatoilHydro.

Mulrooney, M. J. et al., 2020. Structural analysis of the Smeaheia fault block, a potential CO2 storage site, northern Horda Platform, North Sea. *Marine and Petroleum Geology,* Volume 121.

Nelson, S. T. et al., 2008. *Enhanced fracture permeability and accompanying fl uid fl ow in the footwall of a normal fault: The Hurricane fault at Pah Tempe hot springs, Washington County, Utah,* Bulletin: Geological Society of America.

Newell, A. J. & Butcher, A. S., 2015. *Sedimentological control on the reservoir and caprock properties of a bleached palaeoreservoir in the Entrada Formation at Salt Wash Graben, Green River, Utah,* Keyworth, Nottingham : Environmental Modelling Programme: British Geological Survey.

Nuccio, V. & Condon, S., 1996. *Burial and Thermal History of the Paradox Basin, Utah and Colorado, and Petroleum Potential of the Middle Pennsylvanian Paradox Formation,* Denver, CO: Utah Geological Association.

Ogata, K., Senger, K., Braathen, A. & Tveranger, J., 2013. Fracture corridors as seal bypass system in siliciclastic reservoir-cap rock successions: Field-based insights from the jurassic entrada formation (SE Utah, USA). *Journal of structural geology,* Volume 66, pp. 162-187.

Pentecost, A., 2005. *Travertine:,* Berlin, Heidelberg: Springer, 453 p..

Petersen, C. et al., 2010. High-resolution P Cable 3D seismic imaging of gas chimney structures in gas hydrated sediments of an Arctic sediment drift:. *Marine and Petroleum Geology,* Volume 27, p. 1981–1994.

Peterson, F. & Turner-Peterson, C., 1989. *Geology of the Colorado plateau.* Denver, Colorado: American Geophysical Union, Washington, D.C.

Petrie, E. S., Evans, J. P. & Bauer, S. J., 2014. *Failure of cap-rock seals as determined from mechanical stratigraphy, stress history, and tensile-failure analysis of exhumed analogs,* s.l.: The American Association of Petroleum Geologists.

Pijnenburg, R. et al., 2015. *Determination of effects of CO2 on clay-bearing caprock and reservoir analogues from the Green River borehole CO2W55,* Rijswijk: Shell Global Solutions International.

Planke, S. et al., 2009. P-Cable highresolution seismic:. *oceanography,* Volume 22, p. 25.

Qu, D. & Tveranger, J., 2016. Incorporation of deformation band fault damage zones in reservoir models. *AAPG Bulletin,* 100(3), p. 423–443.

Rafaelsen, B., 2006. *Seismic resolution and frequency filtering,* Tromsø, Norway: Univ. Tromso Lecture Series.

Roca, X. & Nadon, G., 2007. Tectonic Control on the Sequence Stratigraphy of Nonmarine Retroarc Foreland Basin Fills: Insights from the Upper Jurassic of Central Utah, U.S.A. *Journal of Sedimentary Research,,* Volume v. 77, p. 239–255.

Rotevatn, A. & Fossen, H., 2011. Simulating the effect of subseismic fault tails and process zones in a siliciclastic reservoir analogue: Implications for aquifer support and trap definition:. *Marine and Petroleum Geology,* Volume 28, p. 1648–1662.

Rutqvist, J., 2012. The Geomechanics of CO2 Storage in Deep Sedimentary Formations. *Geotech Geol Eng ,* Volume 30, p. 525–551.

Røe, L. & Hermansen, 2006. new aspects of deformed cross-strata in fluvial sandstones: examples from Neoproterozoic formations in northern Norway. *sedimentary geology,* Volume 186, pp. 283-293.

Salazar, J. M., Bonnie, R. J., Clopine, W. W. & Michael, G. E., 2014. *Petrophysical Modelling: Mancos Modeling Uses Basic Log Data.* s.l.:The american Oil & Gas Reporter.

Schueller, S., Braathen, A., Fossen, H. & Tveranger, J., 2013. Spatial distribution of deformation bands in damage zones of extensional faults in porous sandstones; Statistical analysis of field data. *Journal of structural geology,* Volume 52, pp. 148-162.

Sheriff, R., 1996. Understanding the Fresnel zone: Search and Discovery article #40014:. *Geophysical corner, SEG.*.

Sheriff, R. E. & Geldart, L. P., 1995. *Exploration Seismology, p. 52.* 2 ed. s.l.:Cambridge University Press.

Shi, J.-Q.et al., 2013. Snøhvit CO2 storage project: Assessment of CO2 injection performance through history matching of the injection well pressure over a 32-months period. *Energy Procedia,* Volume 37, p. 3267 – 3274 .

Shipton, Z. & Cowie, P., 2001. Damage zone and slip-surface evolution over um to km scales in high porosity Navajo sandstone, Utah. *Journal of structural geology,* Volume 23, pp. 1825-1844.

Shipton, Z. K. et al., 2002. Structural heterogeneity and permeability in faulted eolian sandstone: Implications for subsurface modeling of faults. *AAPG Bulletin, v. 86,* Volume 5, pp. 863-883.

Shipton, Z. K., Evans, J. P. & Thompson, L. B., 2005. The Geometry and Thickness of Deformation-band Fault Core and its Influence on Sealing Characteristics of Deformation-band Fault Zones. *Faults, fluid flow, and petroleum traps: AAPG Memoir ,* Volume 85, p. 181–195.

Shuey, R. T., 1985. A simplification of the Zoeppritz equations. *Geophysics ,* Volume 50, p. 609–614..

Simm, R. & Bacon, M., 2014. *Seismic Amplitude: An interpreter's handbook.* s.l.:Cambridge university press.

Skurtveit, E. et al., 2020. Experimental Investigation of Natural Fracture Stiffness and Flow Properties in a Faulted CO2 Bypass System (Utah, USA). *Journal of geophysical research,* 125(7), p. p.e2019JB018917.

Sowers, T. & Boyd, O. S., 2019. *Petrologic and Mineral Physics Database for Use with the U.S. Geological Survey National Crustal Model,* Reston, Virginia: USGS.

Stockton, S. L. & Balch, A. H., 1978. *THE UTILITY OF PETROLEUM SEISMIC EXPLORATION DATA IN DELINEATING STRUCTURAL FEATURES WITHIN SALT ANTICLINES,* Colorado: UNITED STATES DEPARTMENT OF THE INTERIOR GEOLOGICAL SURVEY.

Tasianas, A., Mahl, L., Darcis, M. & Buenz, S., 2015. *Simulating seismic chimney structures as potential vertical migration pathways for CO2 in the Snøhvit area, SW Barents Sea: model challenges and outcomes.* Tromsø, CAGE-Centre for Arctic Gas Hydrate, Environment and Climate, Department of Geology, UiT. Environ Earth Sci (2016) 75:504.

Thore, P. & Juliard, C., 1999. Fresnel zone effect on seismic velocity resolution:. *Geophysics,* Volume 64, p. 593–603.

Thorman, C., 2011. The Elko orogeny: a major tectonic event in eastern Nevada–western utah. *Sprinkel, D.A., Yonkee, W.A., and Chidsey, T.C., Jr., eds., Sevier Thrust Belt: Northern and Central Utah and Adjacent Areas: Utah Geological Association,* Volume 40, p. 117–129.

Thorman, C. H. & Peterson, F., 2004. *The Middle Jurassic Elko Orogeny - A Major Tectonic Event in Nevada-Utah.* Utah, Salt lake city: U.S. Geological Survey.

Tiab, D. & Donaldson, E., 2016. Naturally Fractured Reservoirs (chapter 8). In: D. Tiab & E. Donaldson, eds. *Petrophysics Theory and Practice of Measuring Reservoir Rock and Fluid Transport Properties (4th edition).* s.l.:Gulf Professional Publishing, pp. 415-481.

Torabi, A., 2008. *"Deformation bands in porous sandstones: their microstructure and petrophysical properties" Dissertation for the degree Philosophiae Doctor.* Bergen: Department of Earth Science, University of Bergen.

Torabi, A. et al., 2020. Fault zone architecture and its scaling laws: where does the damage zone start and stop?. *Integrated fault seal analysis,* Volume 496, pp. 99-124.

Torabi, A. & Fossen, H., 2007. *Spatial variation of microstructure and petrophysical properties of properties of deformation bands..* Bergen: University of Bergen, department of earth sciences. Under review in Journal of Structural Geology.

Torabi, A., Fossen, H. & Braathen, A., 2013. *Insight into petrophysical properties of deformed sandstone reservoirs,* s.l.: The American Association of Petroleum Geologists.

Torabi, A., Johannessen, M. & Ellingsen, T., 2019. Fault Core Thickness: Insights from Siliciclastic and Carbonate Rocks. *Geofluids ,* Volume vol. 2019, p. 24.

Tsujia, T., Ikeda, T. & Jiang, F., 2019. Evolution of hydraulic and elastic properties of reservoir rocks due to mineral precipitation in CO2 geological storage. *Computers and Geosciences,* Volume 126, pp. 84-95.

Tueckmantel, et al., 2010. 0, Fault seal prediction of seismic-scalenormal faults in porous sandstone: A case study from the eastern Gulf of Suez rift, Egypt:. *Marine and Petroleum geology,* Volume 27, pp. 334-350.

Tunheim, R. J., 2015. *Mineralogical controls on the weathering characteristics of arid continental deposits of the Colorado Plateau.* s.l.:Department of Earth Science University of Bergen.

Tveranger, J. et al., 2007. Fault Facies Modelling - a Practical Approach to Incorporating 3D Fault Architecture in Standard Reservoir Models. *AAPG Search and Discovery Article #90072.*

Urquhart, A. S. M., 2011. *Structural controls on CO2 leakage and diagenesis in a natural long-term carbon sequestration analogue: Little Grand Wash fault, Utah.* Austin: The University of Texas at Austin.

Wang, L. et al., 2017. CO2 injection-induced fracturing in naturally fractured shale rocks. *Energy,* Volume 139, pp. 1094-1110.

Welch, M., Souque, C., Davies, R. & Knipe, R., 2011. *The Role of Fluid Overpressure in the Development of Fracture Corridors: A Finite Element Modelling Study.* s.l., European Association of Geoscientists & Engineer.

Wibberly, C., Yielding, G. & Do Toro, G., 2008. Recent advances in the understanding of fault zone internal structure: a review.. *Geol. Soc. Lond. Spec. Publ.,* Volume 299 , p. 5–33..

Wilkinson, M., Gilfillan, S., Haszeldine, R. & Ballentine, C., 2009. Plumbing the depths: Testing natural tracers of subsurface CO2 origin and migration, Utah. *AAPG Studies in Geology 59*, p. 619–634.

Williams, A. P., 2005. *STRUCTURAL ANALYSIS OF CO2 LEAKAGE THOUGH THE SALT WASH AND LITTLE GRAND WASH FAULTS FROM NATURAL RESERVOIRS IN THE.* Logan, Utah: UTAH STATE UNIVERSITY.

Willis, G. C., 1999. The Utah thrust system-an overview. *Utah Geological Association Publication,* Volume 27.

Wright, J. C., Daniel, S. & Lohman, S. V., 1962. DEFINITIOS OF MEMBERS OF JURASSIC ENTRADA SANDSTONE IN EAST-CENTRAL UTAH A.ND WEST-CENTRAL COLORADO. *BULLETIN OF TH E AMERICA N ASSOCIATION OF PETROLEU M GEOLOGISTS,* Volume VOL . 46, pp. 2057-2070.

Yamabe, H., Tsuji, T., Liang, Y. & Matsuoka, T., 2016. Influence of fluid displacement patterns on seismic velocity during supercritical CO2 injection: Simulation study for evaluation of the relationship between seismic velocity and CO2 saturation. *international journal of greenhouse gas control,* Volume 46, pp. 197-204.

Zuchuat, V. et al., 2019a. COMPOSITE AND DIACHRONOUS STRATIGRAPHIC SURFACES IN LOW-GRADIENT, TRANSITIONAL SETTINGS: THE J-3 ''UNCONFORMITY'' AND THE CURTIS FORMATION, EAST-CENTRAL UTAH, U.S.A... *Journal of sedimentary research volume 89,* pp. 1075-1095.

Zuchuat, V. et al., 2019b. Overprinted allocyclic processes by tidal resonance in an epicontinental basin: the Upper Jurassic Curtis Formation, east-central Utah, USA: The Depositional Record, v. 5, p. 272–305.. *The Depositional Record, v. 5,* p. 272–305.

Zuchuat, V. et al., 2018. New insights on the impact of tidal currents on a low-gradient, semi-enclosed, epicontinental basin: the Curtis Formation, east-central Utah, USA. *Geology of the intermountain west v. 5,* pp. 131-165.

Appendix

Appendix 1: Base model

Grayscale model and velocity model for M1 input into seismic modelling software
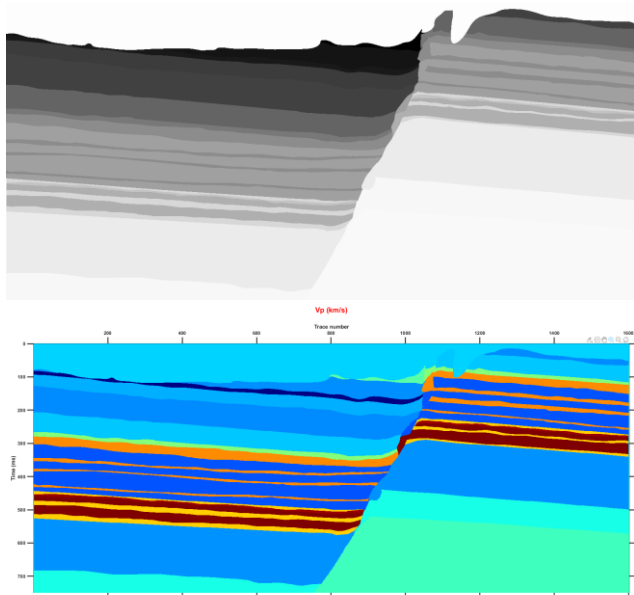
Appendix 2: Model With damage zone

Grayscale model and velocity model for M2 input into Seismic modelling programs
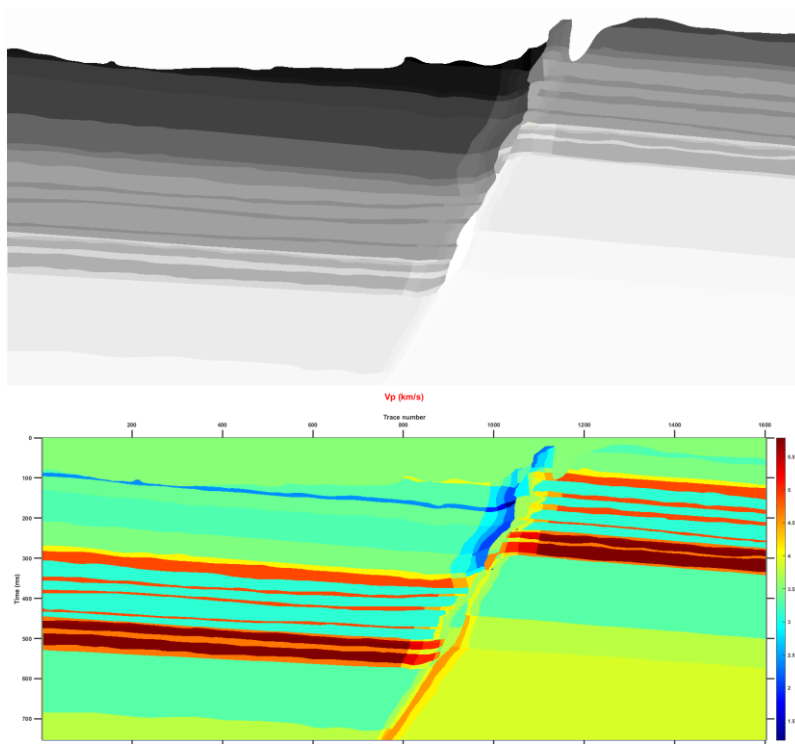
Appendix 3: Model With CO$_2$

Grayscale model and velocity model for M3 input into seismic modelling programs
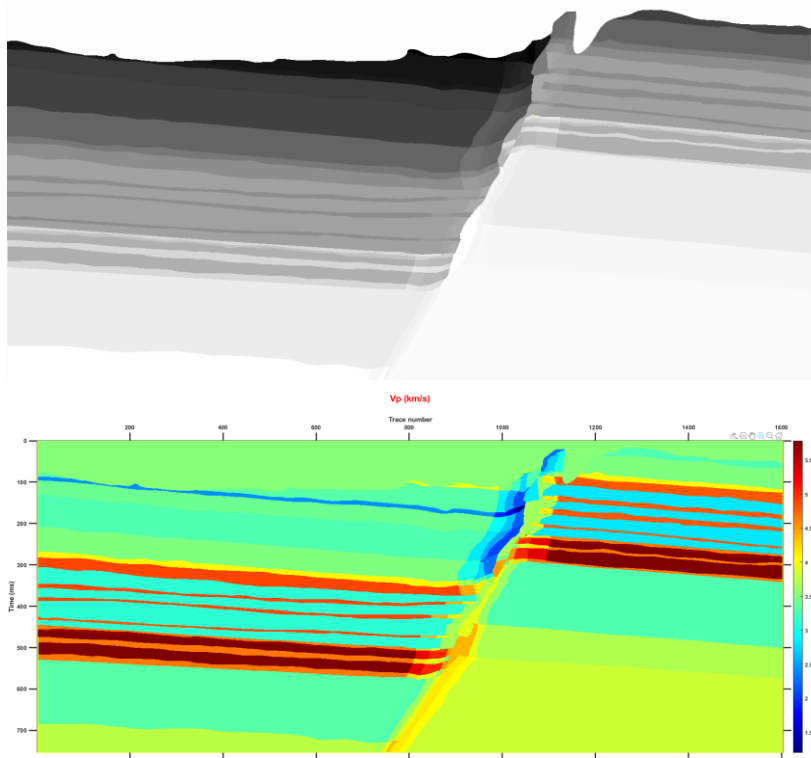
Appendix 4: Model With Bleaching

Grayscale model and velocity model for M4 input into seismic modelling programs
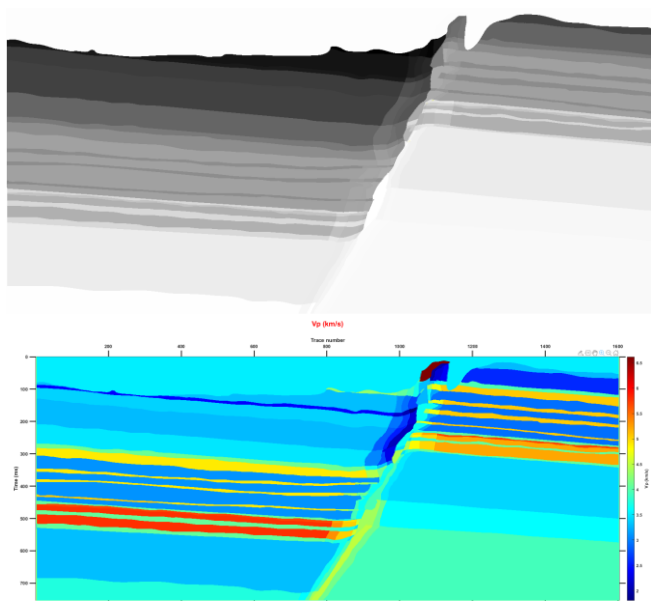
Appendix 5: overburden model without CO$_2$

Grayscale model and velocity model for M5 input into seismic modelling programs
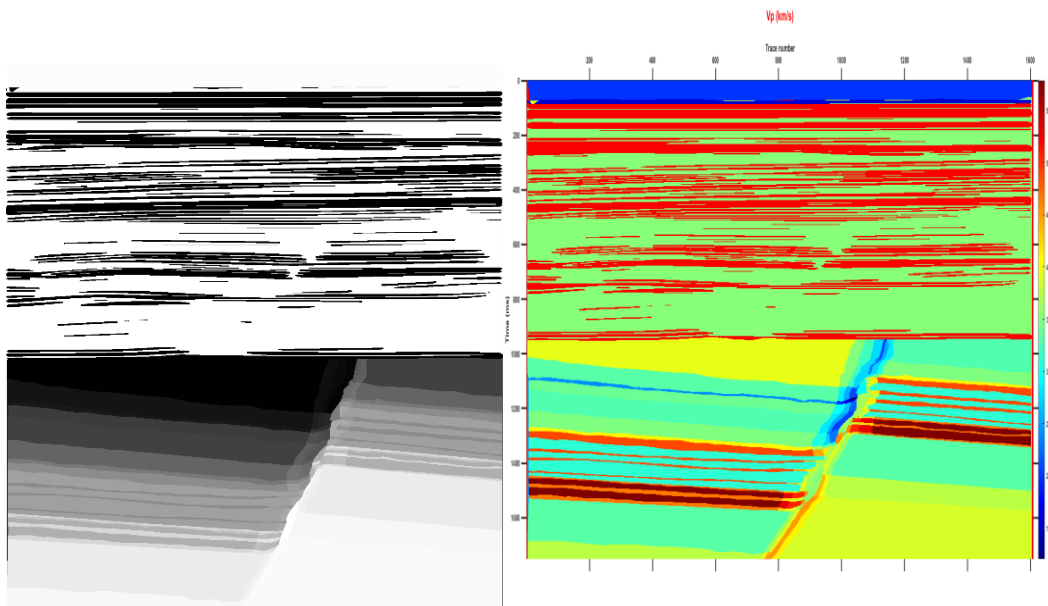
Appendix 6: overburden model with CO$_2$

Grayscale model and velocity model for M6 input into seismic modelling programs
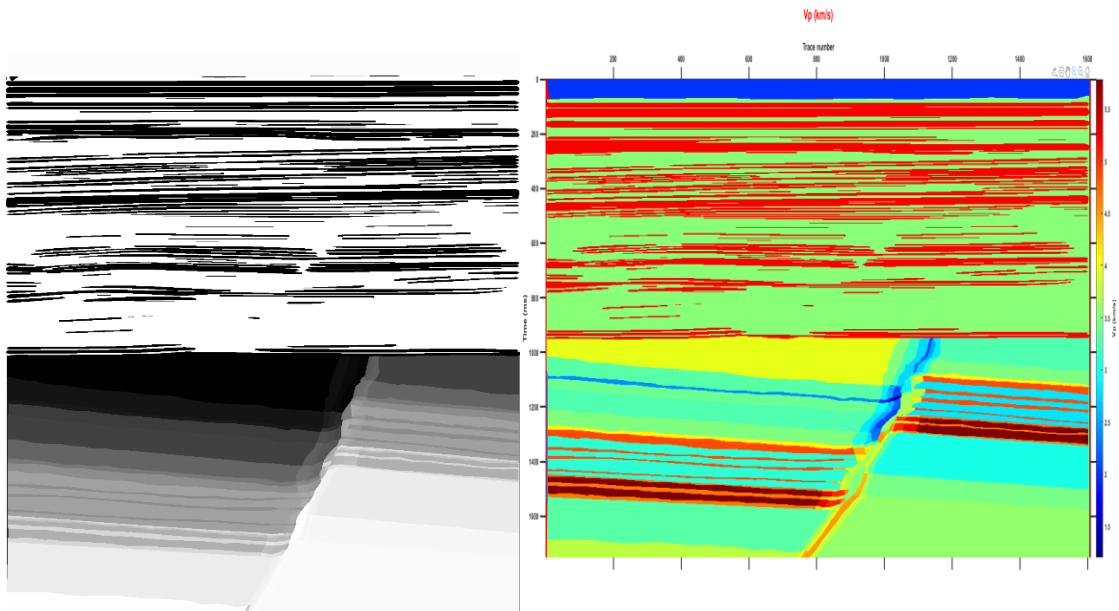
	Unit	M.	P(	Vp CO2	Vp CO2 H	Vp	Vp brine	Vp matrix	Depth (m) FW	Pressure FW	Depth (m)	Pressure HW	RGB M1	RGB M3	RGB M4
2	Mancos	2	0			3950	1550	4100			1	0,0098	0	0	
3	Mancos CO2 altered (FW only)	3	0			4289,31	1550	4947,43			1	0,0098			0
4	Silisiclastic damage zone Fracture count >16				2750	2750					1	0,0098	5	5	
5	Silisiclastic damage zone Fracture count 3<16				3200	3200					1	0,0098	10	10	
6	Silisiclastic damage zone Fracture count				3500	3500					1	0,0098	15	15	
7	Silisiclastic damage zone bleached Fracture count >16				3689,31	3689,31					1	0,0098			5
8	Silisiclastic damage zone bleached Fracture count 3<16				3914,31	3914,31					1	0,0098			10
9	Silisiclastic damage zone bleached Fracture count < 3				4064,31	4064,31					1	0,0098			15
10	Cedar mountain (shale)				3300	3300					15	0,147	20	20	20
11	Cedar mountain (buckhorn conglon				2403	2403					60	0,588	25	25	25
12	Silisiclastic damage zone Fracture count >16				2100	2100					15	0,147	40	30	
13	Silisiclastic damage zone Fracture count 3<16				2550	2550					15	0,147	35	35	
14	Silisiclastic damage zone Fracture count < 3				2850	2850					15	0,147	30	40	
15	Silisiclastic damage zone Fracture count >16				1203	1203					60	0,588	45	45	
16	Silisiclastic damage zone Fracture count 3<16				1653	1653					60	0,588	50	50	
17	Silisiclastic damage zone Fracture count				1953	1953					60	0,588	55	55	
18	Silisiclastic damage zone bleached Fracture count >16				2700	2700					15	0,147			30
19	Silisiclastic damage zone bleached Fracture count 3<16				2925	2925					15	0,147			35
20	Silisiclastic damage zone bleached Fracture count < 3				3075	3075					15	0,147			40
21	Silisiclastic damage zone bleached Fracture count >16				1803	1803					60	0,588			45

	A	B	C	D	E	F	G	H	I	J	K	L	M	N	O
22	Silisiclastic damage zone bleached Fracture count 3<16				2028	2028					60	0,588			50
23	Silisiclastic damage zone bleached Fracture count < 3				2178	2178					60	0,588			55
24	Morrison (brushy basin)				3400	3400					77	0,7546	60	60	60
25	Morrisson (salt wash)				3275	3275					115	1,127	65	65	65
26	Silisiclastic damage zone Fracture count >16				2200	2200					77	0,7546	70	70	70
27	Silisiclastic damage zone Fracture count 3<16				2650	2650					77	0,7546	75	75	75
28	Silisiclastic damage zone Fracture count <3				2950	2950					77	0,7546	80	80	80
29	Silisiclastic damage zone Fracture count >16				2075	2075					115	1,127	85	85	85
30	Silisiclastic damage zone Fracture count 3<16				2525	2525					115	1,127	90	90	90
31	Silisiclastic damage zone Fracture count < 3				2825	2825					115	1,127	95	95	95
32	Summerville siltstone	3	0		4109,83	4109,83	1550	5033,47			191	1,8718	100	100	101 (HW)
33	Summerville siltstone CO2 altered (FW only	3	0		4035,33	4035,33	1550	4689,13			191	1,8718			100
34	Silisiclastic damage zone Fracture count >16				2909,83	2909,83					191	1,8718	105	105	106 (HW)
35	Silisiclastic damage zone Fracture count 3<16				3359,83	3359,83					191	1,8718	110	110	111 (HW)
36	Silisiclastic damage zone Fracture count <3				3659,83	3659,83					191	1,8718	115	115	116 (HW)
37	Silisiclastic damage zone (bleached) Fracture count >16				3435,33	3435,33					191	1,8718			105
38	Silisiclastic damage zone Fracture count 3<16				3660,33	3660,33					191	1,8718			110
39	Silisiclastic damage zone Fracture count <3				3810,33	3810,33					191	1,8718			115
40	Curtis			4100	4100	4100			28	0,2744	238	2,3324	120	120	121
41	Curtis (CO2 altered) (FW only			3950	3950	3950			28	0,2744	238	2,3324			120

#	Description														
41	Curtis (CO2 altered) (FW only			3950	3950	3950			28	0,2744	238	2,3324			120
42	Silisiclastic damage zone Fracture count >16			2820	2900	2900			28	0,2744	238	2,3324	125	125/126	126 (HW)
43	Silisiclastic damage zone Fracture count 3<16			3350	3350	3350			28	0,2744	238	2,3324	130		130 131 (HW)
44	Silisiclastic damage zone Fracture count < 3			3650	3650	3650			28	0,2744	238	2,3324	135		135 136 (HW)
45	Silisiclastic damage zone (bleached) Fracture count >16			3270	3350	3350			28	0,2744	238	2,3324			125
46	Silisiclastic damage zone Fracture count 3<16			3575	3575	3575			28	0,2744	238	2,3324			130
47	Silisiclastic damage zone Fracture count <3			3725	3725	3725			28	0,2744	238	2,3324			135
48	Entrada earthy facies (co2 altered)	3	0	5045	5124,88	5124,88	1550	5669,73	35	0,343	247	2,4206			140
49	Entrada sandstone earthy facies (unaltered)	3	0	4534	4614,33	4614,33	1550	5421	35	0,343	247	2,4206	140	140/141	141 (HW)
50	Silisiclastic damage zone Fracture count >16			3334	3414,33	3414,33			35	0,343	247	2,4206	145	145/146	146 (HW)
51	Silisiclastic damage zone Fracture count 3<16			3864	3864,33	3864,33			35	0,343	247	2,4206	150		150 151 (HW)
52	Silisiclastic damage zone Fracture count <3			4164	4164,33	4164,33			35	0,343	247	2,4206	155		155 156 (HW)
53	Silisiclastic damage zone (bleached) Fracture count >16			4445	4524,88	4524,88			35	0,343	247	2,4206			145
54	Silisiclastic damage zone Fracture count 3<16			4750	4749,88	4749,88			35	0,343	247	2,4206			150
55	Silisiclastic damage zone Fracture count <3			4900	4899,88	4899,88			35	0,343	247	2,4206			155
56	Entrada dune facies (co2 altered)	2	0	2921	3170,96	3220,96	1550	4219,46	50	0,49	297	2,9106			160

#	Description														
59	Entrada UNALTERED (W5)	3	0	3627	3927,44	3927,44	1550	5921	50	0,49	297	2,9106	165	165/166	166(HW)
60	Entrada Sandstone (W10)	3	0	3643	3643,38	3643,38	1550	4783,45	50	0,49	297	2,9106	170	170	170
61	Carmel co2 exposed	3	0	5215	5215,49	5215,49	1550	5479,96	150	1,47	403	3,9494			175
62	Carmel (unexposed)	3	#	5784	5784,41	5784,41	1550	6527,42	150	1,47	403	3,9494	175	175	176(HW)
63	Silisiclastic damage zone Fracture count >16			4524	4584,41	4584,41			150	1,47	403	3,9494	180	180/181	181(HW)
64	Silisiclastic damage zone Fracture count 3<16			5034	5034,41	5034,41	1550	6527,42	150	1,47	403	3,9494	185	185	186(HW)
65	Silisiclastic damage zone Fracture count <3			5334	5334,41	5334,41	1550	6527,42	150	1,47	403	3,9494	190	190	191(HW)
66	Silisiclastic damage zone (bleached) Fracture count >16			4405	4465,49	4465,49			150	1,47	403	3,9494			180
67	Silisiclastic damage zone Fracture count 3<16	ii k		4815	4815,49	4815,49			150	1,47	403	3,9494			185
68	Silisiclastic damage zone Fracture count <3			4990	4990,49	4990,49			150	1,47	403	3,9494			190
69	Carmel F2	3	0	5689	5689,49	5689,49	1550	6620	170	1,666	423	4,1454	195	195	195
70	Silisiclastic damage zone Fracture count >16			4459	4489,49	4489,49			170	1,666	423	4,1454	200	200/201	200/201
71	Silisiclastic damage zone Fracture count 3<16			4939	4939,49	4939,49			170	1,666	423	4,1454	205	205	205
72	Silisiclastic damage zone Fracture count < 3			5239	5239,49	5239,49			170	1,666	423	4,1454	210	210	210
73	Carmel F3	3	0	4657	4657,4	4667,4	1550	5500	190	1,862	443	4,3414	215	215	216
74	Silisiclastic damage zone Fracture count >16			3447	3447,4	3467,4			190	1,862	443	4,3414	220	220	221(HW)
75	Silisiclastic damage zone Fracture count 3<16			3917	3917,4	3917,4			190	1,862	443	4,3414	225	225	226
76	Silisiclastic damage zone Fracture count <3			4217	4217,4	4217,4			190	1,862	443	4,3414	230	230	231
77	Carmel 3 co2 bleached			4059	4059,4	4069,4			190	1,862	443	4,3414			215
	Silisiclastic damage zone Fracture count				3449,4	3469,4									

#	Name															
77	Carmel F3 co2 altered			4059	4059,4	4069,4			190	1,862	443	4,3414			215
78	Silisiclastic damage zone Fracture count >16			3449	3449,4	3469,4			190	1,862	443	4,3414			220
79	Silisiclastic damage zone Fracture count 3<16			3694	3694,4	3694,4			190	1,862	443	4,3414			225
80	Silisiclastic damage zone Fracture count <3			3844	3844,4	3844,4			190	1,862	443	4,3414			230
81	Sandstone (bleached) navajo	2	0	3355	3354,51	3404,51	1550	4145,67	220	2,156	470	4,606			235
82	Navajo, unaltered	2	0	3263	3313,19	3313,19	1550	4066,17	220	2,156	470	4,606	235	235/236	236 (HW)
83	Navajo W5 (unaltered	2	0	3601	3601,26	3651,26	1550	4066,17	220	2,156	470	4,606	240		240 241(HW)
84	Navajo W5 (bleached)			3514	3514	3564			220	2,156	470	4,606			240
85	Navajo W10 (unaltered)	2	0	3938	3938,3	3938,3	1550	4066,17	220	2,156	470	4,606	245	245	245
86	Kayenta (CO2 altered)			3609	3609	3659			370	3,626	620	6,076			247
87	Kayenta w5 (bleached)			4126	4126,3	4176,3			370	3,626	620	6,076			248
88	Kayenta W10			4375	4375	4375			370	3,626	620	6,076	246	246	246
89	Kayenta (Unaltered)			3700	3750	3750			370	3,626	620	6,076	247	247/254	254(HW)
90	kayenta w5 unaltered			3938	3988	3988			370	3,626	620	6,076	248	248/255	255 (HW)
91	Wingate (unaltered			3825	3875	3875			440	4,312			249	249	
92	Wingate (bleached)			3916	3966	3966			440	4,312					249
93	Wingate W5			4063	4113	4113			440	4,312			250	250	
94	Wingate W5 (bleached)			4154	4204	4204			440	4,312					250
95	Wingate W10			4500	4500	4500			440	4,312		v	251	251	251
96	calcite	3		6620	6620	6620									253
97	Overburden 1					3521							253		3
98				4138	3684,55	3698,02									

	P	Q	R	S	T		U
	pressure depth	solubility CO2	concentration CO2	SCO2			Vp anomaly (high porosity facies)
	0,147	15	0,05	0,1	7,873906706		400
	0,49	50	0,26	0,27	0,472434402		100
	0,686	70	0,3	0,31	0,337453145		100
	0,98	100	0,35	0,42	1,653520408		300
	1,47	150	0,4	0,45	0,787390671		150
	1,96	200	0,65	0,6	-0,530543003		50
	2,94	300	0,8	0,8	0		50
	3,92	400	0,87	0,87	0		50
	5,88	600	0,9	0,9	=((510-R10)*0,83)*273)/(P10*9,8)		50

Solubility and CO2 concentrations

Appendix 8: Velocity calculations Model 5 and Model 6

	A	B	C	D	E	F	I	J
1	Unit	Matrix de	Porosity	Vp CO2 FW	Vp CO2 HW	Vp	RGB M5	RGB M6
2	Mancos	2,4188	0,08			3950	1	1
3	Mancos CO2 altered (FW only)	2,5999	0,07			4289,312179		
4	Silisiclastic damage zone Fracture count >16				2750	2750	5	5
5	Silisiclastic damage zone Fracture count 3<16				3200	3200	10	10
6	Silisiclastic damage zone Fracture count < 3				3500	3500	15	15
7	Cedar mountain (shale)				3300	3300	20	20
8	Cedar mountain (buckhorn conglomerate)				2403	2403	25	25
9	Silisiclastic damage zone Fracture count >16				2100	2100	30	30
10	Silisiclastic damage zone Fracture count 3<16				2550	2550	35	35
11	Silisiclastic damage zone Fracture count < 3				2850	2850	40	40
12	Silisiclastic damage zone Fracture count >16				1203	1203	45	45
13	Silisiclastic damage zone Fracture count 3<16				1653	1653	50	50
14	Silisiclastic damage zone Fracture count < 3				1953	1953	55	55
15	Morrison (brushy basin)				3400	3400	60	60
16	Morrisson (salt wash)				3275	3275	65	65
17	Silisiclastic damage zone Fracture count >16				2200	2200	70	70
18	Silisiclastic damage zone Fracture count 3<16				2650	2650	75	75
19	Silisiclastic damage zone Fracture count < 3				2950	2950	80	80
20	Silisiclastic damage zone Fracture count >16				2075	2075	85	85
21	Silisiclastic damage zone Fracture count 3<16				2525	2525	90	90

	A	B	C	D	E	F	I	J
22	Silisiclastic damage zone Fracture count <3				2825	2825	95	95
23	Summerville siltstone	2,47213	0,1		3483,664247	3483,664247	100	100
24	Summerville siltstone CO2 altered (FW only	2,24353	0,08		2584,181835	2584,181835		
25	Silisiclastic damage zone Fracture count >16				2283,664247	2283,664247	105	105
26	Silisiclastic damage zone Fracture count 3<16				2733,664247	2733,664247	110	110
27	Silisiclastic damage zone Fracture count <3				3033,664247	3033,664247	115	115
28	Curtis			4100	4100	4100	120	120
29	Curtis (CO2 altered) (FW only			3950	3950	3950		
30	Silisiclastic damage zone Fracture count >16			2870	2900	2900	125	125/126
31	Silisiclastic damage zone Fracture count 3<16			3350	3350	3350	130	130
32	Silisiclastic damage zone Fracture count <3			3650	3650	3650	135	135
33	Entrada sandstone earthy facies (unaltered)	2,69	0,06	4859,917747	4889,917747	4889,917747	140	140/141
34	Silisiclastic damage zone Fracture count >16			3659,917747	3689,917747	3689,917747	145	145/146
35	Silisiclastic damage zone Fracture count 3<16			4139,917747	4139,917747	4139,917747	150	150
36	Silisiclastic damage zone Fracture count <3			4439,917747	4439,917747	4439,917747	155	155
37	Entrada dune facies (una	2,66	0,24	2800	3100	3100	160	160/161
38	Entrada UNALTERED (W5)	2,66	0,18	3627,435972	3927,435972	3927,435972	165	165/166
39	Entrada Sandstone (W10)	2,5079	0,15	3643,384544	3643,384544	3643,384544	170	170
40	Carmel co2 exposed	2,6672	0,02	5215,488372	5215,488372	5215,488372		
41	Carmel (unexposed)	2,78642	0,04	5784,412884	5784,412884	5784,412884	175	175

	A	B	C	D	E	F	I	J
42	Silisiclastic damage zone Fracture count >16			4524,412884	4584,412884	4584,412884	180	180/181
43	Silisiclastic damage zone Fracture count 3<16			5034,412884	5034,412884	5034,412884	185	185
44	Silisiclastic damage zone Fracture count < 3			5334,412884	5334,412884	5334,412884	190	190
45	Carmel F2	2,65	0,05	5689,492653	5689,492653	5689,492653	195	195
46	Silisiclastic damage zone Fracture count >16			4429,492653	4489,492653	4489,492653	200	200/201
47	Silisiclastic damage zone Fracture count 3<16			4939,492653	4939,492653	4939,492653	205	205
48	Silisiclastic damage zone Fracture count <			5239,492653	5239,492653	5239,492653	210	210
49	Carmel F3			3423	3423	3483	215	215
50	Silisiclastic damage zone Fracture count >16			2163	2163	2283	220	220
51	Silisiclastic damage zone Fracture count 3<16			2733	2733	2733	225	225
52	Silisiclastic damage zone Fracture count <			3033	3033	3033	230	230
53	Carmel F3 co2 altered			2825	2825	2885		
54	Navajo, unaltered	2,39559	0,14	3013,189689	3313,189689	3313,189689	235	235/236
55	Navajo W5 (unaltered	2,39559	0,07	3351	3351	3651	240	240/241
56	Navajo w5 (bleached)			3264	3264	3564		
57	Navajo W10 (unaltered)	2,39559	0,02	3938,303879	3938,303879	3938,303879	245	245

	A	B	C	D	E	F	I	J
57	Navajo W10 (unaltered)	2,39559	0,02	3938,303879	3938,303879	3938,303879	245	245
58	Kayenta W10			4375	4375	4375	246	246
59	Kayenta (Unaltered)			3450	3750	3750	247	247/254
60	Kayenta W5 (unaltered)			3688	3988	3988	248	248/202
61	Wingate (unaltered			3575	3875	3875	249	249
62	Wingate (bleached)			3666	3966	3966		
63	Wingate W5			3813	4113	4113	250	250
64	Wingate W5 (bleached)			3904	4204	4204		
65	Wingate W10			4500	4500	4500	251	251
66	Calcite/aragonite Travertine	2,65		6620	6620	6620		
67	Loose overburden					3521		
68				4015,797323	3539,79261	3570,55764		
69	Average velocity			3777,794966				
70	Dense overburden					5215		
71	seafloor					2000		

pressure: depth		Saturation	Vp anomaly (high porosity facies)	
9,947	1015	50 %		150
10,29	1050	100 %		300
10,486	1070	50 %		300
10,78	1100	50 %		150
11,27	1150	50 %		150
11,76	1200	20 %		50
12,74	1300	20 %		50
13,72	1400	20 %		50
15,68	1600	20 %		50

91